The structure and the dynamics of poly(vinyl methyl ether) PVME and PVME in concentrated water solution:

A study by neutron scattering and fully atomistic molecular dynamics simulations.

Sara Capponi

Thesis supervisors:

Juan Colmenero de León
Arantxa Arbe

Ph. D. Thesis
2011

author's e-mail: saracapp@gmail.com

I think that this situation absolutely requires a really
futile and stupid gesture to be done.

(Bluto Blutarsky, motivational speech.)

PREFACE

Studying water in confined geometry and in mixtures is an issue of the utmost importance. Water indeed plays an essential role in biological processes and a large amount of water molecules is found very close to fundamental biomolecules affecting or even controlloing their functionality. Furthermore, in confined geometry water crystallization on cooling is prevented and in this way it is possible to study water in the so-called "no man's land" (the region experimentally inaccessible in the bulk phase) and to shed light on the origin of the water anomalies.

In this field aqueous polymer solution represents a very suitable sample. Polymers, though sharing features with biological macromolecules, are simpler systems. So they can be used as model systems trying to mimic the biological ones and to investigate the role played by the water in biological processes. Moreover, depending on the glass transition temperature, polymer dynamics can appear as frozen in the time scale of the experiment, allowing investigation of the structure and dynamics of bulk-like water in the temperature range corresponding to the "no man's land".

The joint use of neutron scattering (NS) and fully atomistic molecular dynamics simulation (MD) techniques offers a powerful tool to study polymers and aqueous polymer solutions. Thermal neutrons are characterized

by energy of the same order of magnitude of the intermolecular energies and wavelength of the same order of the distances typical of soft matter. In addition, aqueous polymer solution, and in general biological systems, are rich of hydrogen atoms, to which neutrons are very sensitive probes. The dependence of the scattering on the isotopes makes possible to focus the study on a functional group or on a single molecule by labelling it through selective deuteration procedures. Molecular dynamics simulations, performed in parallel to the experiments and properly validated by them, provide essential information to unveil the characteristics of the sample regarding both dynamical and structural aspects. X-ray diffraction and broadband dielectric spectroscopy (DS) represent useful complementary experimental techniques. They allow investigating the structure of the sample and extending the dynamics window spanned by neutron scattering instruments respectively.

The topic of this Ph. D. thesis is the study of the structure and the dynamics of a hydrophilic polymer, poly(vinyl methyl ether)(PVME) and PVME in concentrated aqueous solution. Chapter 1 provides a general overview of the sample by discussing polymer and water features. In Chapter 2 an introduction to the neutron scattering techinque is given along with a description of the instruments used. X-ray and dielectric spectroscopy techniques and instruments are also illustrated. The simulation method and how it has been applied in this work is described in Chapter 3. In Chapter 4 the structure and the dynamics of the dry PVME and how the results have been analyzed in the light of the Mode-Coupling Theory (MCT) are discussed. The structure and the dynamics of water in the solution and how it affects the PVME behaviour are discussed in Chapter 5. The results are finally summarized in the Conclusions.

CONTENTS

BACKGROUND

1.1 Polymeric systems

1.1.1 Basic characteristics of Polymers

Polymers are macromolecules formed by a large number of repeating structural units linked by covalent bonds. They constitute a wide class of materials which spans from *synthetic* polymers, produced by chemical industry, to *biopolymers* such as natural products, proteins or DNA. In this work, the term *polymer* will refer to organic compounds in which the backbone, commonly named *main chain*, is made up mainly of carbon atoms. Single atoms, as Hydrogen or Oxygen, or groups of atoms, the so-called *side groups*, can be linked to the main chain atoms.

The repeating structural unit is called *monomer* and the number of monomers in a polymer chain determines the *degree of polymerization*. In a polymeric system chains of different sizes are usually found. Therefore, rather than relate polymers with an unique degree of polymerization, *molecular weight distribution functions* are used. The *number-average molecular weight* M_n and the *weight-average molecular weight* M_w are respectively defined as

$$M_n = \frac{\sum_i N_i M_i}{\sum_i N_i}$$

$$M_w = \frac{\sum_i N_i M_i^2}{\sum_i N_i M_i}$$

with N_i the number of molecules of molecular weight M_i. In general $M_w > M_n$ and the ratio M_w/M_n, called *polydispersivity index*, provides a characterization of the width of the molecular weight distribution [1–3].

Polymers' features are affected not only by the value of the polydispersivity, same polymers with different polydispersity value can indeed exhibit very different properties. Their features are also determined by the steric arrangement of the repeating units along the chain, by the chain conformation, that is the spatial organization of the chain as zig-zag, helical, folded chain, etc., and by the chain configuration, also called *microstructure*. *Homopolymers* are polymers formed by a single type of monomers, while polymers which contain different monomeric units are called *copolymers*. There also exist many different architectures in which polymers can be found, like star, branched, linear, etc. All these characteristics contribute to the mechanical and dynamical features of each specific system.

This Ph. D. thesis is focused on the structural and dynamical properties of poly(vinyl methyl ether) (PVME) and its concentrated aqueous solution with water content $c_w = 30\%$ in weight. PVME is widely used in chemical, farmaceutical and textile fields and the chemical formula is shown in Fig. 1.1.

$$-\left[CH_2\text{-}CH\right]_n-$$
$$\big|$$
$$O$$
$$\big|$$
$$CH_3$$

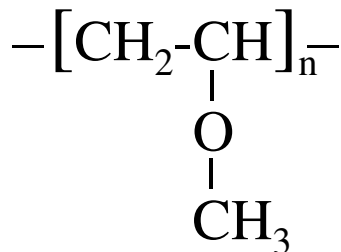Figure 1.1: Chemical formula of PVME.

1.1.2 Relaxation processes and the Glass Transition

Polymers are viscoelastic materials and their state depends on the temperature and the time allotted to the experiment [1]. At high temperature polymers form viscous liquids, called polymer melts, in which thermal equilibrium is always mantained. On cooling, the characteristic times of the main relaxation process in the melts, the α- or structural relaxation, increase so much that the system is no longer able to continuosly equilibrate. Finally the α-relaxation freezes and the polymer is found to be stiff and glassy: a glass is obtained. The transition from a viscous liquid to a glass is called *glass transition*. It is a general feature of glass-forming liquids and the temperature at which such transition takes place is called *glass transition temperature T_g*. At low enough temperature, polymers are usually found in a glassy or in a semicristalline state, where ordered regions alternate with amorphous ones. Due to the particular microstructure and to the irregular chain configurations most of polymers do not crystallize on cooling and this makes them good *glass formers* [4, 5].

Due to the macromolecular character of the structural units in a polymer, different relevant length scales can be distinguished, from the dimension of a monomer, which is of the order of $\approx 5\,\text{Å}$, to the radius of gyration, which represents the average size of the polymer and can vary from $100\,\text{Å}$ to $1000\,\text{Å}$ [2, 6, 7]. The time scale spanned by polymer dynamics is also very wide. It goes from the vibrational motions and the fast dynamics, which take place with characteristic times of the order of $10^{-14} - 10^{-12}s$, to the center of mass diffusion, which in the glassy state is completely frozen, while in the molten state can occur with long associated times. In between, other relaxational processes, like the α-relaxation or secondary relaxation, take place.

To visualize with a real example the time scale covered by polymer dynamics and the molecular origin of the different motions the relaxation map of polyisoprene (PI) is represented in Fig. 1.2 [8]. At a generic temperature below the glass transition, indicated in the graph by a blue dotted-dashed
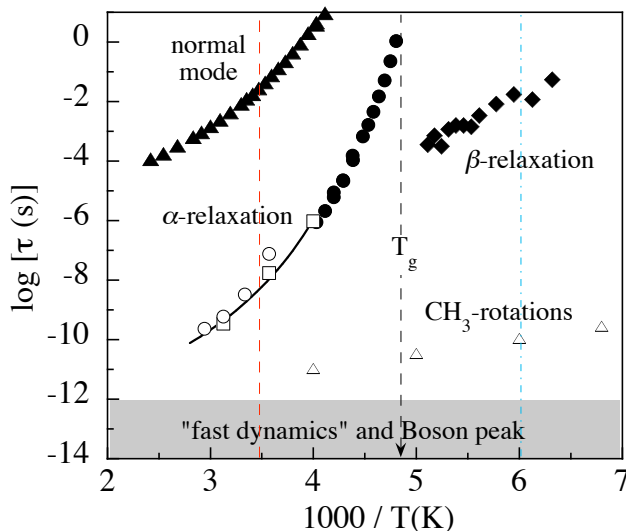
Figure 1.2: Relaxation map of polyisoprene: results from dielectric spectroscopy (*full symbols*), rheological shift factor (*solid line*) and neutron scattering (*empty symbols*) [8]. The shadowed area indicates the time scales of the fast dynamics and the Boson peak. The black dashed line corresponds to the glass transition temperature, while the red dashed line and the blue dotted-dashed line represent generic temperatures above and below the glass transition respectively.

line, the polymer is in the glassy state and only local motions occur: (i) in the range of $10^{-14} - 10^{-12}s$ the fast dynamics and the Boson peak, a low frequency vibrational anomaly typical of glassy materials, are found; (ii) the methyl group rotation takes place at $\approx 10^{-10}s$; (iii) the secondary β-relaxationis occurs at $\approx 10^{-2}s$. Above the glass transition a more complex scenario is observed. At a fixed temperature, indicated in the graph by a red line, the following processes are found: (i) the vibrational processes (the fast dynamics and the Boson peak) occur in the range of $10^{-14} - 10^{-12}s$; (ii) the structural or α-relaxation takes place at times of $\approx 10^{-9} - 10^{-7}s$. The associated length scales correspond to interchain distances which are of the order of $\approx 10\text{Å}$; (iii) in the case of the (PI) sample investigated in [8], the normal mode is detected by means of broadband dielectric spectroscopy and it occurs at the very long time of $\approx 10^{-2}s$. The normal mode is due to the relaxation of the end-to-end vector and thereby related to the size of the
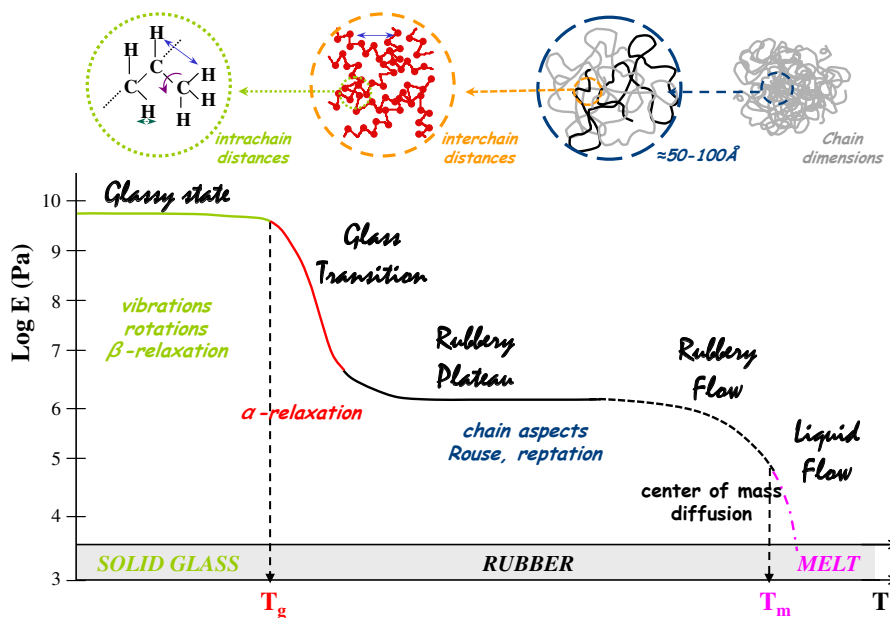
Figure 1.3: Dynamic modulus of a bulk polymer and its molecular origin as a function of temperature. The indicated length scales vary from the typical bond length at low T to the proper chain dimensions at high T.

chain.

These dynamical processes are also reflected in the mechanical properties. A schematic representation of the Young's modulus as a function of the temperature is shown in Fig. 1.3. The length scales of the molecular motions corresponding to the different region of the dynamic modulus are also illustrated. Five regions can be distinguished and they will be examined in the following.

the Glassy Region

In the glassy state only local processes, like vibrations, short range rotations or secondary relaxations take place. Local motions, such as methyl group rotations or flip-motion of the side groups, can be detected by neutron scattering (NS) or relaxation techniques like dielectric or mechanical spectroscopy [2, 9]. The temperature dependence of the relaxation times

associated to these processes can be described by an Arrhenius law

$$\tau = \tau_0\, exp\frac{E_0}{k_B T} \qquad (1.1)$$

in which E_0 represents the activation energy of the process and k_B the Boltzmann's constant. In this region the Boson peak is commonly observed as a particular feature in the vibrational density of states of glassy systems (see Fig. 1.2).

the Glass Transition Region

The glass-transition region can be identified with the onset of the primary or structural relaxation: the α-relaxation. Cooperative processes involving longer chain sequences become possible in the time scales of observation and allow the system to flow. As a consequence the modulus drops abruptly and few degrees of temperature change affect the behaviour of the glass-forming system enormously. In this region the relevant length scale refers to interchain distances. The temperature dependence of the characteristic relaxation time τ_α associated to the α-relaxation is usually described by a Vogel-Fulcher function [10, 11]

$$\tau_\alpha = \tau_{\alpha_0} exp\frac{B}{T - T_0} \qquad (1.2)$$

The Vogel temperature T_0 represents a singularity in which, as temperature is approaching, the characteristic relaxation time diverges. To fully characterize the α-relaxation usually different techniques have to be combined. The glass transition phenomenon will be extensively discussed in the next paragraph.

the Rubbery Plateau

In the rubbery plateau region the modulus is almost constant and large scale motions within the polymer chain are involved. In this regime and in the rubbery flow, the following one, the properties are basically determined

by the macromolecular character of the structural units: the topological constraints and how they are released are the main ingredient to be considered. Polymer melts, in fact, resemble a temporary network in which chain entanglements, effective for a limited time, act as constraints being able to suppress flow [2]. In such scenario the single chain dynamics is described by means of the Rouse model [12], while the motion of the confined chains, taking the constraints into account, is explained by means of the *reptation model* [6, 13]. Such model is based on the concept that a polymer chain in the melt is considered to move within a *tube* formed by adjacent chains, which represent obstacles for the lateral motion and so shape the confinement range. The motion of the chain is so formed by two components. The first consists of a rapid wriggling motion oriented along the tube cross-section and it can be described in terms of the Rouse motion. The second component corresponds to the time dependent evolution of the *primitive path*, the shortest path connecting the endgroups of the chain compatible with the topology of the entanglements, that is the tube topology. The *primitive chain* is the chain associated to the primitive path and the disentanglement process is described in terms of reptation motion of it. As parts of the primitive chain have left the original tube, the adjacent chains occupy the empty space and modify the constraints, so a part of the tube disappears. The result is a continous shortening of the tube until it completely disappears and the process of disentangling is finished. Therefore, the width of the rubbery plateau is related with the time the chain needs to reptate along the tube and this is directly determined by the chain length.

the Rubbery Flow Region

As the temperature increases the rubbery flow region is reached. In this regime, depending on the time scale of the experiment, polymers show both rubber elasticity and flow features. At short times the entanglements cannot relax, while at long times and at high temperature the chains are able to

escape from the tube and hence to flow. The rubbery flow regime is thus reached when the chain can easily reptate out through the entanglements. It is noteworthy to underline that cross-linked polymers undergo decomposition before reaching this region [1].

the Liquid Flow Region

When temperature is further increased the chains can finally flow as individual molecules leading to the liquid flow [1]. In this region the center of mass diffusion is the dominant mechanism.

As a final remark, it is worthy to emphasize that while the features of the dynamics driving the glassy and the glass-transition regime are universal for glass-forming systems, the rubbery plateau, which relates with the dynamics within the tube, and the higher temperature regimes are determined by the macromolecular origin of polymer motions.

1.1.3 Universal Features of the Glass Transition

To understand the nature of the glassy state and of the glass transition represents one of the major challenges in solid state physics [14]. Currently no theory is able to entirely describe all the salient features of this phenomenon.

A glass is formed by cooling a liquid fast enough to avoid crystallization. Continuing supercooling, the viscosity of the liquid increases until the liquid freezes in a noncrystalline solid [4, 5, 15–17]. The glass transition is a purely kinetic phenomenon, which depends on the experimental time scale with respect to the characteristic time of the molecular motions [2, 4, 17]. At a certain temperature on cooling, the molecules will indeed move so slowly that they won't be able to rearrange significantly before the temperature is lowered further. Since these rearrangements are necessary for the system to find the equilibrium, at such temperature some physical quantities start to deviate from their equilibrium values. At lower temperatures, molecular

relaxation times become so long compared to the experimental time scale that the system appears to be frozen. So, glasses can be considered as systems *out of equilibrium* or liquids which are *frozen* in the time scale of the experimental observation.

The glass transition temperature T_g depends on the cooling rate, although in reality the dependence is relatively weak. There are different ways to measure T_g. For calorimetric measurements and volumetric experiments carried out with a typical cooling rate of $T \simeq 10^{-2} K s^{-1}$, the T_g usually coincides with the temperature at which the characteristic relaxation times observed for the α-relaxation by other techniques, like e.g. dielectric spectroscopy (DS), takes the value of

$$\tau_\alpha(T_g) \simeq 10^2 \, s$$

According to another definition referred to the viscosity η, T_g is determined by the following condition

$$\eta_0(T_g) = 10^{13} poise = 10^{12} N m^{-2} s$$

Viscosity measurements at such high values are hard to perform, so they are usually carried out away from the glass transition and the T_g value is extrapolated from the Vogel-Fulcher approximation.

Three main universal features of glass-forming systems near T_g can be pointed out. The first is the *non-Arrhenius* behaviour of the temperature dependence of the α-relaxation time τ or of the viscosity η [4]. In the well-known *Angell's plot* [4], in which the variation of the viscosity η as a function of temperature is represented by scaling viscosity data with the values of $T_g = T_{(log \, \eta = 13)}$ as the scaling temperature, it is shown that only the dynamics of a few liquids can be described by an Arrhenius law (eq.(1.1)). According to the way the characteristic relaxation time approaches the glass-transition temperature strongly non-Arrhenius liquids are classified *fragile*, while those which manifest a behaviour close to Arrhenius-like are classified as *strong*.

Polymers are usually fragile. The temperature dependence of τ_α in fragile systems is usually described in terms of a Vogel-Fulcher function, expressed in eq.(1.2).

Another feature of glass forming systems is the *nonexponential* nature of the reponse of the system to the perturbations [2, 17]. An empirical stretched exponential function, known as Kohlrausch-Williams-Watts (KWW) function, is used to characterize the response function in the time domain [18, 19]. It reads

$$\phi_{KWW}(t) = e^{-(\frac{t}{\tau_w})^\beta} \tag{1.3}$$

τ_w sets the time scale and β, called *shape parameter*, determines the extension of the decay in time: the smaller the β value, the less exponential the response function. Typical β values for fragile supercooled liquids and polymeric systems near T_g are of the order of $\simeq 0.5$ [8]. In real experiments a prefactor $A(Q,T)$ is present. It is a Lamb-Mössbauer factor (LMF) for incoherent scattering or a Debye-Waller factor (DWF) for coherent scattering and it is defined as

$$A(Q,T) = exp\left(-\frac{<u^2>}{3}Q^2\right) \tag{1.4}$$

From a mathematical point of view, the KWW function can be expressed as a superposition of exponential functions

$$\phi_{KWW}(t) = \int g_\tau exp(-t/\tau)d\tau \tag{1.5}$$

The origin of the nonexponential behaviour of the relaxation function of glass forming systems can be interpreted in two extreme scenarios. In the *heterogeneous* one, due to the disorder inherent the system, each particle has a slightly different neighbourhood and relaxes exponentially, but, because of the heterogeneous sets of environments, with different relaxation times τ. The stretching is so caused by the sum of exponential functions with different relaxation times. In the *homogeneous* scenario, all the environments

relax almost identically in an intrinsically nonexponential manner. Though it is generally accepted that heterogeneities are essential ingredients in the dynamics of glass-forming systems, in particular near the glass transition, the question whether the relaxation function is intrinsically exponential is still a subject of debate [20–22].

The third canonical feature of relaxing complex systems is the *nonlinearity* of relaxation for small perturbations [4, 15]. This relates with the fact that, near and below T_g, relaxations are studied on systems out-of-equilibrium, which are nonergodic and evolve toward the equilibrium structure slowly. The time scales are thus very long.

1.1.4 The Mode-Coupling Theory of the Glass Transition

Due to the complexity of the behaviour of glassy systems in the glass transition region there is not a global theory able to describe entirely this phenomenon. It is possible to distinguish two different theoretical approaches, the *phenomenological* and the *microscopic* ones, which attempt to give an exhaustive explanation of the glass transition. The first ones are able to describe some of the phenomena observed in glasses, but some assumptions are not proven and the predictive power is limited [23]. Some examples are the Adam-Gibbs Theory, the Free-volume theory and the Gibbs-DiMarzio theory. Further details can be found in Refs. [24–26]. In microscopic approaches, the physical quantities are calculated from first principles. Since the glassy region is located at quite high temperature, quantum effects can be neglected and the theory sets out on a classical N-body problem.

Introduced in 1984 by Bengtzelius, Götze and Sjölander [27], the *mode-coupling theory, MCT*, represents a microscopic approach to the structural glass transition. The authors have applied to the relaxation of the density fluctuations of a supercooled liquid the mode coupling theory introduced by Kawasaki [28] and the predictions of the MCT can be tested in experiments
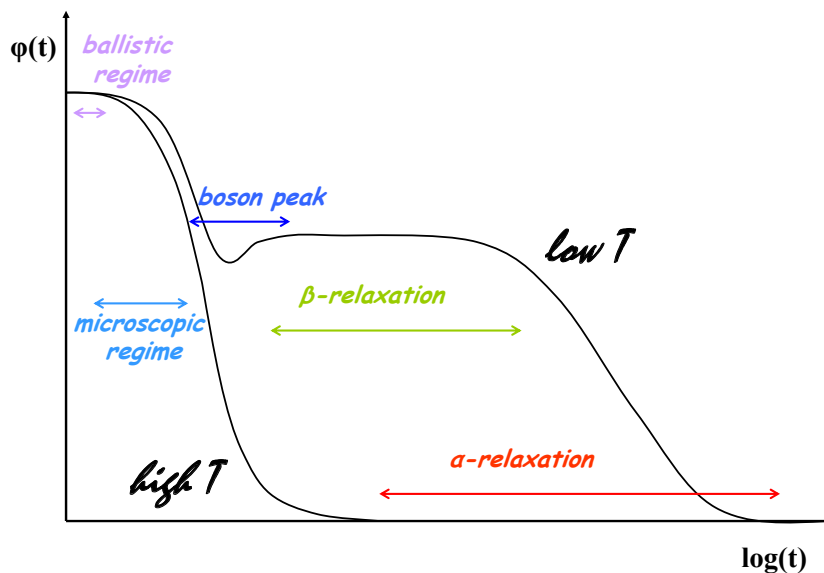
Figure 1.4: Time dependence of a typical correlation function φ at two different temperature, one relatively high and the other in which the relaxation dynamics of the system is already very glassy.

or in computer simulations.

An important feature of the supercooled liquids which is exploited in the MCT is the time scale separation of the main dynamic processes observed in experimental and simulated results. In Fig.1.4 it is schematically shown the behaviour of a typical correlation function φ as a function of time. It can be observed that there are dynamical processes, like vibrations, which occur on a microscopic time scale and other processes, like relaxations, which take place at time scales many orders of magnitude longer than the previous one. While at high temperature it is no possible to define a separation of time scales, at low temperature the *ballistic* and the *microscopic* regime are well separated from the process giving rise to the complete decay of φ. In such condition the correlator φ shows a plateau-like regime at intermediate times, called β-*relaxation*, and, after that, it decays to zero. The process by which the correlator decays to zero is called α-*relaxation* as indicated in Fig. 1.4. In the framework of the MCT, the physical meaning of the plateau is given

by the *cage effect*. At low temperature each particle finds itself surrounded by other particles which form a temporary cage. While at very short times the particles move ballistically, at a certain time they start to feel the cage formed by the others and their movements are limited. So the correlation function relaxes first in the microscopic regime and then, when particles are trapped in the cage, enters in the plateau, where it cannot relax and remains almost constant. Only at much longer times the particles are able to escape from the cage and hence the correlation function starts to decay to zero.

MCT is able to describe this behaviour and predicts some universal features for the correlators. The theory makes use of the separation of the time scale by chosing the density distribution of the particles as the relevant slowly varying observable and by deriving the equations of motions for this slow variable using an *exact* formalism, called Zwanzig-Mori projection operator formalism [29]. The complete derivation of the MCT equations of motions from first principles is rather complex. So here only the involved approximations and the MCT predictions will be discussed. Exhaustive reviews on MCT can be found in Refs. [30–35].

A simple liquid of N identical particles with mass m in a finite volume V is considered. In the strongly supercooled regime, besides fast motions as vibrations around the quasi-equilibrium position, the *microscopic density* $\rho(\mathbf{r}, t)$ will have a slowly varying part. Therefore, the Fourier transformation of $\rho(\mathbf{r}, t)$

$$\rho(\mathbf{q}, t) = \sum_j e^{i\mathbf{q}\mathbf{r}_j(t)}$$

can be chosen as the relevant *slow variable* for the MCT and, assuming that the system is isotropic, the density-density correlator results

$$F(q, t) = \frac{1}{N} < \rho(\mathbf{q}, t)\rho(\mathbf{q}, 0)^* >$$

Using the fundamental Liouville equation of motion and the Mori-Zwanzig projection formalism [36], the *exact* equation of motion for the normalized

density-density correlator $f(q,t) = F(q,t)/S(Q)$, where $S(Q) = F(q, t = 0)$, is found and it reads

$$\ddot{f}(q,t) + \frac{q^2 k_B T}{m S(q)} f(q,t) + \int_0^t dt' M(q, t - t') \dot{f}(q,t') = 0 \qquad (1.6)$$

$M(q, t - t')$ represents the memory kernel. It governs the time dependence of $f(q,t)$ and, within the Mori-Zwanzig formalism, is related to the fluctuating forces.

Eq. (1.6) is not solvable, but it is possible to approximate the memory kernel in order to provide a closed integro-differential equation for the normalized correlator $f(q,t)$ in the long time regime.

The first approximation concerns directly the memory kernel. The expression of the force in the $M(q, t - t')$ contains a coupled pair of modes $\rho(\mathbf{q}_1)\rho(\mathbf{q}_2)$. Since it is assumed that the slow dynamics regime of any observable coupled to density fluctuations can be expressed as a linear combination of "mode pairs", the fast contribution in the fluctuating forces can be neglected [29, 35, 37].

Another crucial approximation is the Kawasaki approximation. The four-point density terms (four-particle correlation function) are factorized into products of two-point density terms (two-particle correlation function) [29, 35].

Finally, the *convolution approximation* leads to a further semplification of the vertices $\mathcal{V}$ in the memory kernel expression: the static three-point correlators are reduced to the product of static structure factors [36, 38]. Nevertheless, it has been demonstrated by Sciortino and Kob [39] that, even if this approximations is well suited for *simple liquids*, it doesn't work so well for liquids characterized by an open network structure or directional interactions. In this case, in fact, additional terms in the computation of the vertices have to be taken into account.

Once such approximations have been performed, the equation (1.6) in the long time regime reduces as following

$$\ddot{f}(q,t) + \frac{q^2 k_B T}{mS(q)} f(q,t) + \frac{q^2 k_B T}{mS(q)} \int_0^t dt' m(q, t-t') \dot{f}(q,t') = 0 \qquad (1.7)$$

in which the memory kernel $m(q, t-t')$ becomes a quadratic function in $f(q,t)$

$$m(q,t) = \frac{1}{2(2\pi)^3} \int d\mathbf{k}\, \mathcal{V}(q,k,|\mathbf{q}-\mathbf{k}|) f(k,t) f(|\mathbf{q}-\mathbf{k}|,t) \qquad (1.8)$$

and the vertex $\mathcal{V}$ is given by

$$\mathcal{V}(q,k,|\mathbf{q}-\mathbf{k}|) = \frac{n}{q^4} S(q)S(k)S(|\mathbf{q}-\mathbf{k}|)\left(\mathbf{q}\left[\mathbf{k}\,c(k) + (\mathbf{q}-\mathbf{k})c\,(|\mathbf{q}-\mathbf{k}|)\right]\right)^2$$
$$(1.9)$$

where n is the particles density and $c(K)$ is the so-called direct correlation function, which is related to the static structure factor via $c(k)\rho = (1 - 1/S(q))$.

It is possible to derive the MCT equation of motion also for a tagged particle [40]. Defining the *self* microscopic density as

$$\rho_s(\mathbf{q}, t) = e^{-i\mathbf{q}\mathbf{r}_j(t)}$$

the *self* density-density correlator becomes

$$F_s(q,t) = \frac{1}{N} < \rho_s(\mathbf{q},t)\rho_s(\mathbf{q},0)^* >$$

The space-time correlation function $F(q,t)$ and $F_s(q,t)$ are usually called coherent and incoherent intermediate scattering functions [36]. Performing the same approximations of the coherent case, the final MCT equations result

$$\ddot{f}_s(q,t) + \frac{q^2 k_B T}{m} f_s(q,t) + \frac{k_B T}{m} \int_0^t dt' m_s(q, t-t') \dot{f}_s(q,t') = 0 \qquad (1.10)$$

$$m_s(q,t) = \frac{1}{(2\pi)^3} \int d\mathbf{k}\, \mathcal{V}_s(q,k,|\mathbf{q}-\mathbf{k}|) f(k,t) f_s(|\mathbf{q}-\mathbf{k}|,t) \qquad (1.11)$$

$$\mathcal{V}_s(q, k, |\mathbf{q} - \mathbf{k}|) = \frac{n}{q^2} S(k) c(k) (\mathbf{q} \cdot \mathbf{k})^2 \qquad (1.12)$$

It is noteworthy to underline that the memory function for the self dynamics contains the normalized coherent intermediate scattering function $f(q, t)$. Since $f_s(q, t)$ describes the dynamics of a tagged particle in its environment, an important input for its time dependence is the time dependence of the relative motion of such particle with respect to the others. This information is indeed provided by $f(q, t)$.

The Eqs. (1.7)-(1.12) are a closed set of equations which define the time dependence of the coherent and incoherent intermediate scattering function. The solutions of this set of equations are correlation functions which can be directly compared with experimental and simulated data.

The expression (1.6) has the form of a damped harmonic oscillator equation with the damping $M(q, t)$ depending on time. With decreasing temperature the vertices, which depend on the static structure factors, become larger, the damping $M(q, t)$ increases and hence the relaxation becomes slower.

It can be deduced a temperature T_c at which the system undergoes a transition from an ergodic to a non-ergodic state. With decreasing temperature in fact the vertices become larger, and the time scale at which the correlators start to decay to zero increases. Thus, there is a critical temperature at which the correlators do not decay to zero.

So far MCT equations have been discussed for one-component monoatomic liquid, but it is relatively straightforward to generalize the discussion to different systems, such as hard [41, 42] and soft [43] spheres, a binary Lennard-Jones mixture [44] and simple aspherical molecules with an intramolecular orientational degree of freedom [45–48]. Experimental checks by NS have been performed with simple model systems, as the molecular system o-terphenyl [49] or simple polymers, like 1,4-polybutadiene (1,4-PB) [50]. Concerning molecular dynamics simulations, realistic polymer models as polyethyelene [51] and 1,4-PB [52, 53] have been analized in terms of the

MCT.

Solutions and Predictions of MCT

The separation parameter $\sigma = (T_c - T)/T_c$ is defined to quantify the relative distance of the temperature of the system to the critical temperature T_c. The following predictions hold only in the limit of small σ, that is for temperature approaching T_c from above and very close to it. It is possible to define the *nonegodicity parameter* f_q as

$$f_q = \lim_{t \to \infty} f(q, t)$$

with

$$f_q = \begin{cases} 0 & \text{liquid state} \\ > 0 & \text{glassy state} \end{cases}$$

It vanishes in an ergodic phase (liquid state) while is nonzero for non-ergodic one (glassy state). Above T_c the nonergodicity parameter f_Q is the critical one, f_Q^c, and it is independent of temperature.

According to MCT predictions, the way in which the α-relaxation time diverges approaching T_c is described by the following law

$$\tau_x(T) = C_x(T - T_c)^{-\gamma} \tag{1.13}$$

in which x denotes a correlator, $\tau_x(T)$ the α-relaxation time, C_x a generic prefactor and γ is a *system universal constant*, independent of the correlator considered.

The *factorization theorem* states that, approaching T_c from above and close to the plateau, the time dependence of the density-density correlator, can be written as

$$f(q, t) = f_q^c + h_q G(t) \tag{1.14}$$

in which f_q^c, the *critical* nonergodicity parameter, represents the height of the plateau, h_q is a q-dependent amplitude, and $G(t)$ is a system universal function, which contains the time dependence of the deviation of $f(q, t)$

17

from its critical value. This theorem represents the *first universality* of the MCT. It states that in the β-relaxation regime the time dependence of all the correlation functions is universal. In fact $f(q,t) - f_q^c$ is a product of two factor, one of which depends on the specific correlator, and the other, $G(t)$, is a scaling function *common* for all the correlators.

$G(t)$ can be expressed as

$$G(t) = \sqrt{|\sigma|}\, g_\sigma(t/\tau_\beta)$$

in which g_σ gives the time dependence of the correlation functions in the β-relaxation regime. The time scale τ_β, defined as the location of the plateau, reads as

$$\tau_\beta = t_0|\sigma|^{1/(2a)}$$

with t_0 a microscopic time scale and a an exponent. Solving analytically the following non linear equation [54]

$$\mp z^{-1} + z g_\sigma^2(z) + i\lambda \int_0^\infty d\tau e^{iz\tau} g_\sigma^2(\tau) = 0$$

two asymptotic solutions can be found

$$g_\sigma(t/\tau_\beta) = (t/\tau_\beta)^{-a} \qquad \text{for } t \ll \tau_\beta \qquad (1.15)$$

$$g_\sigma(t/\tau_\beta) = -B(t/\tau_\beta)^b \qquad \text{for } t \gg \tau_\beta \qquad (1.16)$$

The first functional form is called *critical decay*, while the second is called the *von Schweidler law*. The exponents a, b and the factor λ are related by means of the Γ-function in such way

$$\lambda = \frac{\Gamma(1-a)^2}{\Gamma(1-2a)} = \frac{\Gamma(1+b)}{\Gamma(1+2b)^2} \qquad (1.17)$$

Moreover the exponent parameters a and b are related to the exponent γ of the power-law for the α-relaxation time expresse in eq.(1.13) through the relation

$$\gamma = \frac{1}{2a} + \frac{1}{2b} \tag{1.18}$$

Concerning the α-relaxation, since approaching T_c the relaxation times diverge following the law expressed in eq. (1.13), the long-time decay of any correlator $f(q,t)$ is invariant under scaling by the α-relaxation time τ_α. This important prediction is called *time-temperature superposition principle (TTPS)* and implicates that, at a temperature T, the time dependence of a correlator can be written as follows

$$f(q,T) = \hat{f}(t/\tau(T)) \tag{1.19}$$

with $\hat{f}$ a master function and $\tau(T)$ the α-relaxation time. Even if it is not an analitical solution of the MCT equation, the KWW function, defined in eq.(1.3), is usually used to approximate the shape of the correlators in the long time regime. However, in the limit of $q \to \infty$ of the KWW time τ_w, the MCT predicts that

$$\tau_w \propto q^{-1/b} \tag{1.20}$$

in which b is the von Schweidler exponent.

One of the main prediction of the MCT is the existence of a critical temperature T_c at which the system undergoes a transition from ergodic to a nonergodic state. This feature has stimulated a significative amount of experimental and computational works carried out by different groups with the aim of investigating this singularity [for the references see [55]]. Actually, it is known that, below T_c, hopping processes [56] restore the ergodicity and the sharp transition predicted by the MCT is an anomalous dynamic behaviour in supercooled liquids. Moreover, T_c does not coincide with the *laboratory* glass transition T_g, which tipically results $T_c \approx 1.2\,T_g$ [55, 57, 58].

In spite of this, MCT remains a good dynamical theory for temperature higher than T_c, providing the equation of motion for the normalized density correlator of a simple liquid and making important predictions, as the factorization theorem and the TTSP. Furthemore, all the exponents introduced

in the theory can be obtained from one parameter λ, which is related to the static structure factor $S(Q)$.

1.2 Aqueous Polymer Solutions

1.2.1 Basic features and anomalies of water

Water is the most ubiquitous substance on earth. It is the only chemical compound that occurs naturally in the solid, liquid and vapour phases and it is also the only inorganic liquid present naturally on earth [59]. It plays a fundamental role in natural science since almost all the biomolecules, as proteins or DNA, are inactive in absence of it. Additionally, hydration greatly influences the stability of their structure and their functionality. Concerning industrial fields, water is involved in almost all the processes as a solvent (it is often called the *universal solvent*) as a product, as a reactant or as an impurity.

Water is a compound formed by two hydrogen atoms and an oxygen atom. In the gas phase the HOH angle is $104.5°$ and the OH intramolecular distance is 0.957 Å [60]. Since the geometrical organization of the molecule is not linear and the oxygen electronegativity is higher than that of the hydrogen atoms, the oxygen carries a slight negative charge, whereas the hydrogen atoms a positive one. This gives rise to a dipole moment, which has significant implications. The attraction between an oxygen and an hydrogen atom of different water molecules in fact leads to the formation of a *hydrogen bond*, a bond stronger than van der Waals interaction but weaker than covalent or ionic bond. Even if the hydrogen bond is often described as an electrostatic dipole-dipole interaction, it shares some features with covalent bonding as it is strong and directional, it produces interatomic distances shorter than the sum of van der Waals radii and it involves a limited number of interaction partners. All these characteristics allow water molecules to arrange in a well defined structure as it is found in *ordinary hexagonal ice (Ih)*, the stable form

of water at atmospheric pressure below $273\,K$ [61]. In Ih each water molecule is surrounded by 4 water molecules and acts as a proton donor to two of them and a proton acceptor to the other two. Water molecules are so placed in the vertices of a regular tetrahedron in which the $O - O$ distance is $2.74\,\text{Å}$ and the HOH angle is $109.5°$, a value similar to that found in the gas phase. The tetrahedrally coordinated network of ice is held together by hydrogen bonds and accounts for the unusually low density of ice. Because of the strong directionality of such bonds, the network is indeed an open structure with enough space for other water molecules to exist inside it. Therefore when ice melts at atmospheric pressure, the loss of the long-range order is accompanied by an increase of the density. Besides the ordinary hexagonal ice, water has, in the crystalline state, 13 polymorphs, nine of which are stable over a certain range of temperature and pressure (ices II, III, V, VI, VII, VIII, X, XI, Ih), and four are metastable (ices IV, XI, XII and cubic ice Ic) [62]. Recently, the picture in which water molecules at ambient conditions tend to form a near-tetrahedral hydrogen-bonded structure was questioned. Studies based on X-ray Raman, X-ray absorption and X-ray emission spectroscopy suggest that two distinct types of local structures exist, those tetrahedral as the minority and those highly hydrogen-bond distorted asymmetrical as the majority [63].

Liquid water is characterized by anomalies which in the supercooled regime become more pronounced and have greatly stimulated the research activity [64]. After the publication of Angell's review articles on supercooled water [65, 66] the scientific interest has risen yet more. In the following sections few anomalies of liquid water will be briefly summarized [67, 68].

Density anomaly

The density anomaly is probably the oldest and more known anomaly of liquid water [69]. Whereas at ambient pressure other simple liquids contract upon cooling, below $277\,K$, or $4\,°C$, liquid water begins to expand. This

is the reason for which ice floats on water. Although the magnitude of this effect is small, it has important thermodynamic consequences. The locus of temperatures at which, at fixed pressure, the density is maximum defines water's locus of density maxima, usually referred to as the temperature of maximum density T_{MD}. T_{MD} decreases as the pressure is increased, implying that the isothermal compressibility increases upon cooling, which represents another anomaly of water described in the following.

Isothermal compressibility

The isothermal compressibility measures the volume fluctuations and it is defined as

$$K_T \equiv -\frac{1}{V}\left(\frac{\partial V}{\partial P}\right)_T = \frac{<(\Delta V)^2>}{k_B T V}$$

In contrast to typical liquids in which K_T decreases upon cooling, in water it increases and seems to diverge with a power law at $228\,K$ [68, 70].

Coefficient of thermal expansion

The coefficient of thermal expansion reads as

$$\alpha_P \equiv \frac{1}{V}\left(\frac{\partial V}{\partial T}\right)_P = \frac{P}{k_B^2 T} <\Delta V \Delta S>$$

It measures the cross fluctuations of volume and entropy. Whereas for typical liquids at atmospheric pressure α_P is positive, for water it becomes negative below $277\,K$. This means that for $T < T_{MD}$ increasing the volume the entropy decreases.

Specific heat

The isobaric heat capacity C_p is a measure of how enthalpy H changes with temperature T at constant P. It is related with the entropy in such way

$$C_p \equiv \left(\frac{dH}{dT}\right)_P = T\left(\frac{\partial S}{\partial T}\right)_P = \frac{<(\Delta S)^2>}{k_B}$$

Upon cooling the expected behaviour of C_p should be a decrease, since any thermal fluctuations should decrease. Contrastingly, in the case of water, C_p increases sharply as the temperature is decreased below approximately 330 K [68].

Summarizing, in contrast to what is observed in simple liquids, in water the density and entropy increase upon cooling. Below 277 K, volume and entropy fluctuations are anti-correlated, that means that a decrease in volume corresponds to an increase of the entropy. Such anti-correlation is due to the hydrogen bond network, in which a decrease of the orientational entropy leads to a volume increase. The hydrogen bond network represents the microscopic basis for water's thermal expansion and, as it has been commented, it deeply affects the thermodynamics of liquid water [67].

1.2.2 Liquid, supercooled and glassy water

In Fig. 1.5 the temperature domains of stability and metastability for water at atmospheric pressure are represented [67, 69]. Stable liquid water is found in the range of temperatures between the equilibrium melting point $T_M = 273\,K$ and the boiling point $T_B = 373\,K$. Above the boiling point, water can be superheated, that means heated without boiling, up to 553 K [71]. Bulk water can be supercooled, but it inevitably crystallizes below the homogeneous nucleation temperature $T_H \approx 235\,K$ [71]. Bulk water can be also hyperquenched to a glassy state below the glass transition temperature $T_g = 136\,K$ [72], but it crystallizes on heating around $T_X \approx 150\,K$. As a result there exists a region, comprised between the homogeneous nucleation temperature ($T_H = 235\,K$) and the spontaneous crystallization to ice Ic ($T_X = 150\,K$), in which liquid water cannot be experimentally observed. Such region is usually called *no man's land* [67, 69]. It is worth noting that the T_g value is controversial. Recently, based on the interpretation of calorimetric data, Angell and co-workers argued that such value should be

reassigned to $165 \pm 5 \, K$ [73–77]. At present such issue is still a subject of debate, even if most of experimental observations are consistent with the "conventional" value of $T_g = 136 \, K$.
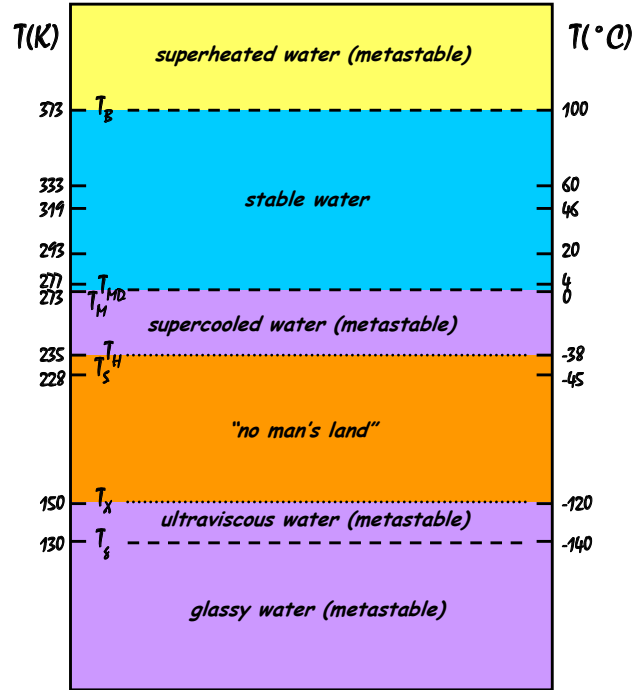

Figure 1.5: Different temperature domains at atmospheric pressure for water [67, 69]. One domain is stable and the others are metastable. On the left side the approximated temperature domains are indicated. T_B indicates the boiling temperature, T_{MD} the maximum density temperature, T_M the melting temperature, T_H the homogeneous nucleation temperature, T_X the crystallization temperature, T_g the glass-transition temperature. Between T_H and T_X the "no man's land" is found, a region in which experiments on the liquid phase cannot be performed. Except the value $T_S \approx 228 \, K$ all the indicated numbers are experimentally observed and correspond to the onset of the anomalies in the sound velocity ($T = 333 \, K$), in the isothermal compressibility ($T = 319 \, K$), in the shear viscosity ($T = 293 \, K$) and in the density ($T = 277 \, K$). First noted by Speedy and Angell [70] T_S is a temperature evaluated by extrapolation at which thermodynamic and dynamic quantities diverge [69, 78] and it is close to the value of the supposed fragile-to-strong crossover temperature.

The homogeneous nucleation temperature T_H represents a kinetic constraint, which depends on the cooling rate and the observation time. It is possible in fact lower the onset temperature of crystallization in water, as

in other liquids, by reducing the concentration of the nucleation-inducing impurities. This is obtained by purifying and subdividing the sample into small droplets. Hence, on supercooling, the lifetime of these droplets becomes smaller compared with the rate of nucleation. Such condition defines a pressure-dependent experimental limit of supercooling, that is the homogeneous nucleation temperature T_H.

Supercooled Water

At atmospheric pressure and upon cooling, the density of supercooled water decreases, while the isothermal compressibility K_T, the magnitude of the thermal expansion α_P, the shear viscosity η and the isobaric heat capacity C_P increase [67].

In supercooled water the first pioneering incoherent quasi-elastic neutron scattering experiments on diffusive motions were performed by Chen *et al.* [79] and Teixeira *et al.* [80]. These authors identified two relaxation times, one short time τ_1 related to rotational motion ($\tau_1 \approx 2\,ps$ at $-20°C$) and one longer time τ_2 related to translational motion of water molecule ($\tau_2 \approx 23\,ps$ at $-20°C$).

Two modes in liquid water were first predicted by molecular dynamics simulations [81]. Then experimental evidences for the high frequency mode were provided by INS experiment [82] and, in stable and supercooled state, by means of IXS (see [67] and Refs. therein). Recently Ruocco and Sette [83] have widely reviewed this issue, but the origin of such high frequency mode propagating at $\approx 3200 ms^{-1}$ in the Q-range of $3.5 - 6\,nm^{-1}$, a value close to the speed of sound in ice and roughly twice than that of ordinary sound in the liquid, is still unclear [83].

Glassy Water

Glassy water, also called *amorphous ice*, is the form of water most common in nature since it is found spectroscopically as a condensed thin film on

interstellar dust in dense molecular clouds and in comets [84, 85]. There exist three known distinct forms of glassy water: *low-density (LDA)*, *high-density (HDA)* and *very high-density amorphous ice (VHDA)*.

LDA has been observed the first time by Burton and Oliver in 1935 by depositing water vapour on a cold plate at low pressure [86]. Rapid cooling small micrometre-sized droplets of liquid water leads to the so-called *hyperquenched glassy water (HGW)*, which was first considered to be different from LDA [87]. Now it is agreed that LDA and HGW are the same amorphous state of water [67, 69]. HDA was discovered by Mishima and co-workers in 1984 by applying pressure to Ih at low temperature [88, 89]. VHDA was discovered recently by Loerting *et al.* by isobaric heating of HDA under pressure from $77\,K$ to 165 or $177\,K$ [90]. Since the term *polyamorphism* means that a pure material can exist in more than one amorphous state, the transitions between the different water's non crystalline forms are named *polyamorphic transition*. They are accompanied by a striking sharp and large volume change, while thermodynamics parameters, such as temperature and pressure, change infinitesimally [69].

Proposed scenarios for explaining the anomalies of water

Although a definitive complete physical picture is still lacking, several interpretations have been developed to explain the anomalies of water. Here two main interpretations are briefly introduced [68, 91]. The *liquid-liquid critical point (LLCP)* scenario has been proposed by Poole and co-workers in 1992 [92]. It arose from molecular dynamics studies on the structure and the equation of state of supercooled water. In the LLCP framework the presence of a second critical point C' with coordinates $T_{C'} \approx 220\,K$, $P_{C'} \approx 100\,MPa$ and $\rho_{C'} \approx 1\,g\,cm^{-3}$ is hypotesized. Above C' the two metastable amorphous phases of ice result indistinguishable, while below C' two distinct phases are found, the low density liquid phase (LDL) at low pressure and the high density liquid phase (HDL) at high pressure. As water near the known

critical point ($T_C = 647\,K$, $P_C = 22\,MPa$ and $\rho_C = 0.328g\,cm^{-3}$) is a fluctuating mixture of molecules whose local structure resembles the liquid and the gas phases, so near the hypotesized second critical point C', it is fluctuating among different structures resembling the LDL and HDL phases. These enhanced fluctuations influence the properties of liquid water, thereby leading to anomalous behaviour.

In the scenario of the *singularity-free hypothesis* Sastry and co-workers showed that the experimental increase in water's response functions is a requirement of thermodynamics [93]. The authors showed that if an anomalous liquid manifests a negative slope of T_{MD}, as water does, then isothermal compressibility increases on decreasing temperature at a constant pressure. They made use of thermodynamic arguments relevant to the behaviour of any anomalous liquid, for which the density decreases on cooling below T_{MD}. They finally commented that anomalous properties and any critical behaviours that might occur in an anomalous fluid are independent issues [93].

1.2.3   Water in a confined geometry

The scientific interest on the study of the structure and the dynamics of water in confined geometry and in mixtures in stable and in supercooled regime has greatly stimulated the research not only with the aim of sheding light on the anomalies of water, but also to elucidate the crucial role played by water in biological processes. On the one hand, by strongly confining, water crystallization on cooling is avoided [91, 94–98] and it is possible to study supercooled water in the "no man's land" (see Fig. 1.5). This opens one possible way to unveil the origin of water anomalies. On the other hand, in all living organisms a significant amount of water molecules is closely associated with biological macromolecules. It means that such water, usually called *biological water*, is found in a range of distances less than $d \lesssim 5\text{Å}$ from proteins, nucleic acids, polysaccharides and it is essential for their structure

and their functions [99]. Therefore it is of the utmost importance to study how water behaves in confined geometry and how it affects its environment.

Fragile-to-Strong Crossover (FSC)

One of the most debated anomalies in water dynamics is the crossover at $T \approx 225\,K$ from *fragile* behaviour at high temperature to *strong* behaviour at low temperature [91, 100]. This anomaly is usually called the *fragile-to-strong crossover (FSC)*, with fragile and strong referring to the terminology introduced by Angell and mentioned in the paragraph 1.1.3 [4]. The temperature in which this crossover takes place is found within the "no man's land", the experimentally inaccessible region for supercooled water. In such context experiments performed in confined geometry and mixtures represent unique ways to study water FSC. Distinct studies have been carried out by different groups, but the issue of the evidence of the FSC is still controversial.

Chen and co-workers studied hydration water of DNA and lysozyme using quasielastic neutron scattering (QENS) spectroscopy and observed that water relaxation times exhibit a crossover at $T_L \approx 222 \pm 2\,K$ from a non-Arrhenius behaviour at high temperature to an Arrhenius behaviour at low temperature [97, 101]. Such scenario is also supported by MD simulations studies performed on bulk water [102] and on lysozyme hydration water [103]. The FSC has been ascribed to a transition of water from high-density liquid to low-density form upon cooling [104]. Above T_L the hydrogen-bond network is not fully developed, while below T_L it is well extended and water results less fluid. On the other hand, investigations performed with different spectroscopic techniques and by different groups show no anomaly in the water relaxation times at $T_L \approx 220 - 225\,K$ [98, 105–107]. Swenson and co-workers challenged the FSC perspective arguing by means of QENS and DS experiments that the FSC is only a result of a decoupling between the structural and the secondary β-relaxation taking place at $T \approx 220 - 225\,K$ [105, 108]. By using dielectric spectroscopy (DS) Sokolov and co-workers

studied the temperature dependence of the conductivity σ of lysozyme hydration water without finding any crossover [106]. The authors suggest that, at the crossover temperature, a secondary relaxation process, which cannot be detected by NS because of the limits of QENS resolution instruments, decouples from the main structural relaxation [106]. By means of ^2H NMR Vogel studied the dynamics of hydration water of elastin and collagen in the range of FSC temperature and objected that water relaxation times show no anomaly in the range of $T \approx 220 - 225\,K$ [98]. Finally, in a very recent work, the same experiment described in Ref. [97] and conducted by Chen *et al.* has been performed by Doster and co-workers on perdeuterated phycocyanin hydration water [107]. Compared to the protocol followed in Ref. [97], they used an improved fitting procedure to analyze the data and no discontinuity in the temperature dependence of the water relaxation times has been found. The authors so suggested that such FSC found in Chen's work is likely to be an artifact of the data analysis. They also commented that previous QENS experiments were motivated by the hope that thin hydration layers would provide a possibility to study supercooled water avoiding crystallization. However, thin hydration layers seem to behave different from bulk water [105, 107].

Biological Water

Biological water is essential for the functioning of macromolecules as proteins, nucleic acids, polysaccharides. It indeed determines their mobility enhancing the biological activity, it enables hydrogen bonding and proton transfer and in general it facilitates the biological processes [99, 109–111].

In biological systems water molecules can be broadly classified into three categories. *Strongly bounded water molecules* are molecules which occupy internal cavities and deep clefts, *hydration water molecules* interact with the macromolecular surface and finally *bulk water* are those water molecules which move freely and can be treated as bulk water [112]. Hydration water

molecules are less structurally defined than the internal ones, are much more mobile and have a significant influence on the dynamics of the biomolecules. Consequenlty the interest in characterizing the dynamics and the structural properties of such molecules and the connection with the biological activity of their environment has become a fundamental topic of research.

Because of the complexity of biomolecules, to study the dynamics and the structure of hydration water simpler systems are also used. Molecular sieves and clays are commonly utilized because they form geometrically well-defined confinements which impede crystallization on cooling (see [113] and Refs. therein). Using this kind of samples it is thus possible to investigate water features in liquid and in supercooled state. Hydrophilic Vycor glasses are also used because they are characterized by pores within water molecules can be organized in different ordered structures.

Aqueous polymer solutions represent a suitable model to mimic biological systems [114, 115]. Although polymers are simpler than biomolecules, they indeed share similarities with them, so representing a significant aid to investigate the role played by water in biological processes and how it affects its surrounding. Moreover, depending on the glass transition of the system, the polymers can appear frozen, allowing to study the water dynamics in a controlled environment.

EXPERIMENTAL TECHNIQUES

2.1 Neutron Scattering

2.1.1 Basic properties of Neutrons

The neutron is a subatomic particle characterized by mass $m = 1.675 \times 10^{-27}$ kg, magnetic moment $\mu = -1.913\,\mu_N$, in which $\mu_N = e\hbar\,/\,2m_p$, spin 1/2 and zero charge. These properties make the interactions short-ranged nuclear and magnetic, therefore the probability that a neutron is scattered by matter is small and it can be described in terms of the first Born approximation. As a consequence the neutrons can usually penetrate into the bulk without distorting the intrinsic properties of the sample. Moreover the magnetic moment makes the neutron a suitable atomistic magnetic probe allowing the interaction with matter through the unpaired electron spins in the atoms [116–120].

In the figure Fig. 2.1 a scheme of a scattering process is shown. The neutron beam, characterized by an initial energy E_0 and initial wavelength $\mathbf{k_0}$ is incident on the sample. Since the interaction probability is small most of the neutrons are transmitted. The neutrons scattered by the sample in the solid angle Ω are characterized by a final energy E and wavelength $\mathbf{k}$
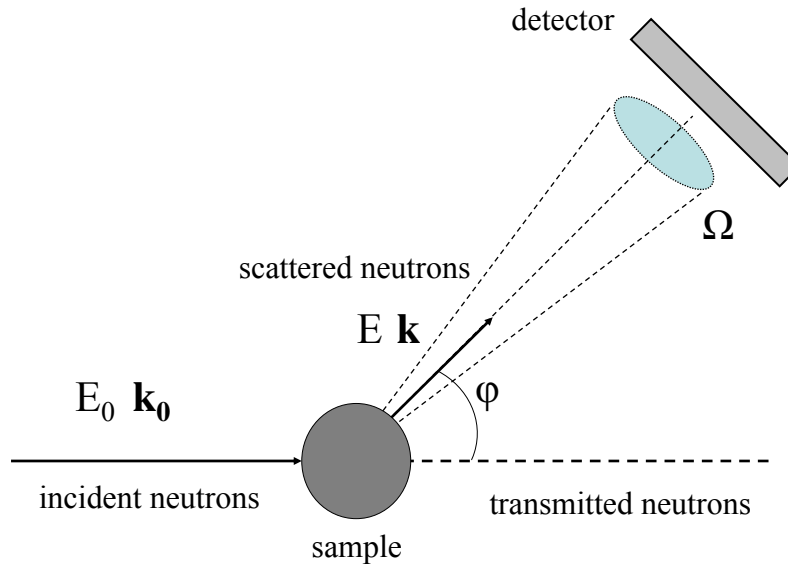
Figure 2.1: Geometry of a neutron scattering experiment.

that can be different from the initial ones. The scattered neutrons will be counted by a detector spanning such solid angle.

The basic physical magnitudes which give information about the neutron scattering process are two: the energy transferred to the sample $\hbar\omega$,

$$\hbar\omega = E - E_0 = \frac{\hbar^2}{2m}(k^2 - k_0^2) \tag{2.1}$$

and the exchanged wave vector $\mathbf{Q}$

$$\mathbf{Q} = \mathbf{k} - \mathbf{k_0} \tag{2.2}$$

The scattering is defined *elastic* when no energy is trasferred to the sample $(E_0 = E)$.

The *inelastic* scattering is found when a neutron loses or gains energy and it is scattered with a final energy and wavelength different from the initial ones $(E_0 \neq E)$.

The *quasielastic* scattering is a type of inelastic scattering involving very

small energy transfers. It is in fact a Doppler effect found when a neutron interacts elastically with a moving particle and its velocity undergoes a Doppler shift. It manifests itself as a broadening of the elastic peak.

The scattering process is therefore associated to a set of $\mathbf{Q}$ and ω values. The scattered intensity depends on both the variables $(\mathbf{Q}, \omega)$ and reveals the sample features under the experimental conditions (temperature, pression, etc.). The relations (2.1) and (2.2) impose kinematic constraints on the experimental feature and the accessible region of the $(\mathbf{Q}, \omega) - space$ is a function of the incident neutron energy [117].

The *scattering length b* is the only parameter which describes the interaction between the neutron and the scattering nucleus. It is a property of each single nucleus and depends in an irregular fashion on its atomic weight A and its atomic number Z. As a consequence, isotopes of single atom species are characterized by different values of the scattering length, the most important example, due for its implications in the soft matter field, is found for hydrogen and deuterium. The contrast variation or selective deuteration techniques take advantage of this property and allow, by a chemical substitution, to label and study a given group of atoms in a sample.

The scattering length also depends on the total spin state of the neutron-nucleus system. In a scattering process between a single isotope with nuclear spin I and a neutron with spin $\frac{1}{2}$, there are two scattering lengths associated to the possible spin state of the neutron-nucleus system: $b^+ = I + \frac{1}{2}$ and $b^- = I - \frac{1}{2}$. Therefore every nucleus with non-zero spin is characterized by two values of the scattering length, while, if the spin of the nucleus is zero, only one value of the scattering length is found.

2.1.2 Theoretical Framework: the Master Formula

The *cross-sections* are the quantities measured in a neutron scattering experiment and they provide information on the characteristic of the sample.

With reference to the scattering experiment shown in Fig. 2.1, the *double*

differential cross section is defined as the number of neutrons which are characterized by an initial energy E_0 and initial wave vector $\mathbf{k_0}$ and are scattered by the sample in a solid angle comprised between Ω and $\Omega + \partial\Omega$ with a final wave vector $\mathbf{k}$ and final energy comprised between E and $E + \partial E$.

It is denoted by

$$\frac{\partial^2 \sigma}{\partial E\, \partial\Omega} = \frac{C}{\Phi N \eta\, d\Omega\, dE} \tag{2.3}$$

in which C is the number of neutrons counted at the detector, η is the efficency of the detector, Φ the flux of incident neutron and N is the number of atoms in the sample.

The *differential cross section* is obtained by measuring the double differential cross section for all the energy transfers E, that means counting the neutrons scattered in the portion of the solid angle $d\Omega$:

$$\frac{\partial\sigma}{\partial\Omega} = \int dE\, \frac{\partial^2 \sigma}{\partial E\, \partial\Omega}$$

It reveals information on the structure but not on the excitations or dynamics of the sample.

The *total cross section* is related to the total number of neutrons scattered and it depends only on $\mathbf{k_0}$

$$\sigma_{tot} = \int d\Omega\, \frac{\partial\sigma}{\partial\Omega}$$

In a scattering process in which the state of the sample changes from the initial one λ_0 to the final one λ, and the state and spin of the neutrons change from $\mathbf{k_0}$ to $\mathbf{k}$ and σ_0 to σ respectively, the differential cross section can be expressed as

$$\left(\frac{\partial\sigma}{\partial\Omega} \right)_{\mathbf{k_0}\lambda_0\sigma_0 \rightarrow \mathbf{k}\lambda\sigma} = \frac{1}{N\Phi d\Omega} W_{\mathbf{k_0}\lambda_0\sigma_0 \rightarrow \mathbf{k}\lambda\sigma} \tag{2.4}$$

The right-hand side of eq. (2.4) represents the number of transitions per second from the state $k_0\lambda_0\sigma_0$ to the state $k\lambda\sigma$ and it is evaluated using

Fermi's Golden Rule

$$W_{\mathbf{k_0}\lambda_0\sigma_0 \to \mathbf{k}\lambda\sigma} = \frac{2\pi}{\hbar} \left| < \mathbf{k}\lambda\sigma \mid V \mid \mathbf{k_0}\lambda_0\sigma_0 > \right|^2 \varrho_{\mathbf{k}\sigma}(E) \qquad (2.5)$$

in which V is the interaction potential between an incident neutron and the sample and $\varrho_{\mathbf{k}\sigma}(E)$ is the density of final states per unit energy rate for neutrons.

Considering a box of volume L^3 containing the incident beam and the sample, the initial and final state of a neutron can be respectively expressed by the wave function

$$\frac{1}{L^{3/2}} e^{i\mathbf{k_0}\mathbf{r}} \mid \sigma_0 > \qquad \frac{1}{L^{3/2}} e^{i\mathbf{k}\mathbf{r}} \mid \sigma >$$

The density of the final state is defined as

$$\varrho(E)\,dE = \left(\frac{L}{2\pi}\right)^3 d\mathbf{k} = \left(\frac{L}{2\pi}\right)^3 k^2\,dk\,d\Omega$$

using the relation (2.1) between energy and wavevector, dE can be calculated and the following expression of $\varrho(E)$ is obtained

$$\varrho(E) = \left(\frac{L}{2\pi}\right)^3 \frac{k}{\hbar^2 m}\,d\Omega \qquad (2.6)$$

With the aid of the De Broglie relation, $p = \hbar k$, the neutron flux Φ can be written as

$$\Phi = \frac{v}{L^3} = \frac{1}{L^3} \frac{\hbar\,k_0}{m} \qquad (2.7)$$

and sustituting Eqs. (2.5), (2.6), (2.7) in (2.4), the differential cross section results

$$\left(\frac{\partial\sigma}{\partial\Omega}\right)_{\mathbf{k_0}\lambda_0\sigma_0 \to \mathbf{k}\lambda\sigma} = \frac{1}{N}\frac{k}{k_0}\left(\frac{m}{2\pi\hbar}\right)^2 \left| < \mathbf{k}\lambda\sigma \mid V \mid \mathbf{k_0}\lambda_0\sigma_0 > \right|^2 \qquad (2.8)$$

Incorporationg in the expression (2.8) the energy conservation condition through a delta function, the double differential cross section is finally obtained

$$\left(\frac{\partial^2\sigma}{\partial\Omega\,\partial E}\right) = \frac{1}{N}\frac{k}{k_0}\left(\frac{m}{2\pi\hbar}\right)^2 \Big|<\mathbf{k}\lambda\sigma\mid V\mid\mathbf{k_0}\lambda_0\sigma_0>\Big|^2\delta(\hbar\omega+E_\lambda-E_{\lambda_0}) \quad (2.9)$$

The so-called *master formula* for neutron scattering results summing over all the final states of the sample λ and the final polarization states of the neutron σ and averaging over all the accessible initial states of the sample λ_0 and of the neutron σ_0

$$\left(\frac{\partial^2\sigma}{\partial E\,\partial\Omega}\right)_{\mathbf{k_0}\rightarrow\mathbf{k}} = \frac{1}{N}\frac{k}{k_0}\left(\frac{m}{2\pi\hbar^2}\right)^2 \sum_{\lambda_0\sigma_0} p_{\lambda_0}p_{\sigma_0}\times$$

$$\times\sum_{\lambda\sigma}\Big|<\mathbf{k}\lambda\sigma\mid V\mid\mathbf{k_0}\lambda_0\sigma_0>\Big|^2\delta(\hbar\omega+E_\lambda-E_{\lambda_0}) \quad (2.10)$$

p_{λ_0} and p_{σ_0} represent the probability that an initial state will occur.

2.1.3   Coherent and Incoherent Scattering

The potential V in the expression (2.10) describes the nucleus-neutron interaction and depends on the scattering length b. The range of the nuclear potential is of the order of $10^{-15}\,m$, that is less than the wavelength of the neutron used in the scattering experiments, the scattering is isotropic and so the interaction potential, called *Fermi pseudopotential*, can be expressed by a delta function

$$V(\mathbf{r}) = \frac{2\pi\,\hbar^2}{m}\,b\,\delta(\mathbf{r}-\mathbf{R})$$

in which $\mathbf{r}$ and $\mathbf{R}$ represent the istantaneous position of the neutron and the nucleus.

The derivation of the cross section pointed out in the previous paragraph is based on the use of Fermi's golden rule, which, for scattering processes, is equivalent to the Born approximation, both based on first-order perturbation theory. This theory does not hold for the case of nucleus-neutron scattering because the interaction potential is very strong. So the Fermi pseudopotential is a formal artifice defined because, in conjunction with the golden rule, it gives the required result of isotropic scattering from a single fixed nucleus.

The interaction between neutrons and sample is obtained through the sum performed over all the atoms

$$V(\mathbf{r}) = \frac{2\pi\,\hbar^2}{m} \sum_i b_i \delta(\mathbf{r} - \mathbf{R}_i) \tag{2.11}$$

For simplicity an unpolarized neutron scattering experiment is considered, in such case, in fact, the dependence on the spin states σ and σ_0 disappers. Evaluating the average of Eq. (2.11) over the neutron wave vectors

$$
\begin{aligned}
< \mathbf{k} \mid V(\mathbf{r}) \mid \mathbf{k}_0 > \ &= \ \frac{2\pi\,\hbar^2}{m} \sum_i b_i \int d\mathbf{r}\, e^{-i\mathbf{k}\,\mathbf{r}} \delta(\mathbf{r} - \mathbf{R}_i) e^{i\mathbf{k}_0\,\mathbf{r}} \\
&= \ \frac{2\pi\,\hbar^2}{m} \sum_i b_i\, e^{-i\mathbf{Q}\,\mathbf{R}_i}
\end{aligned}
$$

the master formula results

$$\frac{\partial^2 \sigma}{\partial E\,\partial\Omega} = \frac{1}{N}\frac{k}{k_0} \sum_{\lambda_0} p_{\lambda_0} \left| \sum_\lambda \sum_i b_i < \lambda \mid e^{-i\mathbf{Q}\,\mathbf{R}_i} \mid \lambda_0 > \right|^2 \delta(\hbar\omega + E_{\lambda_0} - E_\lambda)$$
$$\tag{2.12}$$

In an actual experiment the magnitude measured is not the cross section for a process in which the scattering system goes from a specific state λ_0 to another state λ. Instead the double differential cross section defined in the expression (2.3) is measured. To obtain this quantity it is necessary to sum over all the final states λ, keeping λ_0 fixed, and then average over all λ_0. To carry out this task the Heisenberg operators and a representation of the delta

function by an integral over time are used. The final expression is called the *real-time representation* of the double differential cross section

$$\frac{\partial^2 \sigma}{\partial E \, \partial \Omega} = \frac{1}{N} \frac{k}{k_0} \left(\frac{1}{2\pi\hbar}\right) \int_{-\infty}^{\infty} \sum_{i\,i'} < b_i^* \, b_{i'} \, e^{-i\mathbf{Q}\,\mathbf{R}_i(0)} \, e^{i\mathbf{Q}\,\mathbf{R}_{i'}(t)} > \, e^{-i\omega t} \, dt$$

(2.13)

The angular brackets represent a thermal average of a product of two operators, one involving a particle i at time 0 and the other a particle i' at time t. The connection with the classical mechanics is done regarding $\mathbf{R}_i(t)$ as the actual istantaneous positions of the particles. Furthermore, according to classical statistical mechanics, states can be averaged in configuration space. This means that, if the history of the development of a classical model system over space and time is known, from, for example, a computer simulation experiment, the scattering cross section can be directly calculated using the appropriate time average and compared with neutron scattering results.

In the expression (2.13) the nuclear states are represented by the scattering length b, while the other terms are related to the atomic coordinates $\mathbf{R}_i$. In the case in which the nuclear spins and the isotopes are randomly distributed in any atomic configuration, the atomic state is independent of the nuclear coordinates and it is possible to represent the scattering as a function of the atomic coordinates:

$$\frac{\partial^2 \sigma}{\partial E \, \partial \Omega} = \frac{1}{N} \frac{k}{k_0} \left(\frac{1}{2\pi\hbar}\right) \sum_{i\,i'} \overline{b_i^* \, b_{i'}} \int_{-\infty}^{\infty} < e^{-i\mathbf{Q}\,\mathbf{R}_i(0)} \, e^{i\mathbf{Q}\,\mathbf{R}_{i'}(t)} > \, e^{-i\omega t} \, dt$$

(2.14)

On the assumption of no correlation between the b values of different nuclei

$$\overline{b_i^* b_{i'}} = \overline{|b|^2} \qquad\qquad i = i' \qquad\qquad (2.15)$$

$$\overline{b_i^* b_{i'}} = |\bar{b}|^2 \qquad\qquad i \neq i' \qquad\qquad (2.16)$$

Then

$$\frac{\partial^2 \sigma}{\partial E \, \partial \Omega} = \frac{1}{2\pi\hbar} \frac{1}{N} \frac{k}{k_0} |\bar{b}|^2 \sum_{\substack{i\,i' \\ i \neq i'}} \int <i, i'> e^{-i\omega t} dt +$$

$$+ \frac{1}{2\pi\hbar} \frac{1}{N} \frac{k}{k_0} \overline{|b|^2} \sum_i \int <i, i> e^{-i\omega t} dt = \quad (2.17)$$

$$= \frac{1}{2\pi\hbar} \frac{1}{N} \frac{k}{k_0} |\bar{b}|^2 \sum_{i\,i'} \int <i, i'> e^{-i\omega t} dt +$$

$$+ \frac{1}{2\pi\hbar} \frac{1}{N} \frac{k}{k_0} \{\overline{|b|^2} - |\bar{b}|^2\} \sum_i \int <i, i> e^{-i\omega t} dt \quad (2.18)$$

in which

$$<i, i'> = <e^{-i\mathbf{Q}\,\mathbf{R}_i(0)} \, e^{i\mathbf{Q}\,\mathbf{R}_{i'}(t)}>$$

and

$$\frac{1}{2\pi\hbar} \frac{1}{N} \frac{k}{k_0} |\bar{b}|^2 \sum_i \int <i, i> e^{-i\omega t} dt$$

has been added and subtracted.

In equation (2.18) the first term represents the *coherent* double differential cross section. It depends on the correlations between the position of the same nucleus at different times and on the correlations between the position of an atom i at time 0 with a different atom i' at time t.

The second terms represents the *incoherent* double differential cross section and depends on the correlation between the position of the same atom i at different times.

The double differential cross section can thus be written as the sum of the two components

$$\frac{\partial^2 \sigma}{\partial E \, \partial \Omega} = \left(\frac{\partial^2 \sigma}{\partial E \, \partial \Omega}\right)_{coh} + \left(\frac{\partial^2 \sigma}{\partial E \, \partial \Omega}\right)_{inc}$$

in which

$$\left(\frac{\partial^2 \sigma}{\partial E \, \partial \Omega}\right)_{coh} = \frac{1}{N} \frac{\sigma_{coh}}{4\pi} \frac{k}{k_0} \frac{1}{2\pi\hbar} \sum_{i \, i'} \int_{\infty}^{\infty} < e^{-i\mathbf{Q}\,\mathbf{R}_i(0)} \, e^{i\mathbf{Q}\,\mathbf{R}_{i'}(t)} > e^{-i\omega t} dt$$

(2.19)

$$\left(\frac{\partial^2 \sigma}{\partial E \, \partial \Omega}\right)_{inc} = \frac{1}{N} \frac{\sigma_{inc}}{4\pi} \frac{k}{k_0} \frac{1}{2\pi\hbar} \sum_{i} \int_{\infty}^{\infty} < e^{-i\mathbf{Q}\,\mathbf{R}_i(0)} \, e^{i\mathbf{Q}\,\mathbf{R}_i(t)} > e^{-i\omega t} dt$$

(2.20)

with $\sigma_{coh} = 4\pi \, |\bar{b}|^2$ and $\sigma_{inc} = 4\pi \, \{\overline{|b|^2} - |\bar{b}|^2\}$.

Because of the feature of the scattering length b, an incoming neutron is affected by a scattering potential which varies in a discontinuos manner among the atoms forming the sample. Only the average scattering potential can give interference effects and thus coherent scattering. This average is proportional to $\bar{b}$ and the coherent scattering cross section thus results to be proportional to $|\bar{b}|^2$. The deviations from the average scattering potential are randomly distributed and cannot give interference effects, they give incoherent scattering proportional to the deviation of the scattering length from their average value.

2.1.4 Correlation functions in neutron scattering

The physical magnitudes calculated in the previous paragraph can be expressed in terms of correlation functions that are thermal averages of operators belonging to the sample. This formulation is due primarily to Van Hove (1954) and is referred as the *Van Hove formalism* [119].

The double differential cross section can be defined in terms of the *coherent* and *incoherent scattering function* as

$$\left(\frac{\partial^2 \sigma}{\partial E \, \partial \Omega}\right)_{coh} = \frac{k}{k_0} \frac{\sigma_{coh}}{4\pi} \, S(\mathbf{Q}, \omega)$$

(2.21)

$$\left(\frac{\partial^2 \sigma}{\partial E \, \partial \Omega}\right)_{inc} = \frac{k}{k_0} \frac{\sigma_{inc}}{4\pi} \, S_{inc}(\mathbf{Q}, \omega)$$

(2.22)

with

$$S(\mathbf{Q}, \omega) = \frac{1}{2\pi\hbar} \int_{-\infty}^{\infty} dt \, e^{-i\omega t} S(\mathbf{Q}, t) \tag{2.23}$$

$$S_{inc}(\mathbf{Q}, \omega) = \frac{1}{2\pi\hbar} \int_{-\infty}^{\infty} dt \, e^{-i\omega t} S_s(\mathbf{Q}, t) \tag{2.24}$$

These functions are the Fourier transform in time of the *intermediate scattering function* and of the *self-intermediate scattering function* respectively

$$S(\mathbf{Q}, t) = \frac{1}{N} \sum_{i\,i'} < e^{-i\mathbf{Q}\,\mathbf{R}_i(0)} e^{i\mathbf{Q}\,\mathbf{R}_{i'}(t)} > \tag{2.25}$$

$$S_s(\mathbf{Q}, t) = \frac{1}{N} \sum_{i} < e^{-i\mathbf{Q}\,\mathbf{R}_i(0)} e^{i\mathbf{Q}\,\mathbf{R}_i(t)} > \tag{2.26}$$

The double differential cross sections, expressed in equations (2.21) and (2.22), are so given by the product of two factors: the first is totally related to the scatterer atoms, while $S(\mathbf{Q}, \omega)$ is determined solely by the structural and the dynamical properties of the sample.

The *space-time correlation function* and the *self-space-time correlation function*, also called *Van Hove correlation functions*, are the Fourier transform in space of the corresponding intermediate scattering function:

$$G(\mathbf{r}, t) = \frac{1}{(2\pi)^3} \int d\mathbf{Q} \, e^{-i\mathbf{Q}\,\mathbf{r}} S(\mathbf{Q}, t) \tag{2.27}$$

$$G_s(\mathbf{r}, t) = \frac{1}{(2\pi)^3} \int d\mathbf{Q} \, e^{-i\mathbf{Q}\,\mathbf{r}} S_s(\mathbf{Q}, t) \tag{2.28}$$

They are therefore the Fourier transform in space and in time of the coherent and incoherent scattering functions.

The physical meanings of such correlation functions is better understood introducing the *particle density operator* and the corresponding operator in the reciprocal space:

$$\rho(\mathbf{r}, t) = \sum_i \delta(\mathbf{r} - \mathbf{R}_i(t))$$

$$\rho_{\mathbf{Q}}(t) = \int d\mathbf{r} \, \rho(\mathbf{r}, t) e^{i\mathbf{Q}\,\mathbf{r}} = \sum_i e^{i\mathbf{Q}\,\mathbf{R_i}(t)}$$

So, it results

$$S(\mathbf{Q}, t) = \frac{1}{N} < \rho_{-\mathbf{Q}}(0)\rho_{\mathbf{Q}}(t) > \tag{2.29}$$

The intermediate scattering function and thus $S(\mathbf{Q}, \omega)$ are now expressed in terms of a density-density correlation function. As coherent nuclear scattering is concerned, the interaction potential couples the neutron to the density of the target system. $S(\mathbf{Q}, \omega)$ is thus determined by spontaneuos density fluctuations in the sample and gives information on its structure and its dynamics.

Giving special attention to the fact that the operators $\mathbf{R_i}(0)$ and $\mathbf{R_{i'}}(t)$ do not commute except when $t = 0$ and using the properties of the delta function, the space-time correlation function can be evaluated in terms of the particle density operators

$$G(\mathbf{r}, t) = \frac{1}{N} \int d\mathbf{r'} < \rho(\mathbf{r'} - \mathbf{r}, 0)\rho(\mathbf{r'}, t) > \tag{2.30}$$

with

$$\int d\mathbf{r} \, G(\mathbf{r}, t) = N$$

and the space-time correlation functions assume the so-called *classical* form

$$G^{cl}(\mathbf{r}, t) = \frac{1}{N} \sum_{i\,i'} < \delta(\mathbf{r} - \mathbf{R}_{i'}(t) + \mathbf{R}_i(0)) > \tag{2.31}$$

$$G_s^{cl}(\mathbf{r}, t) = \frac{1}{N} \sum_i < \delta(\mathbf{r} - \mathbf{R}_i(t) + \mathbf{R}_i(0)) > \tag{2.32}$$

So $G^{cl}(\mathbf{r}, t)\, d\mathbf{r}$ and $G_s^{cl}(\mathbf{r}, t)\, d\mathbf{r}$ represent the probability that, given a particle i in the origin at time $t = 0$, any particle i' including the original particle i, or only the same particle i in the self case, is in the volume $d\mathbf{r}$ at position $\mathbf{r}$ at time t.

At time $t = 0$ the operators commute, so

$$G_s^{cl}(\mathbf{r}, 0) = \delta(\mathbf{r})$$

and the expression (2.31) becomes

$$G^{cl}(\mathbf{r}, 0) = \sum_{i,i'} <\delta(\mathbf{r} - \mathbf{R}_i + \mathbf{R}_{i'})> = \delta(\mathbf{r}) + g(\mathbf{r}) \qquad (2.33)$$

with

$$g(\mathbf{r}) = \sum_{i \neq i'} <\delta(\mathbf{r} - \mathbf{R}_i + \mathbf{R}_{i'})> \qquad (2.34)$$

The physical magnitude $g(\mathbf{r})$ is known as the *static pair correlation function* and gives the average particle density with respect to a given particle.

The zeroth moment of the scattering function $S(\mathbf{Q}, \omega)$ is known as the *static structure factor* and it is denoted as $S(\mathbf{Q})$:

$$S(\mathbf{Q}) = \int_{-\infty}^{\infty} d(\hbar\omega) S(\mathbf{Q}, \omega) = S(\mathbf{Q}, 0)$$

So

$$S(\mathbf{Q}) = \frac{1}{N} \sum_{ii'} <e^{i\mathbf{Q}[\mathbf{R}_{i'} - \mathbf{R}_i]}>$$

$$= 1 + \int g(\mathbf{r})\, e^{i\mathbf{Q}\mathbf{r}} d\mathbf{r}$$

In the case in which the scattering is isotropic and $g(\mathbf{r})$ depends only on $|\mathbf{r}|$, the static structure becomes

$$S(Q) = 1 + \frac{4\pi}{Q} \int_0^{\infty} dr\, [g(r) - \rho] \sin(Qr)\, r$$

The elastic scattering is related to the function $G(\mathbf{r}, t)$ and $S(\mathbf{Q}, t)$ evaluated at $t = \infty$. The intermediate scattering function can be written, in fact, as a sum of two terms, one depending on the time and which tends to zero in the limit of $t = \infty$ and the other one being the limiting value:

$$S(\mathbf{Q}, t) = S(\mathbf{Q}, \infty) + S'(\mathbf{Q}, t) \tag{2.35}$$

Substituing the expression (2.35) in the definition (2.23) of $S(Q, \omega)$

$$S(\mathbf{Q}, \omega) = \frac{1}{2\pi\hbar} \int_{-\infty}^{\infty} dt \, [S(\mathbf{Q}, \infty) + S'(\mathbf{Q}, t)] e^{-i\omega t} =$$

$$= \frac{\delta(\omega)}{\hbar} S(\mathbf{Q}, \infty) + \frac{1}{2\pi\hbar} \int_{-\infty}^{\infty} dt \, S'(\mathbf{Q}, t) e^{-i\omega t} \tag{2.36}$$

in which the former term represents the elastic scattering, while the latter the inelastic one. The coherent double differential cross section can thus be expressed as a sum of the elastic and inelastic part

$$\left(\frac{\partial^2 \sigma}{\partial E \, \partial \Omega} \right)_{coh} = \left(\frac{\partial^2 \sigma}{\partial E \, \partial \Omega} \right)_{coh}^{el} + \left(\frac{\partial^2 \sigma}{\partial E \, \partial \Omega} \right)_{coh}^{inel} \tag{2.37}$$

For a bulk sample, in the limit of $t \to \infty$ the time-dependent part cannot contribute because it tends to zero, while the correlation between $\mathbf{R}_i(0)$ and $\mathbf{R}_{i'}(t)$ becomes independent of t. In such limit, the following expression for the coherent elastic double differential cross section is thus obtained

$$\left(\frac{\partial^2 \sigma}{\partial E \, \partial \Omega} \right)_{coh}^{el} = \frac{k}{k_0} \frac{\sigma_{coh}}{4\pi} \frac{\delta(\omega)}{\hbar} S(\mathbf{Q}, \infty) = \frac{k}{k_0} \frac{\sigma_{coh}}{4\pi} \frac{\delta(\omega)}{\hbar} \left| \int d\mathbf{r} < \rho(\mathbf{r}) > e^{i\mathbf{Q}\mathbf{r}} \right|^2$$

In this condition there is no correlation also between the density functions on which the space-time correlation function depends, so the equation (2.30) can be written as

$$G(\mathbf{r}, \infty) = \frac{1}{N} \int d\mathbf{r}' < \rho(\mathbf{r}' - \mathbf{r}) > < \rho(\mathbf{r}') >$$

and, for the case of liquids and gases in which the density is uniform, it results

$$G(\mathbf{r}, \infty) = \frac{1}{N} \int d\mathbf{r}' \rho^2 = \rho$$

In the case of incoherent elastic scattering, integrating over the energy E, the following expression of the differential cross section is obtained

$$\left(\frac{\partial \sigma}{\partial \Omega} \right)_{incoh}^{el} = \frac{\sigma_{inc}}{4\pi} S_s(\mathbf{Q}, \infty) = \frac{\sigma_{inc}}{4\pi} \int d\mathbf{r} \, G_s(\mathbf{r}, \infty) \, e^{i\mathbf{Q}\mathbf{r}}$$

Summarizing, the *coherent scattering* gives information about the relative positions and motions of *different* particles in the system. From this scattering it is possible to gain information on the *structure* of the sample, through the evaluation of the *pair correlation function* and the *static structure factor*. The evolution of the pair correlation function in time, the *dynamic structure factor*, reveals the collective dynamics in the sample. In particular, at low values of momentum transfer it shows effects due to excitations of cooperative modes. The information provided by the *incoherent scattering* relates to the motion of a *single* particle.

2.1.5 Experimental section

The characteristics of the neutron beam energy and of the time structure of the flux, pulsed or continuous, are important factors to determine which kind of dynamical or structural investigation is well suited to a particular source and to establish the design of the spectrometers [118]. These characteristic are determined by the type of the source and by the thermic moderators, i.e. the environment through which the neutrons pass immediately after production. H_2O, D_2O and graphite are usually used as thermic moderators. They slow down the neutrons acting directly on their kinetic energies. Once slowed down, neutrons are classified as cold, thermal and hot. In the table 2.1 typical energy, temperature and wavelentgh ranges are shown [119].

Quantity	Cold	Thermal	Hot
Energy E(meV)	0.1-10	5-100	100-500
Temperature T(K)	1-120	60-1000	1000-6000
Wavelength $\lambda(\mathring{A})$	30-3	4-1	1-0.4

Table 2.1: Typical energy, temperature and wavelength range for the three types of source in a reactor

In both, reactor and spallation sources, guides allow neutrons from the source to arrive to the instruments, where they interact with the sample. The detectors count the scattered neutrons through a process of absorption by a suitable nucleus followed by the detection of the charged particles produced.

The neutron scattering experiments carried out in this study were performed at the Institute Laue-Langevin (ILL), a reactor source placed in Grenoble, France, and at the Paul Scherrer Institute (PSI), a continuous spallation source placed in Villigen, Switzerland. In the next section characteristics and details of the instruments used will be given.

2.1.6 Neutron sources

The reactor

In a reactor source fast neutrons are generated by a fission chain reaction often from enriched uranium ^{235}U. The fast energy region corresponds to the region in which neutrons are produced. In the intermediate or epithermal region thermic moderators slow down the neutrons. Finally, when neutrons reach the thermal equilibrium with the moderator, the energy spectrum is described by a Maxwell-Boltzmann distribution with a characteristic effective temperature.

The core of the High Flux Reactor at the ILL consists of a single fuel element made of highly enriched ^{235}U with a mass of $\sim 8.57\,kg$. There are

three moderators at different temperatures to reach a wide range of neutron spectra. One is a hot source consisting of a graphite block and two cold moderators which consist of a vertical cold source (VCS) and of an ultra cold neutron source [121].

The spallation source

The spallation reaction is a process in which heavy energetic particles, such as $1\,GeV$ protons, splinter neutrons from heavy nuclei of a particular target. The reaction is a sequential one involving the incorporation of the incident proton by the target nucleus followed by an internal cascade, an internuclear cascade, in which a high energy neutron is expelled, and an evaporation process in which the target nuclei de-excitate by the emission of several low energy neutron and other particles. The neutrons produced by this kind of source have high energies. It is possible to create a continuous spallation source by feeding the accelerated protons in a storage ring and smearing out the pulse structure.

SINQ is a continuous spallation neutron source driven by (PSI)'s 590 MeV proton accelerator, characterized by a stable proton current of 2.3 mA [122–124]. Thermal neutrons are extracted in four sectors of the target block and the thermal neutron flux is in the range of $10^{14}\,cm^2s^{-1}$, while in other two sectors cold neutrons are extracted.

2.1.7 Neutron scattering instruments

Time-of-Flight spectrometer

According to the De Broglie relation, $\lambda = h/mv$, neutrons with different energies and hence different wavelengths travel with different velocities. Therefore higher energy neutrons are faster and arrive to the detector in less time than the slower ones. Knowing the starting time t_0, the distance l_0 between the sample and the detector and the time t_{flight} it takes a neutron

to arrive to the detector it is possible to calculate the neutron velocity and hence its energy. This is the way of working of a Time-of-Flight (ToF) spectrometer. The neutrons are counted as a function of the detector angle θ and the time-of-flight t_{flight}. The intensity recorded is characterized by an asymmetric appereance because of the non linear dependence of the energy exchange on the t_{flight}

$$\hbar\omega = \left(\frac{l_1^2}{(l_0 - \sqrt{2E_0/m}\, t_{flight})^2} - 1 \right) E_0$$

in which l_1 is the distance between the chopper and the sample.

Due to the wide $\hbar\omega$-range covered in these experiments, the spectra of a single detector at angle θ correspond to a curved line in the (Q,ω) plane [125].

FOCUS is a time and space focusing ToF spectrometer placed at the cold neutron guide $RNR\,11$ in SINQ, PSI. The white beam is reduced by a preselector disk chopper, this with a Be-filter is used also to suppress higher order contamination. A monochromator focuses the beam on the sample through a Fermi-chopper, scattered neutrons pass a $2.5\,m$ flight distance before being detected [126, 127]. A scheme of the instrument is shown in Fig. 2.2.

Backscattering spectrometer

The backscattering spectrometers (BS) work in *inverse geometry* [120]. The neutrons scattered by the sample are energy-analysed by means of Bragg-scattering, which means that only those neutrons with specific wavelength/energy to satisfy the Bragg condition are directed toward the detectors. In such spectrometers the final neutron energy is therefore fixed and the initial energy of the incident neutrons varies around this value [120, 128]. The backscattering process is drawn in figure 2.3 and the high-energy resolution is obtained working at the largest possible Bragg angle. In fact, the
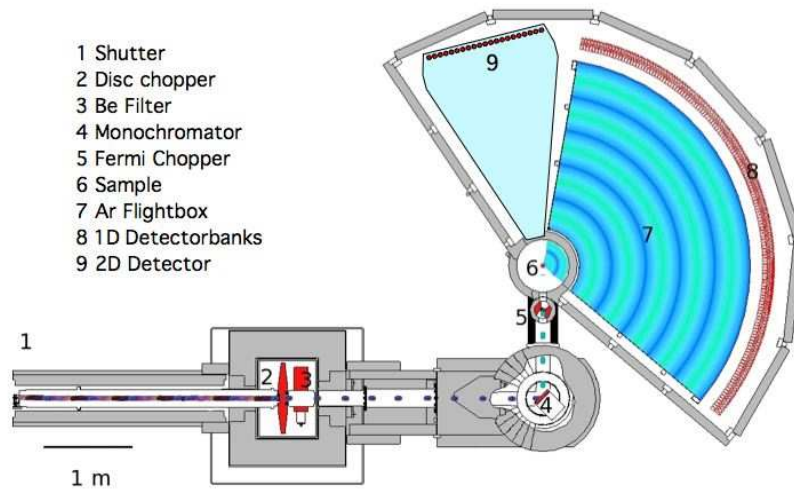
Figure 2.2: Geometry of the ToF spectrometer FOCUS, PSI, Zurich.

differential of the Bragg law $\lambda = 2\,d\,sin\theta$ is

$$\frac{\Delta E}{E} = \frac{2\Delta\lambda}{\lambda} = 2cot\theta\Delta\theta + \frac{2\Delta d}{d}$$

and it is minimized when $\theta = 90°$.

In some inverted geometry spectrometers, as IRIS at ISIS, the ToF technique is used for the data analysis to detect the energy exchange within the sample [128, 129]

The IN16 spectrometer is located at the $H53$ cold guide at ILL [130]. In such instrument perfect crystals act as monochromator and analyzers, the instrumental resolution is optimized by using backscattering geometry at both crystals and the variation of the neutron incident energy is obtained by a Doppler motion of the monochromator [131].

Schematically shown in Fig. 2.4, IN16 consists of two spectrometers. In the first one a graphite deflector, a Beryllium filter and a chopper focus the
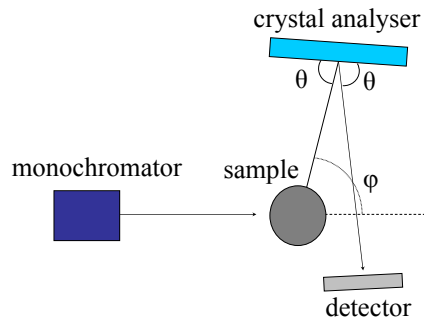
Figure 2.3: Inverse-geometry inelastic neutron scattering experiment.

white beam of the neutron guide suppressing high order contamination. After that, a second graphite deflector sends periodically the monochromatic neutrons to a spherically curved monochromator in nearly exact backscattering. This spherical monocromator is mounted on a mechanical crankshaft velocity drive (the Doppler drive) operating at a variable frequency and constant amplitude. In the secondary spectrometer, the analysers cover the full angular range and the neutrons are counted with a multidetector.

Neutron Spin-Echo spectrometer

Neutron spin echo (NSE) is distinguished from all other dynamic neutron scattering techniques in that it measures directly the velocity change of each neutron individually during scattering [8, 132–134]. A neutron, entering in a region with a magnetic field perpendicular to its magnetic moment, will undergo Larmor precession with a frequency

$$\omega_L = \gamma B$$

being B the magnetic field and $\gamma = 1.83033 \times 10^8 \, radian/sT$ the gyromagnetic ratio of the neutron.

In a NSE spectrometer a longitudinally polarized neutron beam is sent through a $\pi/2$ flipper so the neutron spins rotate 90° resulting perpendicular to the direction of the beam. After leaving the flipper, neutrons enter in the
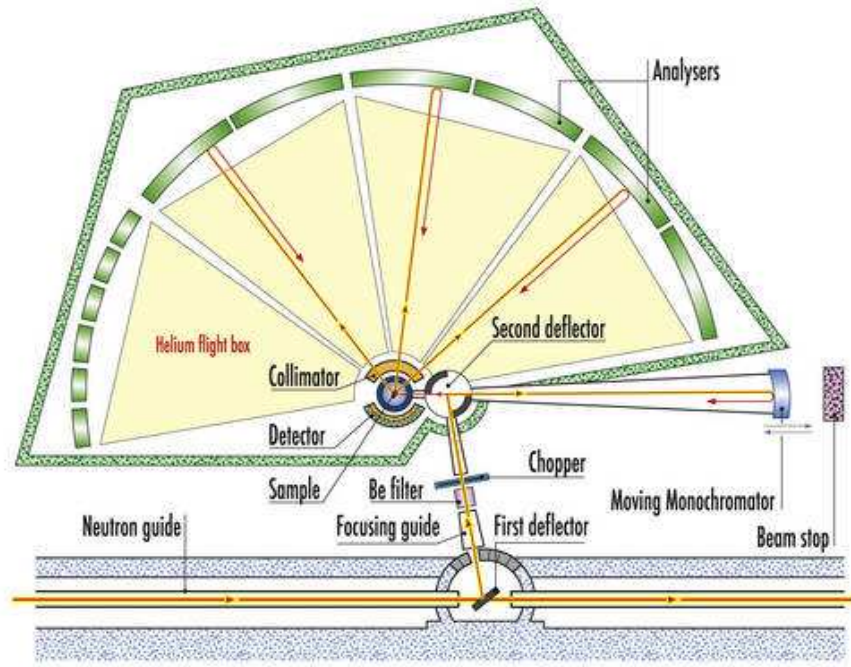
Figure 2.4: Geometry of the backscattering spectrometer IN16, ILL, Grenoble.

primary solenoid and start the precession around the magnetic field B. If l is the length of the solenoid, the total precession angle of a neutron will be

$$\varphi = \frac{\gamma B l}{v}$$

Arriving at the sample, different neutrons with different velocities have total precession angles that differ proportionally, but the precession angle of a spin single out a specific neutron and is related to its velocity. Near the sample a π flipper is placed. Its function is to reverse the scattered neutrons precession plane around the beam axis. After that, the neutrons enter in the secondary solenoid, perform the same number of precessions as in the first one and arrive to a second $\pi/2$ flipper with all the spins pointing upwards. The function of the second $\pi/2$ flipper is to stop the precession and turns the polarization in the direction of the analyzer, irrespectively of the neutron velocities. *Spin-*

51

echo is referred to the entire process of refocusing of precessing neutron spin magnetization.

The analyzer transmits only the neutrons with spin component parallel to the axis, so the spin projection to the axis determines the probability that a neutron reaches the detector. If a neutron undergoes a velocity change during the scattering, the final spin direction is no longer upwards, the neutron doesn't reach the detector and the echo signal is reduced. So the cosine of the final precession angle determines the transmission.

In an inelastic scattering process the total precession angle results

$$\varphi_{tot} = \frac{\hbar \gamma B l}{m v^3} \omega$$

and $< cos\varphi >$ will be the expected value over all the scattered neutron. In general, in an inelastic neutron scattering experiment, the scattering probability is given by $S(Q, \omega)$. The beam polarization measured thus results

$$< cos\varphi >= \frac{\int cos(t_{NSE} \omega) S(Q, \omega) d\omega}{\int S(Q, \omega) d\omega} = S(Q, t)$$

with

$$t_{NSE} = \frac{\hbar \gamma B l}{m v^3}$$

NSE directely measures the intermediate scattering function. The maximun t_{NSE} avalaible, that is the resolution, depends linearly on the magnetic field and on the third power of the neutron wavelength. Thus, using cold neutrons allows reaching long Fourier times. In practice, due to the polarization process, the measured signal is obtained by the difference between the non-spin flipped and the spin flipped neutrons, such that

$$S_{NSE}(Q, t) = \frac{S_{coh}(Q, t) - \frac{1}{3} S_{inc}(Q, t)}{S_{coh}(Q, 0) - \frac{1}{3} S_{inc}(Q, 0)} \tag{2.38}$$

Placed at the cold neutron guide $H141$ at ILL, $IN11$ has three configuration as it is shown in Fig. 2.5.

The option $IN11A$ is a 2-dimensional multidetector with a very high energy resolution. $IN11C$ has 41 detectors distributed over an angle of $30°$
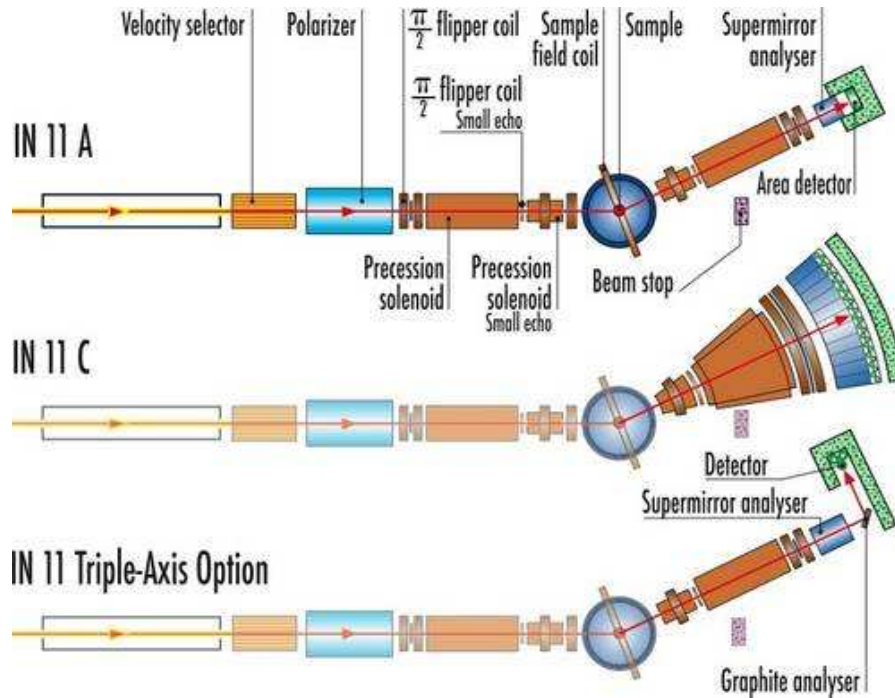
Figure 2.5: Geometry of the NSE spectrometer IN11, ILL, Grenoble.

in the horizontal plane and offers a high count rate while the energy resolution is lower. The triple axis configuration was designed to increase the sensitivity to small energy transfers.

2.1.8 Neutrons: a suitable probe for soft matter

Thermal neutrons are a very powerful tool to investigate condensed matter. In fact they are characterized by energies of the same order of the energies of excitations in soft matter and their wavelength is comparable with the usual molecular dimension or with the inter-molecular space.

In structural studies X-rays can represent a valid alternative to the neutron techniques [119, 125]. In fact, X-ray diffraction and small angle X-ray scattering cover the same range of spatial resolution of neutron diffraction and small angle neutron scattering. Moreover X-rays have high intensities and there is no incoherent scattering. On the other hand, X-rays are scat-

tered by electrons and hence the interaction with the sample depends on a form factor which increases with the atomic number Z, while neutrons are scattered by nuclei. The neutron form factor, that is the scattering length b, does not depend on the wavevector Q, it is a proper characteristic of the isotopes and it varies randomly throughout the periodic table. The very advantage of neutron scattering is thus represented by the possibility of isotopic substitution, which allows to measure partial structure factors. Due to the big difference between the Hydrogen and Deuterium scattering length and to the large amount of these atoms in biological and polymeric samples, the H/D isotopic substitution has been greatly exploited in soft matter studies. In the table 2.6 are shown the values of H and D scattering lengths.

	$b_{coh}\,(fm)$	$b_{inc}(fm)$	$\sigma_{coh}\,(10^{-24}\,cm^2)$	$\sigma_{inc}\,(10^{-24}\,cm^2)$
H	-3.7409	25.274	1.76	80.26
D	6.674	4.04	5.59	2.05
C	6.6484	0	5.551	0.001
O	5.805	0	4.232	0.00

Figure 2.6: Scattering lengths and cross sections of PVME atoms.

In dynamical study the selective deuteration technique also plays a fundamental role making neutrons a unique probe for condensed matter. In fact, it is possible to label a single part of a macromolecule and selectively investigate its dynamics or label an entire molecule and study it, in contrast with the environment. Due to the high value of H incoherent cross section, the experiments carried out on a protonated sample lead information on the single particle motion of hydrogens, while deuterated sample are needed to investigate the collective dynamics.

2.2 Complementary experimental techniques

To better clarify the structure and the dynamics of the samples it has been made use of complementary experimental techniques which will be outlined in the following.

X-ray scattering

X-radiation (*X-rays*) is an electromagnetic radiation characterized by a wavelength comprised in the range of 0.5 to 2 Å [135]. Along with fast electrons, thermal neutrons and X-rays are used in diffraction studies of the structure of matter. Since the scattering principles and the specific case of neutron scattering have been deeply treated, in the following X-radiation will be discussed.

Fig. 2.1 can be generalized to a scheme of a scattering experiment. A monochromatic beam (neutrons or X-rays) is incident on a sample, which generates scattering waves. The scattering amplitude is the parameter which describes the interaction between the incident wave and the target sample. In the case of X-rays, since the mass of the nuclei is more than 10^3 times greater than the electron mass and the nuclear scattering energy is accordingly 10^6 times less than the electron scattering energy, the scattering amplitude is determined by the interaction between the incident radiation and the electrons [135]. Furthermore, in the case of weakly scattering centers the first Born approximation is fulfilled. The scattering amplitude is thus related through the Fourier transforms to the potential field, which in the case of X-rays is the distribution of the electron charge density $\rho(\mathbf{r})$.

Therefore, the scattering of X-rays from an atom, being the X-ray energy large compared with the binding energy of all of the electrons in the atom, is described in terms of scattering amplitude or the so-called *atomic form factor* $f(\mathbf{s})$

$$f(\mathbf{s}) = \frac{1}{2\pi} \int \rho(\mathbf{r}) e^{i\mathbf{s}\mathbf{r}} d\mathbf{r}$$

with $\mathbf{s} = \mathbf{k} - \mathbf{k}_0$ the scattering vector and $|\mathbf{s}| = 4\pi\frac{sin(\theta)}{\lambda}$, being 2θ the scattering angle, λ the wavelength of the incident radiation and $\mathbf{q} = \mathbf{s}/2\pi$ the change in the momentum of X-rays [135].

For spherically simmetric atoms $\rho(\mathbf{r}) = \rho(r)$ and $f(\mathbf{s})$ results

$$f(s) = 4\pi \int_0^\infty r^2 \rho(r) \frac{sin(sr)}{sr} dr \tag{2.39}$$

The atomic form factors for all free atoms and most of the chemically significant ions have been calculated using the best wave functions available and they are listed in X-ray crystallography tables [136]. The analytic approximation to the form factors reads as

$$f(\lambda^{-1} sin\theta) = \sum_{i=1}^4 a_i \, exp(-b_i \lambda^{-2} sin^2\theta) + c \tag{2.40}$$

in which the parameters a_i, b_i and c have been determined by curve fitting procedures [137].

Small-angle X-rays scattering (SAXS) is a very accurate technique which allows to determine the micro- and nanoscale structure of systems as polymers, proteins, colloids, etc. It indeed accesses a distance range comprised between 5 and $25\,nm$ for macromolecules up to $125\,nm$ for partially ordered systems. *Wide-angle X-rays scattering* (WAXS) provides complementary information about the structure of crystalline, semi-crystalline and amorphous samples. In fact comparing with SAXS tecnique, the distance from the sample to the detector is shorter and diffraction maxima at larger angles are observed.

X-ray instrument

SAXS and WAXS diffraction experiments were performed at the Material Physics Center-Centro de Física de Materiales (CFM) in San Sebastián using a Rigaku SAXS S-MAX3000 equipment supplied with WAXS image plate chamber. The $MicroMax-002+$ X-ray Generator System is comprised of a microfocus sealed tube X-ray source module and an integrated X-ray

generator unit. Using $Cu\ K_\alpha$ transition photons of wavelength $\lambda = 1.54\text{Å}$ are provided. Using WAXS capabilities, an X-ray diffraction pattern in the Q-range from ≈ 0.7 up to 5Å^{-1} is accessed.

Broadband dielectric spectroscopy

Dielectric spectroscopy is a useful technique to study the dynamics of polymeric systems. It involves the interactions of electromagnetic waves with matter in a frequency range comprised between 10^{-6} and $10^{12}\ Hz$ [138]. Such extended range of frequency allows to study molecular and collective dipolar fluctuations, charge transport, polarization effects and to determine the dielectric properties of the material under investigation.

When an electric field is applied to the faces of a parallel capacitor containing a dielectric sample, the molecular and atomic charges are moved from their equilibrium position and the material is polarized. In polymeric systems the polarization due to the charge migration and that due to the ri-orientation of the permanent dipoles are the mainly studied phenomena. The first polarization mechanism gives rise to the conductivity and it is related to the viscosity, while the polarization of permanent dipoles involves motions of molecular segments and it is related to the macroscopic observable polarization. In a polymer the molecular dipole can be orientated parallel or perpendicular to the main chain or can have both components and the different motional processes are characterized by fluctuations of the polarization well separated in their relaxation times and length scales.

Most of dielectric measurements are conducted by applying voltage to the electrode interface and measuring the amplitude and the phase shift of the resulting current. The complex dielectric function of a capacitor filled with a sample and to which is applied a periodical electric field $E(t) = E_0 exp(-i\omega t)$ characterized by an angular frequency $\omega = 2\pi\nu$ is defined as

$$\epsilon^* = \epsilon'(\omega) - i\epsilon''(\omega) = \frac{C^*(\omega)}{C_0} \tag{2.41}$$

in which $\epsilon'(\omega)$ and $\epsilon''(\omega)$ are the real and the imaginary part of the complex dielectric function and C_0 is the vacuum capacitance. ϵ^* can be derived by measuring the complex impedance $Z^*(\omega)$

$$\epsilon^* = \frac{1}{i\omega\, Z^*(\omega)C_0} \tag{2.42}$$

The temperature and the angular frequency dependence of $\epsilon^*(\omega)$ originates from different motions which determine the specific features of $\epsilon'(\omega)$ and $\epsilon''(\omega)$. In the case of relaxation processes for example $\epsilon''(\omega)$ shows a peak, while $\epsilon'(\omega)$ a step-like decrease with increasing frequency. In contrast, conduction phenomena show an increase of $\epsilon''(\omega)$ with decreasing frequency. Therefore information on the dynamics of the sample can be obtained by analyzing $\epsilon^*(\omega)$. In general, the frequency ν_p of the maximum of the peak of $\epsilon''(\omega)$ represents the characteristic relaxation rate $\omega_p = 2\pi\nu_p$, which is related to the characteristic relaxation time $\tau_p = 1/\omega_p$ of the fluctuating dipole. From the shape of the loss peak the equivalent distribution of the relaxation times can be deduced.

Different model functions are usually used to analyze dielectric spectra [138]. The *Debye function* is given by

$$\epsilon^* = \epsilon_\infty + \frac{\Delta\epsilon}{1 + i\omega\tau_D} \tag{2.43}$$

where $\Delta\epsilon = \epsilon_S - \epsilon_\infty$ is the dielectric strength with $\epsilon_S = \lim_{\omega\tau\ll 1} \epsilon'(\omega)$ and $\epsilon_\infty = \lim_{\omega\tau\gg 1} \epsilon'(\omega)$. The Debye relaxation time τ_D is related to the position of the maximum of the loss peak, which is symmetric with half width ω_D of 1.14 decades [138].

If the shape of the loss peak is asymmetric and broader than that predicted by (2.43) the process is called non-Debye and different model function are used. The Cole-Cole function is defined as [139]

$$\epsilon^* = \epsilon_\infty + \frac{\Delta\epsilon}{1 + (i\omega\tau_{CC})^\beta} \tag{2.44}$$

where β is comprised in the range between 0 and 1 and leads to a symmetrical broadening. When $\beta = 1$ the Debye function is obtained.

For experiments performed on liquids or low-molecular glass forming materials, the asymmetric complex dielectric function can be described by the Cole-Davidson function [140, 141]

$$\epsilon^* = \epsilon_\infty + \frac{\Delta\epsilon}{1 + (i\omega\tau_{CD})^\gamma} \tag{2.45}$$

in which the parameter γ, defined in the range of $0 < \gamma \leq 1$, describes the asymmetric broadening of the relaxation function for frequencies $\omega > 1/\tau_{CD}$ with τ_{CD} the Cole-Davidson relaxation time. When $\gamma = 1$ the Debye funtion is obtained.

A more general function to describe the dielectric spectra in the frequency domain was proposed by Havriliak and Negami (HN) [142, 143]. It reads as

$$\epsilon^* = \epsilon_\infty + \frac{\Delta\epsilon}{(1 + (i\omega\tau_{HN})^\beta)^\gamma} \tag{2.46}$$

with $\beta > 0$ and $\beta\gamma \leq 1$.

In the time domain the non-Debye pattern is usually described by the empirical Kohlraush-Williams-Watts (KWW) function in the following way

$$\epsilon(t) - \epsilon_\infty = \Delta\epsilon\left[1 - exp\left(\left(-\frac{1}{\tau_w}\right)^{\beta_w}\right)\right] \tag{2.47}$$

A relation between the Cole-Davidson and the KWW functions was derived by Patterson and Lindsay [144] and then extended by Colmenero *et al* [145] leading to the following relations between KWW and HN relaxation times:

$$log\frac{\tau_{HN}}{\tau_w} \approx 2.6(1 - \beta_w)^{0.5}e^{(-3\beta_w)}$$

with

$$\beta\gamma \approx \beta_w^{1.23}$$

broadband dielectric spectroscopy instrument

All the dielectric measurements were performed at the Material Physics Center-Centro de Física de Materiales in San Sebastián (CFM). The complex dielectric function $\epsilon^*(\omega)$ was measured in the frequency range $10^{-2} - 10^6 \, Hz$ using the broadband dielectric spectrometer *Novocontrol Alpha-N*, while in the higher frequency range of $10^6 - 10^9 \, Hz$ an Agilent rf impedance analyzer $4192B$ was used.

CHAPTER 3

MOLECULAR DYNAMICS SIMULATION

3.1 Introduction to molecular dynamics simulations

The macroscopic properties of a system result from the behaviour of collections of individual atoms and molecules and computer simulation indeed provides a route from microscopic details to macroscopic properties of experimental interest. In scientific investigation, computer simulation plays a double role. It can be used to perform a *computer experiment*, that is test the validity of a theory contrasting simulated results against theoretical predictions. Or it can be used as a tool to get a better insight into the microscopic characteristic of a sample. This is found when simulated data are compared with experimental results to check if a model is adequate or not. Once this process has been carried out, the simulation can be further exploited [146–148].

Molecular dynamics simulation (MD) is a technique in which the behaviour of a set of molecules is computed solving the classical equation of motion, Newton's equations. The positions of the molecules are connected in time so MD are deterministic.

In general computer simulation yields information on microscopic level

61

and, with the aid of statistical mechanics, it is possible to convert this very detailed information into macroscopic terms [146]. In a system formed by N particles, the position $\mathbf{r}$ and the momenta $\mathbf{p}$ of each particle can be expressed by a set of coordinates in a $6N$ multidimensional space: the phase-space. If $\mathbf{\Gamma} = \mathbf{\Gamma}(\mathbf{r}, \mathbf{p})$ describes a point in such space, the istantaneous value of a property $\mathscr{A}$ of such system can be interpreted as $\mathscr{A}(\mathbf{\Gamma})$. As the system evolves, the phase point moves along a trajectory in the phase space. Therefore, the measured value of the observable macroscopic property $\mathscr{A}$ can be calculated as the time average over a long time interval t_{obs}

$$\mathscr{A}_{obs} = \frac{1}{t_{obs}} \int_{t_0}^{t_0+t_{obs}} \mathscr{A}(\mathbf{\Gamma}(t)) \, dt$$

For systems in thermodynamic equilibrium, the time average is independent of the time origin t_0 and really approximates the time average over an infinite time [147]. It thus results

$$\mathscr{A}_{obs} = < \mathscr{A} >_{time}$$

with

$$< \mathscr{A} >_{time} = < \mathscr{A}(\mathbf{\Gamma}(t)) >_{time} = \lim_{t_{obs} \to \infty} \frac{1}{t_{obs}} \int_0^{t_{obs}} \mathscr{A}(\mathbf{\Gamma}(t)) \, dt$$

In molecular dynamics simulation the equation of motion are solved step-by-step, over a long finite number τ_{obs} of time steps of length $\delta t = t_{obs}/\tau_{obs}$. The length of the time step δt is a compromise: it has to be large enough to produce reasonable time scales, but it has to be short enough to resolve important feature of the atoms at very small time scales.

The value of the simulated property $\mathscr{A}_{obs}^{sim}$ is calculated as

$$\mathscr{A}_{obs}^{sim} = \frac{1}{\tau_{obs}} \sum_{\tau=1}^{\tau_{obs}} \mathscr{A}(\mathbf{\Gamma}(\tau))$$

in which τ is an index running over the succession of time step.

For simulated systems in thermodynamic equilibrium it is assumed that the computed interval average, over which the equation on motion are solved, equates the time average $< \mathscr{A} >_{time}$ [147]. It means that

$$\mathscr{A}_{obs}^{sim} =< \mathscr{A} >_{time}$$

This assumption makes the issue of validation of a simulation of utmost importance in every scientific work: it is analogous to that of the accuracy in a laboratory experiment.

While in MD the time average is performed over an interval, in statistical mechanics the time average is avoided and it is replaced by an ensemble average invoking the *ergodic hypothesis*. This concept consists in that, over a sufficiently long time, a phase point $\mathbf{\Gamma}$ moves through all the possible configurations of the system. In such condition, the time average of a function $\mathscr{A}$ over a trajectory is equal to an ensemble average [147].

A molecular dynamics simulation consists of three basic steps: the first is the construction and equilibration of the model, the second the calculation of the atomic trajectories, that is really the simulation, and the third, the analysis of the trajectories. The paragraph 3.2 will concern the first and the second step, while, in the paragraph 3.3, the computation of the magnitudes of physical interest will be presented.

3.2   The atomistic model

Fully atomistic molecular dynamics simulation were carried out using the simulation package *Materials Studio* from *Accelrys* [149, 150]. The simulated system is created through a user-friendly graphical interface in which it is possible to establish the characteristic of the system, as the number of monomers in a polymer chain, the tacticity, etc. Once the system is generated, it is transferred to multi-processor Linux Clusters [151] in which *Discover* program, running standalone, performs the simulation [152].

The *Amorphous cell* algorithm

MD simulation is usually performed on a large number of atoms. To prevent surface effects affecting the simulation in bulk liquids, periodic boundary conditions are used. The system is confined in a cubic box of length L, the *primary cell*, which is replicated to form an infinite space. The replicated cells, called *image cells*, contain, placed in the same position as in the original one, the *image* of the atoms. As the simulation runs, the atoms in the primary cell start moving through the box and the image atoms perform the same movements: as an atom exits from the primary cell, its image enters through the opposite face. Only the coordinates of the atoms in the original cell are saved [146, 147].
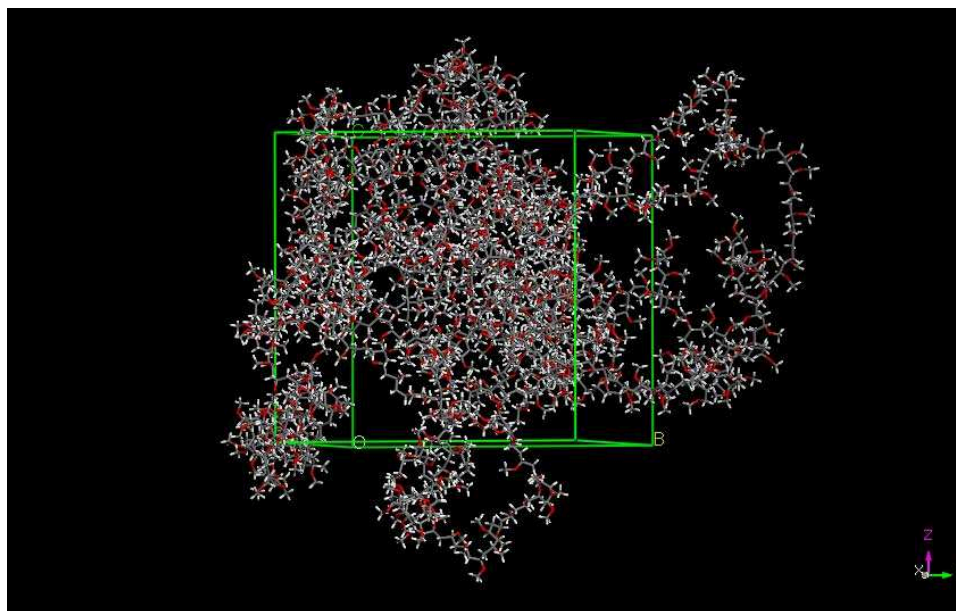
Figure 3.1: Example of the PVME simulated cell.

In Discover engine the primary cell is built using the *Amorphous cell algorithm* originally proposed by Theodorou and Suter [153]. An example

of a PVME simulated cell is represented in Fig. 3.1. Once the initial cell is built, a standard minimization procedure, the Polak-Ribiere conjugate gradient method, is performed to equilibrate the system. Furthermore, before changing to constant-volume ensemble in which data are collected, in the equilibration procedure short *NPT* runs (constant number of atoms N at constant pression P and temperature T) are performed. The NPT ensemble works varing the length, and so the volume of the cell. In the *NVT ensemble* the number of atoms, the temperature and the length of the cubic cell is maintained constant. In this conditions data are collected and the atom trajectories are computed.

The *COMPASS* force field

The *force field* approach works at atomic level by neglecting the electron-electron and the electron-nucleus interactions. The treatment of the electronic degrees of freedom is so incorporated in empirical potentials for the bond lengths, the bond angles, the torsion angles and the nonbonded interactions between atoms of different molecules. The force field parameters are calculated from quantum chemistry, quantum mechanics ab initio data or high-quality experimental data. The force field functional form mimics the interatomic interactions through different contributions related to the corresponding effective potentials [21, 154].

The *COMPASS* force field, *condensed-phase optimized molecular potentials for atomistic simulation studies*, belongs to the class of force field especially designed to simulate polymers and organic materials: the *CFF family* of force field. The parametrization of the COMPASS has been built up following an hybrid method, consisting of an ab initio parametrization and empirical optimization. In the first step, the partial charge and the valence terms have been obtained by fitting ab initio potential energy surfaces. Then, empirical data were used to optimize the force field [154, 155]. So COMPASS is a type of ab initio forcefield in that it is derived from extensive *ab initio* data. It

makes possible to simulate, with good accuracy, gas-phase and condensed phase properties for a broad range of polymers and molecules [154–157].

All CFF family of force field have the following functional form [150]:

$$
\begin{aligned}
E_{pot} =& \sum_{b} \left[\, K_2(b - b_0)^2 + K_3(b - b_0)^3 + K_4(b - b_0)^4 \right] + \\
&+ \sum_{\theta} \left[\, H_2(\theta - \theta_0)^2 + H_3(\theta - \theta_0)^3 + H_4(\theta - \theta_0)^4 \right] + \\
&+ \sum_{\phi} \left[V_1\left[1 - \cos(\phi - \phi_1^0)\right] + V_2\left[1 - \cos(2\phi - \phi_2^0)\right] + V_3\left[1 - \cos(3\phi - \phi_3^0)\right] \right] + \\
&+ \sum_{\chi} k_{\chi}\chi^2 + \sum_{b}\sum_{b'} F_{bb'}(b - b_0)(b' - b_0') + \sum_{\theta}\sum_{\theta'} F_{\theta\theta'}(\theta - \theta_0)(\theta' - \theta_0') + \\
&+ \sum_{b}\sum_{\theta} F_{b\theta}(b - b_0)(\theta - \theta_0) + \sum_{b}\sum_{\phi} (b - b_0)[V_1 \cos\phi + V_2 \cos 2\phi + V_3 \cos 3\phi] + \\
&+ \sum_{b'}\sum_{\phi} (b' - b_0')[V_1 \cos\phi + V_2 \cos 2\phi + V_3 \cos 3\phi] + \\
&+ \sum_{\theta}\sum_{\phi} (\theta - \theta_0)[V_1 \cos\phi + V_2 \cos 2\phi + V_3 \cos 3\phi] + \\
&+ \sum_{\theta}\sum_{\theta'}\sum_{\phi} K_{\theta\theta'\phi}(\theta - \theta_0)(\theta' - \theta_0') \cos\phi + \\
&+ \sum_{i>j} \frac{q_i q_j}{\varepsilon\, r_{ij}} + \sum_{i>j} \left[\frac{A_{ij}}{r_{ij}^9} - \frac{B_{ij}}{r_{ij}^6} \right]
\end{aligned}
$$

(3.1)

Two main classes of terms can be distinguished: the valence terms and the nonbond interaction terms [154]. The valence terms, including diagonal and off-diagonal cross-coupling terms, represent internal coordinates of bond b, angle θ, torsion angle ϕ and out-of-plane angle χ. The nonbond interactions include a Lennard-Jonnes 9-6 function for the van der Waals term and a Coulombic function for the electrostatic interaction. The nonbond terms operate for atoms separated by two or more intervening atoms or for those belonging to different molecules.

The *velocity Verlet* algorithm

A standard method to solve the differential equations in MD is the *finite difference* approach. Given the initial coordinates, the velocities and other dynamic information at time t, the positions, velocities, etc. at $t + \delta t$ are calculated step-by-step. Depending on the investigated system, different values of δt and different algorithms can be used to calculate the new trajectories.

The *velocity Verlet* algorithm is the algorithm used by Discover engine [158]. It is the modern formulation of the *Verlet* algorithm and it stores positions, velocities and accelerations all at the same time t. It reads as follow [146, 159]:

$$\mathbf{r}(t + \delta t) = \mathbf{r}(t) + \delta t \mathbf{v}(t) + \frac{1}{2} \delta t^2 \mathbf{a}(t) \tag{3.2}$$

$$\mathbf{v}(t + \delta t) = \mathbf{v}(t) + \frac{1}{2} \delta t [\mathbf{a}(t) + \mathbf{a}(t + \delta t)] \tag{3.3}$$

This approach resembles that of the *predictor-corrector* algorithm in which the predicted trajectories at time $t + \delta t$ are obtained through a Taylor expansion about time t. From the predicted position, the corrected forces at time $t + \delta t$, and hence the corrected acceleration, are then calculated. Comparing these with the predicted accelerations, the error is estimated and it can be used to gain a better approximations of the true positions, velocities, etc. This procedure can be iterated.

In MD it is of utmost importance to choose a good value of the integration time step δt and the evaluation of the forces is the most time-consuming part of the simulation.

3.3 Analysis of the MD trajectories

Once the simulation has been carried out, the computed MD trajectories can be analysed to evaluate the structural and dynamical properties of the system under investigation. The *Van Hove correlation functions* provide

a tool to carry out this task. The Fourier transformation of these functions indeed allow the computation of physical magnitudes which can be compared to experimental results.

In the following sections, α and β refer to different species of atoms, which can be distinct atoms, different isotopes or different types of the same atoms, as for example carbons C_{mc} belonging to the main chain of a polymer, and carbon C_{mg} belonging to the methyl group. The index i usually refers to particles of type α and j to particles of type β.

For homogeneous uniform substances $G(\mathbf{r}, t)$, already introduced in the paragraph 2.1.4 (Eq. (2.30)), depends only on the scalar distance r. For the different species of atoms α and β it can be written as

$$G_{\alpha\beta}(r,t) = \frac{1}{4\pi\, r^2}\frac{1}{N_\alpha N_\beta}\Big\langle \sum_{i_\alpha}^{N_\alpha}\sum_{j_\beta}^{N_\beta}\delta[r-|\mathbf{r}_{i_\alpha}(0)-\mathbf{r}_{j_\beta}(t)|\,]\Big\rangle \qquad (3.4)$$

in which N_α and N_β are the total number of particles α and β.

To extract the values of $G_{\alpha\beta}(r,t)$ from the MD trajectories, a working expression is needed [147, 148]. Fixing k as the index running over the total M time origins over which the trajectories are collected, the distance between atom i, read at time t_k, and j, read at time $t+t_k$, is direct to compute. Then, averaging over all the distances and the frames, an histogram with bin width Δr can be constructed. The working expression thus results

$$G_{\alpha\beta}(r,t) = \frac{1}{M}\frac{1}{N_\alpha N_\beta}\frac{1}{4\pi\, r^2\Delta r}\sum_{k}^{M}\sum_{i_\alpha}^{N_\alpha}\sum_{j_\beta>i_\alpha}^{N_\beta}\delta[r-|\mathbf{r}_{i_\alpha}(t_k)-\mathbf{r}_{j_\beta}(t+t_k)|\,]\Delta r$$

In the case of the single particle motion, the self Van Hove correlation function, also introduced in the paragraph 2.1.4, can be expressed as

$$G_s(r,t) = G_\alpha(r,t) = \frac{1}{4\pi\, r^2}\frac{1}{N_\alpha}\Big\langle \sum_{i_\alpha}^{N_\alpha}\delta[r-|\mathbf{r}_{i_\alpha}(0)-\mathbf{r}_{i_\alpha}(t)|\,]\Big\rangle \qquad (3.5)$$

and the working expression is thus

$$G_\alpha(r,t) = \frac{1}{M}\frac{1}{N_\alpha}\frac{1}{4\pi\, r^2 \Delta r} \sum_k^M \sum_{i_\alpha}^{N_\alpha} \delta[r - |\mathbf{r}_{i_\alpha}(t_k) - \mathbf{r}_{i_\alpha}(t + t_k)|\,]\Delta r$$

3.3.1 Structural properties

Once the pair correlation function $G_{\alpha\beta}(r, t = 0)$ is calculated, the static structure factor, as measured by a neutron scattering or X-ray experiment, is straighforward to compute. It is the sum over all the Fourier transformed pair correlation functions properly weighted with the coherent scattering lengths or the atomic form factors of the involved species of atoms. In the case of X-ray experiments, the working expression can be written as

$$S(q) = N \sum_{\alpha\beta} f_\alpha(q) f_\beta(q) S_{\alpha\beta}(q) \tag{3.6}$$

in which

$$S_{\alpha\beta}(q) = x_\alpha \delta_{\alpha\beta} + \rho\, x_\alpha x_\beta \tilde{h}_{\alpha\beta}(q) \tag{3.7}$$

with $x_\alpha = N_\alpha/N_{tot}$, $x_\beta = N_\beta/N_{tot}$, $\rho = N_{tot}/V$ the number density and $\tilde{h}_{\alpha\beta}(q)$ is the Fourier transform of $g_{\alpha\beta}(r) - 1$ with $g_{\alpha\beta}(r) = G_{\alpha\beta}(r)/\rho$. In the expression (3.6) the atomic form factors are usually calculated using the approximation written in Eq. (2.40) with the values of the parameter listed in the table published in Ref.[137].

When there are no correlation $S_{\alpha\beta}(q) = x_\alpha \delta_{\alpha\beta}$ and the scattered intensity becomes

$$S_0(q) = \sum_\alpha x_\alpha f_\alpha(q) \equiv N\overline{f^2(q)} \tag{3.8}$$

Therefore, the measured structure factor results

$$S^M(q) = \frac{S(q)}{S_0(q)} = \frac{1}{\overline{f^2(q)}} \sum_{\alpha,\beta} f_\alpha(q) f_\beta(q) S_{\alpha\beta}(q) \tag{3.9}$$

This is the quantity which has been computed and compared with the experimental results.

The funtions $S_{\alpha\beta}(q)$ are usually called *partial static structure factors*, because they are the Fourier transform of the pair correlation functions. The study of the behaviour of such functions is important to discerning the different contributions to the total static structure factor and to eventually revealing the local organization of distinct atoms or group of atoms in the sample [160–162].

3.3.2 Dynamical properties

In the case of a neutron scattering experiment performed on a protonated sample, the self intermediate scattering function $S_s(Q,t)$ turns out information on the hydrogen motion. The Fourier transform of the self Van Hove correlation function $G_s(r,t)$, weighted for the incoherent scattering lengths of the atoms forming the sample, results

$$S_s(Q,t) = S_{inc}^{\alpha}(Q,t) = \sum_{\alpha}(b_{inc}^{\alpha})^2 \int_0^{\infty} 4\pi\, r^2 G_{\alpha}(r,t)\frac{sin\, Qr}{Qr}dr \qquad (3.10)$$

So, in the case of a protonated sample, b_{inc}^H dominates the scattering length values of all the atoms in the system and it results

$$S_{inc}^{\alpha}(Q,t) \approx S_{inc}^H(Q,t)$$

The *mean squared displacements* (MSD) can be calculated as the second moment of the $G_s(r,t)$

$$< r^2(t) >= \int_0^{\infty} r^2\, G_s(r,t)4\pi r^2\, dr \qquad (3.11)$$

In some cases, such as free nuclei in a gas, harmonic crystal, simple diffusion at long times, $G_s(r,t)$ assumes a Gaussian form [119]

$$G_s^{gauss}(r,t) = [2\pi\sigma^2(t)]^{-3/2}exp\left[\frac{-r^2}{2\sigma^2(t)}\right] \qquad (3.12)$$

and the intermediate scattering function can be directly determined by the mean squared displacements $< r^2(t) >$

$$S_s^{gauss}(Q,t) = exp\left[- \frac{< r^2(t) >}{6} Q^2 \right] \tag{3.13}$$

A Gaussian correlation function implies a dependence on Q of the characteristic relaxation times τ_w evaluated by means of a KWW description as [163, 164]

$$\tau_w(Q) \propto Q^{-2/\beta} \tag{3.14}$$

In general, deviations from a Gaussian behaviour of the self Van Hove correlation function are expected. By expressing the $S_s(Q,t)$ in terms of its expansion in Q^2

$$S_s(Q,t) = exp\left[- \frac{< r^2(t) >}{6} Q^2 + \frac{\alpha_2(t) < r^2(t) >^2}{72} Q^4 + ... \right] \tag{3.15}$$

it is possible to define a parameter, $\alpha_2(t)$, which takes into account these deviations [165]. $\alpha_2(t)$ is called *non-Gaussian parameter*, its expression is

$$\alpha_2(t) = \frac{3}{5} \frac{< r^4(t) >}{< r^2(t) >^2} - 1 \tag{3.16}$$

and, in the Gaussian case, $\alpha_2(t) = 0$.

Dynamic structure factor

The dynamic structur factor gives the time dependence correlations among all the different particles in the sample. As for the static case, it is possible to semplify the calculation of such function defining the Fourier transform of the Van Hove correlation function as

$$a_{\alpha\beta}(Q,t) = \frac{N_\alpha N_\beta}{N_{tot}} \frac{1}{V} \frac{4\pi}{Q} \int_0^\infty dr\, r\, sin(Qr)[G_{\alpha\beta}(r,t) - 1]$$

and adding up all the contributions, weighted for the corresponding coherent scattering lengths. So the working expression results

$$S(Q,t) = \sum_{\alpha\beta} b^{\alpha}_{coh} b^{\beta}_{coh} \, a_{\alpha\beta}(Q,t) \tag{3.17}$$

3.3.3 Direct calculation of the scattering function

Knowing the atomic coordinates, the computation of the MSD can be performed in a direct way, without the calculation of the self Van Hove correlation function. The different working expression is

$$< r^2(t) >= \frac{1}{M}\frac{1}{N_\alpha} \sum_{k}^{M} |\mathbf{r}_\alpha(t+t_k) - \mathbf{r}_\alpha(t)|^2$$

and the calculation of $< r^4(t) >$, and so of the $\alpha_2(t)$, is straightforward.

The self intermediate scattering function and the dynamic structure factor can be also calculated avoiding the computation of Fourier transformation of the real space correlation functions. The relative working expressions are

$$S_s(Q,t) = \ S_\alpha(Q,t) = \ \frac{1}{M}\frac{1}{N_\alpha} \sum_{k}^{M} \sum_{i_\alpha}^{N_\alpha} e^{i\,[\mathbf{Q}\,(\mathbf{r}_{i_\alpha}(t)-\mathbf{r}_{i_\alpha}(0))]}$$

and

$$S_{\alpha\beta}(Q,t) = \ \frac{1}{M}\frac{N_\alpha N_\beta}{N_{tot}} \sum_{k}^{M} \sum_{i_\alpha}^{N_\alpha} \sum_{j_\beta}^{N_\beta} e^{i\,[\mathbf{Q}\,(\mathbf{r}_{j_\beta}(t)-\mathbf{r}_{i_\alpha}(0))]}$$

The allowed Q vectors depend on the dimension of the simulated cell L and are defined as $\mathbf{Q} = \frac{2\pi}{(L/2)} \cdot (h,k,l)$ with h, k, l integer number. The statistic increases at high Q values, because more vectors, given by the combination of h, k, l, can access to the same module of $\mathbf{Q}$. On the contrary, at low Q values, the statistic is poor.

CHAPTER 4

DRY PVME

4.1 Experimental and simulation details

4.1.1 Sample

Poly(vinyl methyl ether) (PVME) in aqueous solution with water content of $c_w = 50\%$ in weight and an average molecular weight of $M_w = 21.9\,Kg/mol$ was purchased by Sigma-Aldrich. The sample used for NS, broadband dielectric spectroscopy and X-ray measurements was carefully dried out and then stored at room temperature in a vacuum oven. The glass transition temperature, measured by means of differential scanning calorimeter, is found to be $T_g = 247 \pm 0.5\,K$, in agreement with literature data [166]. For all the neutron scattering experiments flat sample holders of thickness $0.2\,mm$ were used. An empty can and a vanadium sample (a purely elastic scatterer) were measured to define the background and to correct for detector efficiency respectively. The measured spectra were corrected, normalized, grouped and trasformed into energy transfer spectra by using the standard ILL and PSI data reduction programs. Correction for multiple scattering was estimated to be negligible because the trasmission of the samples was about 90%.

4.1.2   Experimental conditions

The **Time-of-Flight spectrometer FOCUS** was used with an incident wavelength of $\lambda = 5\text{Å}$ leading to a resolution of $\delta E(HWHM) \approx 45\mu eV$. In this chapter the attention is focused on the measurement performed at $400\,K$, but also the temperature of $100\,K$ was investigated and it has been used to study the effect of water on the PVME dynamics in the wet sample (next chapter). The resolution was determined from a measurement on the sample at $20\,K$ where the scattering is predominantly elastic. The measuring time was 5 hours. The effective Q-region investigated spans from 0.62 to $2.21\,\text{Å}^{-1}$.

The **backscattering spectrometer IN16** was set up with the wavelength $\lambda = 6.271\,\text{Å}$ and the energy resolution $\delta E(FWHM) \approx 0.4\mu eV$. The applied Doppler frequency allow to perform the measurements in the energy window comprised between $-15\mu eV \leq \hbar\omega \leq 15\mu eV$. The investigated Q range was between 0.19 and $1.9\,\text{Å}^{-1}$. The temperatures investigated were 325, 350 and $400\,K$ and the measuring time was of about 8 hours. The resolution function was determined from the measurement of a sample at $2\,K$.

The **Neutron Spin Echo spectrometer IN11** was set up according with the option $IN11C$, with an incident wavelength of $\lambda = 5.5\text{Å}$ and the multidetector placed at $25°$ scattering angle θ for its central detector. The time range explored was comprised between $5.3\,ps$ and $0.95\,ns$ and the Q-range between 0.25 and $0.72\,\text{Å}^{-1}$. The measurements were performed at 375 and $400\,K$ using measuring times of 2.5 hours. The instrumental resolution function was determined from the measurement of a sample at $10\,K$.

The **broadband dielectric spectroscopy** measurements were carried out in the frequency spectrum range of $10^{-2} - 10^6\,Hz$ with the isothermal frequency scans performed every 5 degrees over the temperature range of $120 - 250\,K$. The sample temperature was controlled with a stability better than $\pm 0.1\,K$. Parallel gold plated electrodes with a diameter of $20\,mm$ ($10\,mm$ for the high frequency range) were utilized. The sample thickness

was $0.1\,mm$.

The **X-ray** experiments were performed at room temperature ($\approx 300\,K$) and the measuring time was of 15 minutes. The spectra were corrected and analyzed using the SAXSGUI software. The sample was also measured by other members of the group at the $ID02$ beamline at ESRF at the temperatures of 253, 303 and $373\,K$. The diffraction patterns were corrected and analyzed using the ESRF data reduction programs.

4.1.3 Simulation details

The initial configuration was constructed through the Materials Studio environment using the amorphous cell builder under periodic boundary conditions [153]. The initial cubic cell was formed by 7 PVME chains of 100 monomers (7014 atoms) at $400\,K$. Standard minimization procedure as the Polak-Ribière conjugate gradients method was applied to minimize the obtained energy structure. By means of NPT (constant number of atoms, pressure and temperature) runs performed at atmospheric pressure [150] using the Berendsen pressure control method, a value of density $\rho = 0.981\,g/cm^3$ was achieved. This value is in excellent agreement with literature data (see the Ref. [167] and the table 4.1). An NVT (constant number of atoms, volume and temperature) dynamic run of $1\,ns$ was carried out without recording the atomic trajectories to further equilibrate the cell. The obtained structure was used as a starting point to collect data every $0.01\,ps$ during a simulation run of $1\,ns$. Afterwards, successive runs of $20\,ns$ collecting data every $0.5\,ps$ were carried out. Finally, an extra run of $1\,ns$ was performed to check the possible appearence of aging processes. The velocity-Verlet algorithm with a time step of $1\,fs$ was used as the integration method. To control the temperature, a velocity scaling procedure with a wide temperature window of $10\,K$ was followed. Under these conditions, in fact, greater temperature fluctuations are allowed but the trajectory is disturbed less. It has been checked that, by following this simple protocol, the results are similar to those obtained with

T(K)	$\rho_{exp}(g/cm^3)$	$\rho_{NVT}(g/cm^3)$
400	0.982	0.981
375	0.999	0.996
350	1.017	1.015
325	1.035	1.033
300	1.053	1.046

Figure 4.1: PVME simulated cell details: temperature, experimental and simulated density.

an NVE (constant number of atoms, volume and energy) ensemble, which has the proper Newton dynamics [168].

The initial cell built at $400\,K$ was used to yield simulated systems at the lower temperatures of 375, 350, 325 and $300\,K$. The new cells were obtained scaling the temperature and performing NPT dynamic runs to make the system arrange itself to the new thermodynamic conditions. Each cell was equilibrated following the same protocol of the starting one. Once the equilibrium density was reached, in order to carry out a $40\,ns$ NVT dynamic run, the same procedure of the first simulated sample was followed. The experimental and simulated densities of the equilibrated cells are resumed in the table 4.1. The total CPU time used to simulate each temperature with 10 processors running in parallel was about 3 months.

4.2 Experimental results and data analysis

4.2.1 PVME Structure

In Fig. 4.2 the X-ray static structure factor as measured at room temperature (RT) by WAXS at the CFM laboratory is represented and in the insert the diffraction patterns obtained at the ESRF at different temperatures are shown. The results are in agreement with the literature [169]. The patterns at the common temperature (room temperature for the CFM experiment and
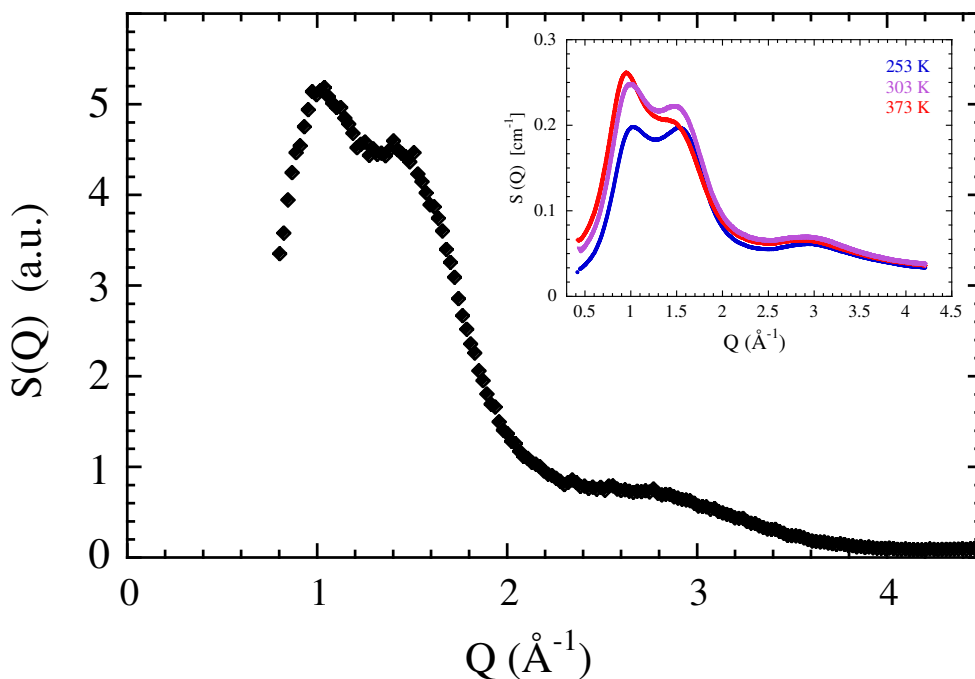
Figure 4.2: X-ray static structure factor of dry PVME obtained from WAXS measurements performed at the CFM at $\approx 300\,K$. In the insert the ESRF diffrection patterns of dry PVME at the indicated temperatures are represented.

$303\,K$ for the ESRF experiment) coincide very well, allowing a factor that matches the intensities, since the imaging plate does not allow a measurement in absolute units. In the diffraction patterns three peaks can be observed, two are found in the region comprised between ≈ 0.5 and $\approx 1.5\,\text{\AA}^{-1}$, while the third and very broad peak is placed at $\approx 2.7\,\text{\AA}^{-1}$. The first two peaks are placed at the Q-values of $Q_{1MAX} \approx 0.9\,\text{\AA}^{-1}$ and $Q_{2MAX} \approx 1.5\,\text{\AA}^{-1}$. In the Bragg approximation the positions of the peaks correspond to distances of the order of $d_1 \approx 2\pi/Q_{1MAX} \approx 6.98\,\text{\AA}$ and $d_2 \approx 4.19\,\text{\AA}$. The effect of the temperature can be observed in the insert. Increasing the temperature the intensity of the first peak increases and the position of the maximum shifts toward lower Q-values. The second peak also follow this tendency, but at the highest studied temperature its intensity is notably lowered.

4.2.2   PVME Dynamics: hydrogen self-motion

NS results

All the neutron scattering experiments were performed on protonated PVME samples and, due to the high value of the hydrogen incoherent cross section (see table 2.6), the scattered intensity can be approximated to the incoherent scattering contribution derived from hydrogen atoms: $S(Q,\omega) \approx S_{inc}^H(Q,\omega)$. All the experiments were carried out well above the glass transition temperature in which the main dynamical process is the α-relaxation. However, localized motions as methyl group rotations also occur.

Fig. 4.3 shows FOCUS results at $400\,K$. Part (a) shows the spectra in the frequency domain at several Q investigated. As it can be observed on increasing Q the scattered intensity decreases and the peak broadens suggesting a diffusive-like motion of the hydrogens. The spectra were analyzed following a deconvolution procedure [170], by which the intermediate scattering function is calculated by dividing the Fourier transformed experimental spectra by that of the reference measurement corresponding to a purely elastic signal. In Fig. 4.3 (b) such deconvoluted intermediate scattering functions are shown for different Q-values and two dynamic regimes can be distinguished. This feature will be discussed in the successive section concerning the data analysis.

FOCUS accesses Fourier times shorter than some tens of ps. Since the α-relaxation slows down with decreasing temperature, this instrument cannot accurately determine anymore its characteristic time. Therefore, BS or NSE techniques are needed to resolve characteristic relaxation times in the range of the nanosecond.

Fig. 4.4 shows, in a logarithmic representation, normalized BS spectra at 325, 350 and $400\,K$ at different Q-values. The broadening of a spectrum in the quasielastic region is related to the inverse of the characteristic
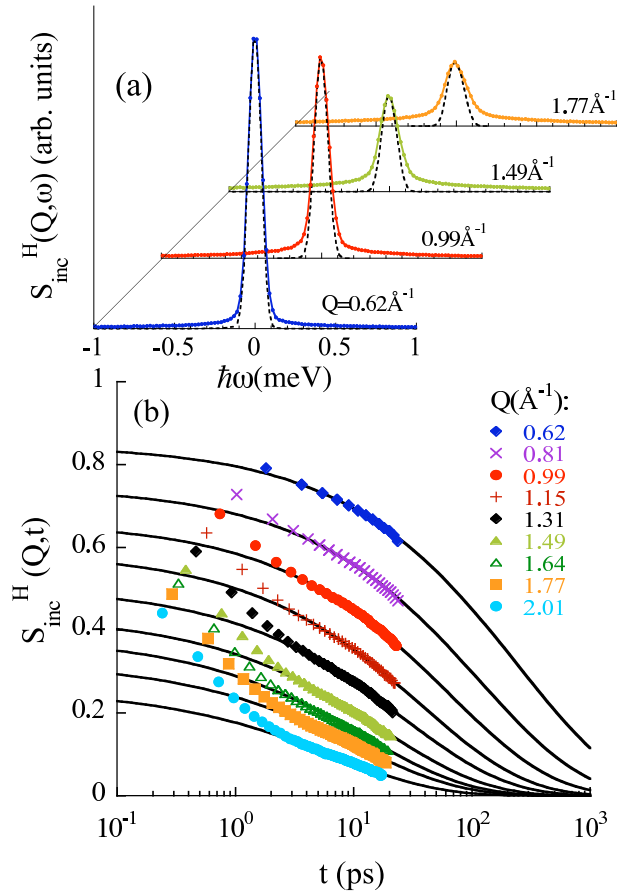
Figure 4.3: (a) FOCUS spectra at $400\,K$ at the indicated Q-values. The dashed lines represents the resolution function. (b) Fourier transformed data deconvoluted with the instrumental resolution. The solid lines are the KWW fits of the data for $t \geq 2\,ps$.

time of the proton motion: the broader is the spectrum, the faster is the motion. Moreover, for a given temperature, the spectrum broadens as the Q-value increases, showing again that the hydrogen dynamics corresponds to a diffusive-like motion.

As it has been introduced in the paragraph 2.1.7, NSE is an experimental technique which directly accesses the time domain. The normalized function presented in (2.38) depends on the coherent and incoherent scattering function weighted for the corresponding cross section. In protonated PVME
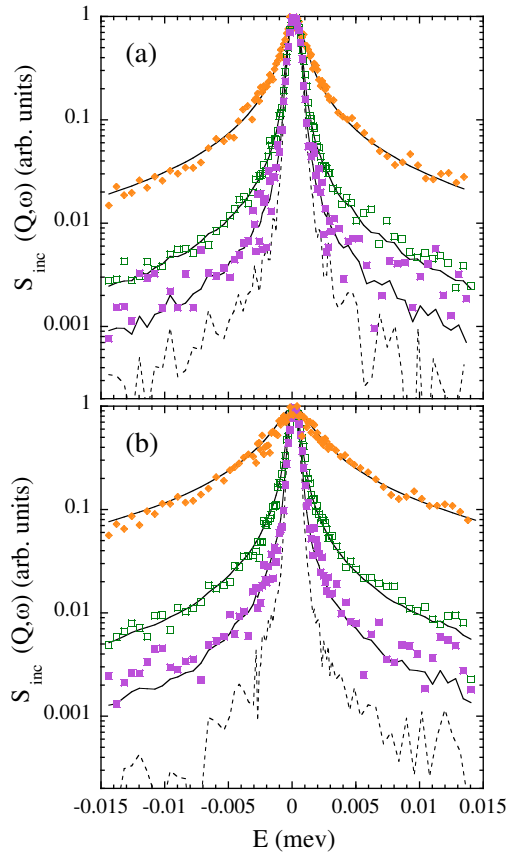
Figure 4.4: IN16 spectra at the temperature of 325 (full squares), 350 (empty squares) and 400 K (diamonds) at the different Q-values of (a) 0.652 and (b) 1.062Å^{-1}. All the spectra are normalized to their maximum intensities, solid lines represent the fitting curves and the dashed lines the instrumental resolution.

sample, the incoherent component is strong enough to dominate the NSE signal, so

$$S_{NSE}(Q,t) \approx S_{inc}^{H}(Q,t)$$

Fig. 4.5 shows some representative examples of the curves obtained by NSE and corrected according to the following procedure.

The data collected at high temperatures clearly decay to 0 in the experimental window, evidencing the absence of an elastic component and thereby the diffusive-like character of the motions addressed. This is also supported
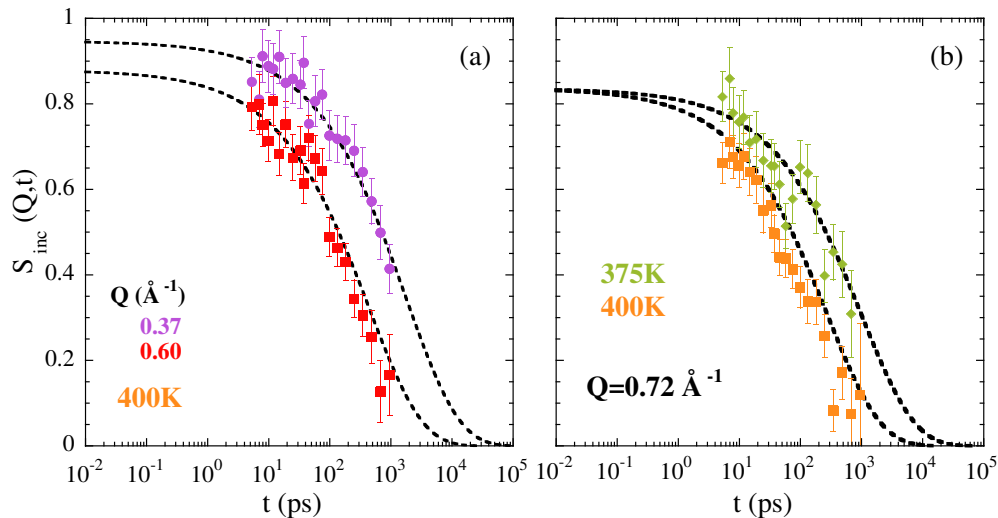
Figure 4.5: (a) NSE data at the fixed temperature of $400\,K$ and at the different values of $Q = 0.37\text{Å}^{-1}$ (circles) and $Q = 0.6\text{Å}^{-1}$ (squares). (b) NSE data at fixed $Q = 0.72\text{Å}^{-1}$ and at the different temperatures of $375\,K$ (diamonds) and $400\,K$ (squares). In both figures the dotted lines are the KWW fitting curves.

by the Q-dependent decay of the function directly observed in the time domain.

As a result of the polarization analysis after the scattering process, a NSE spectrometer offers only a limited band-pass to the scattered neutrons [132]. Inelastically scattered neutrons with energy higher than that allowed by the band-pass ($\approx 2meV$) are not transmitted through the instrument and do not participate to the normalization. The difference between the measured and the normalized signal corresponds to a factor

$$A_{BP}(Q) = \int_{BP} d\omega\, S(Q,\omega)$$

The simulation results can be used to correct the NSE data [171, 172]. In fact, the factor $A_{BP}(Q)$ can be effectively related to the simulated intermediate scattering function computed for all the hydrogens of the system at an *effective band-pass time* t_{BP}

$$A_{BP}(Q) = S_{MD}^{H}(Q, t = t_{BP})$$

Such relation has been used to correct the measured signal. The band-pass time estimated for this case is found to be $t_{BP} = 0.2 ps$.

NS data analysis

Since methyl groups participate simultaneously in the α-relaxation and in faster and localized motions, to analyse the data some considerations have to be done.

FOCUS deconvoluted intermediate scattering function at $400\,K$, shown in Fig. 4.3(b), exhibits two regimes. For $t \lesssim 2ps$ the correlation functions decay to a value which depends on Q and T. This first regime is related to the fast dynamics. At such short times and in the temperature range investigated, the PVME methyl group dynamics is also expected to contribute [173]. In the second long-time regime ($t \gtrsim 2\,ps$), the decay of the incoherent scattering function is characterized by a time scale that strongly depends on Q and T and relates mainly to the structural relaxation. As it has been previously commented, the structural relaxation in glass-forming systems shows a nonexponential behaviour usually described by means of the KWW function (Eq. (1.3)). Therefore, in the time regime of $t \gtrsim 2\,ps$, the intermediate scattering function has been modeled as

$$S_{inc}^{H}(Q,t) = A(Q,T)\,exp\Big(- \Big(\frac{t}{\tau_w(Q,T)}\Big)^{\beta}\Big) \tag{4.1}$$

Here the effect of the fast dynamics, which leads to a decay of the amplitude, is parametrized by the prefactor $A(Q,T)$ and β is the shape parameter reflecting the deviations from exponential behaviour. β takes values between 0 and 1 and for glass forming polymers it is usually 0.5 [8]. $\tau_w(Q,T)$ is the characteristic time of the structural relaxation.

In a preliminary analysis it has been observed that the β value was ≈ 0.5, so its value was fixed to 0.5. In figure 4.3 (b) the KWW fitting curves of the long-time regime are shown through solid lines. It can be seen that the fits are excellent. This finding supports the hypothesis that the methyl group

rotations are fast enough to lead to the corresponding decay of the incoherent structure factor at times shorter than $2\,ps$, i. e. in the fast regime. Therefore, their influence in the spectra is contained in the prefactor $A(Q,T)$, at least at this high temperature. The characteristic relaxation times obtained for the α-relaxation are shown in Fig.4.6 as full triangles. They decrease with increasing Q-value, which is a signature of a diffusive-like motion.

$IN16$ data were analyzed in the frequency domain. If the structural relaxation and the localized motions can be considered as statistically independent, as it has been found in MD simulations performed on polyisoprene [174], the total scattering function results to be given by the convolution of the corresponding ones [168]. Assuming the same LMF for all the protons in the sample and separating the contribution to the total scattering function of the main chain hydrogens (cH) from that of the methyl group hydrogens (mgH), the total scattering function is approximated to

$$S_{inc}^{H}(Q,\omega) = LMF\left[n_{cH}\,S_{inc}^{KWW}(Q,\omega) + n_{mgH}\,S_{inc}^{rot}(Q,\omega) \otimes S_{inc}^{KWW}(Q,\omega)\right]$$

(4.2)

in which n_{cH} and n_{mgH} are the fractions of the different species of hydrogens with respect to the total. $S_{inc}^{rot}(Q,\omega)$ corresponds to the methyl group rotational motion. It contains an elastic and a quasielastic contribution and it can be written as

$$S_{inc}^{rot}(Q,\omega) = EISF\,\delta(\omega) + (1 - EISF)\varphi^{rot}(Q,\omega)$$

(4.3)

The *elastic incoherent scattering function* EISF carries the information about the geometry of the involved motion and for the methyl group rotation it reads as

$$EISF = \frac{1}{3}\left(1 + 2\frac{sin(Q\,r_{HH})}{Q\,r_{HH}}\right)$$

(4.4)

with $r_{HH} = 1.78\text{Å}$ being the distance between methyl group hydrogens.

In the quasielastic contribution, $\varphi^{rot}(Q,\omega)$ provides the dynamic dependence and in an amorphous system, due to the disorder inherent in it, $\varphi^{rot}(Q,\omega)$ is usually described by a distribution of Lorentzian functions [173, 175, 176]. In the temperature range investigated the rotation of the methyl group is so fast that it is expected to be out of the $IN16$ window [173]. Therefore $\varphi^{rot}(Q,\omega)$ results extremely broad and its contribution can be well approximated by an effectively negligible flat background. The scattering function has been thus analysed by means of the Fourier transform of the KWW function

$$S_{inc}^{H}(Q,\omega) = \mathcal{F}\left\{A(Q,T)\,exp\left[-\left(\frac{t}{\tau_w(Q,T)}\right)^{\beta}\right]\right\}$$

The prefactor $A(Q,T)$ takes into account the fast dynamics, including the methyl group contribution: $A(Q,T) = LMF(n_{cH} + n_{mgH}EISF)$.

In the data analysis, β was first considered as a free parameter and its value was found to fluctuate around 0.5, so it was fixed to $\beta = 0.5$. In Figure 4.4, besides the instrumental resolution, the fitting curves are also represented. They describe in an excellent way the data confirming the hypothesis that the methyl group rotation is so fast that, at these temperatures, it cannot be detected by $IN16$ spectrometer. Finally, the characteristic relaxation times have been evaluated and they are shown in Figure 4.6 as full squares.

As it is shown in Figure 4.5, the longer Fourier times accessed by NSE spectrometer cover almost entirely the decay of the correlation function allowing to univocally determine the characteristic timescales. The KWW function was used to analysed the data. As in the previous procedures, the behaviour of the β parameter was studied first and then it was fixed to the value of $\beta = 0.5$, being $\beta \approx 0.5$. The fits, depicted as dashed lines in the figure, are excellent. The characteristic relaxation times were finally estimated and they are represented in Fig.4.6 as full circles.

The good agreement among the results obtained with different neutron scattering techniques and evidenced in Fig. 4.6 supports the consistency of the protocol followed in the data analysis.
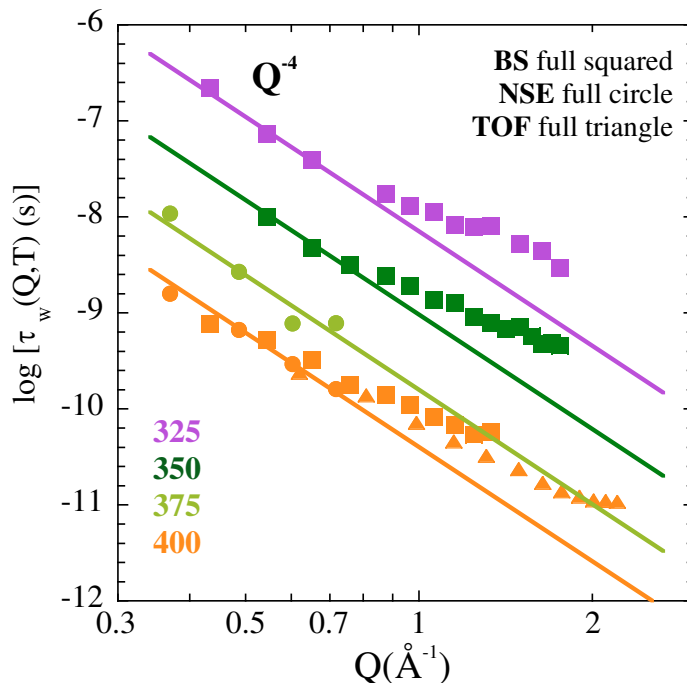
Figure 4.6: Q-dependence of the characteristic relaxation times estimated from the KWW analysis of the indicated NS data. Solid lines represent a Q^{-4}-dependence.

4.3 Validation of the simulated cell

In order to gain advantage from the MD simulations, first the simulated cell has to be properly validated by the direct comparison with experimental results. The simulated static structure factor has been contrasted against the WAXS results, while the simulated intermediate scattering function of the hydrogens has been directly compared with NSE results. Afterwards, the comparison among experimental and simulated results has been extended to the relaxation times of the hydrogen self motions proving finally that the simulated sample really mimics the real one and the procedure used to analyse the data is consistent. Once that such procedure has been completed and the simulated PVME can be relied on, the simulations can be exploited to unveil the particular details of the structure and the dynamics of dry PVME. This last part will be extensively deepened in the next paragraph.

Structure
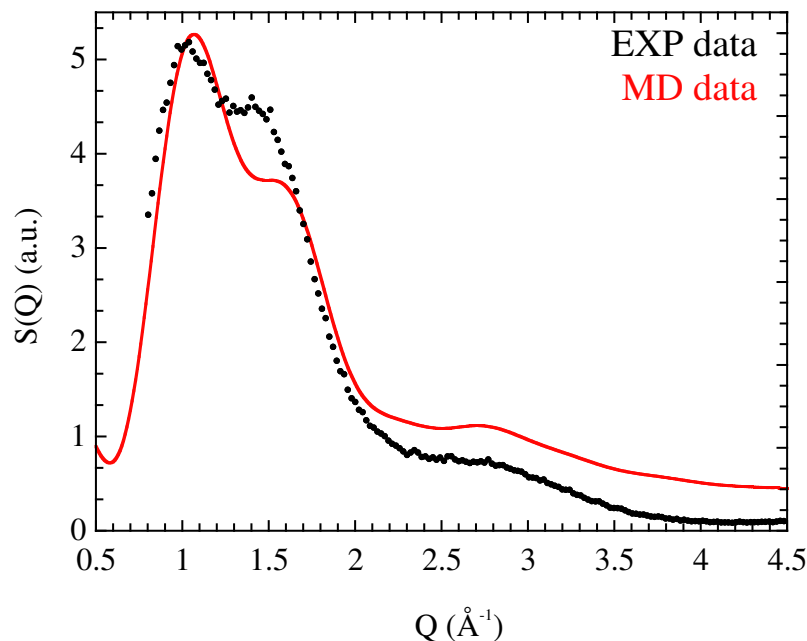
Figure 4.7: Simulated X-ray static structure factor (red solid line) of dry PVME contrasted against the experimental WAXS diffraction pattern (black symbols) measured at the CFM at the temperature of $300\,K$.

The results obtained through the WAXS measurement performed at the CFM on the PVME sample at $\approx 300\,K$ are compared to the simulated one computed at $300\,K$ in Fig. 4.7. Since measurements with the imaging plates do not provide results in absolute units, the data are shown in arbitrary units and the scales have been chosen such that the intenstiy of the first peak is nearly the same. The simulations reproduce the overall features and the position of the three peaks rather good.

In Fig. 4.8 the temperature dependence of the simulated X-ray diffraction pattern of dry PVME is represented along ESRF data of the real sample at the temperatures closest to those investigated by MD simulations. Increasing the temperature the real sample exhibits two phenomena: (i) the position of the maximum of the first peak shifts toward smaller Q-values and (ii) the
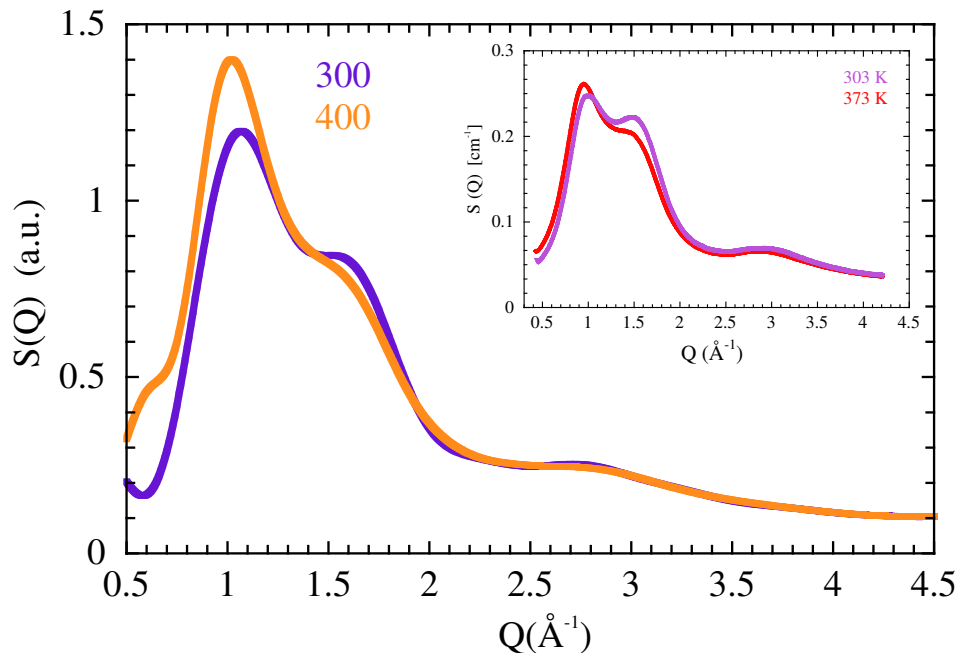
Figure 4.8: X-ray diffraction patterns of simulated dry PVME sample at the two limit temperature of 300 (violet solid line) and $400\,K$ (orange solid line) contrasted against the ESRF results, shown in the insert of the Figure at the temperature of 303 (violet solid line) and $373\,K$ (red solid line).

intensity of both the peaks changes being enhanced the first one, so that at the highest temperature the second peak appears as a shoulder. The third peak is temperature independent in both sets of data. The simulated pattern reproduce very well all these features. It can be thus concluded that the simulated structure describes rather well the short-range order of PVME and the temperature dependence of the simulated sample reflects that of the real one.

Dynamics

In Fig. 4.9 the NSE data previously shown are represented along with the simulated intermediate scattering functions computed for all PVME hydrogens.

Since the experimental data decay faster than the simulated ones, to
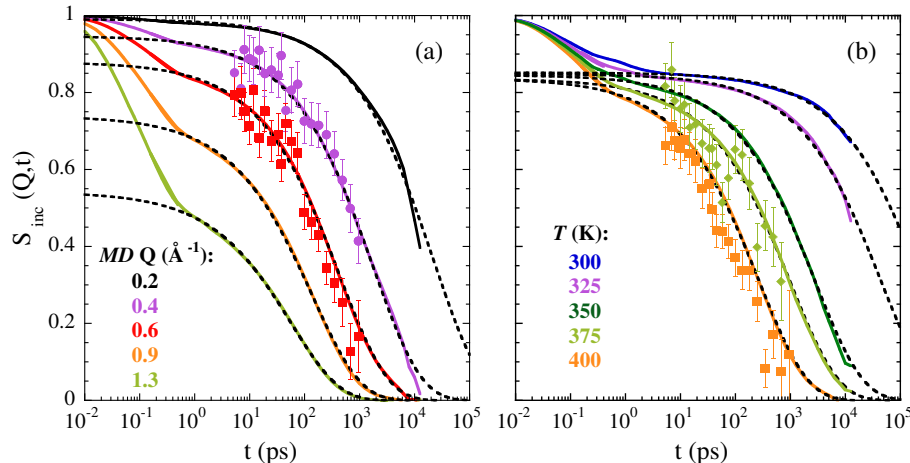
Figure 4.9: Direct comparison between simulated (solid lines) and experimental (symbols) total hydrogen $S_{inc}^{H}(Q,t)$. (a) NSE data at $Q = 0.37\text{Å}^{-1}$ (circles) and $Q = 0.6\text{Å}^{-1}$ (squares) at $400\,K$ are represented along with simulated data at the indicated Q-values. (b) Experimental and simulated data at $Q = 0.72\text{Å}^{-1}$ at the written temperatures are shown. The simulated data are shifted by 0.5 decades toward faster times in both graphs. The dashed lines represent the KWW fits.

match both sets of data the timescales of the latter have been shifted by 0.5 decades. As it can be seen in the figure, allowing such small shift the agreement is excellent and it can be concluded that the simulated sample is reliable also concerning the dynamics. The simulated data were so analized following the same procedure developed for the experimental ones. As it can be observed in Fig. 4.9, the KWW functions fit very well the long-time regime, supporting once again the consistency of the followed procedure.

To extend the comparison between simulated and experimental data to all Q- and T-values investigated, all the corresponding intermediate scattering functions were computed and the relaxion times of all the hydrogens were calculated. Allowing the shift of 0.5 decades toward faster times to the simulated data, a nearly perfect overlap among all the data is obtained, as it is shown in Fig. 4.10. Shifts in temperature and/or timescale have been already observed in other different systems as orthoterphenyl [177],
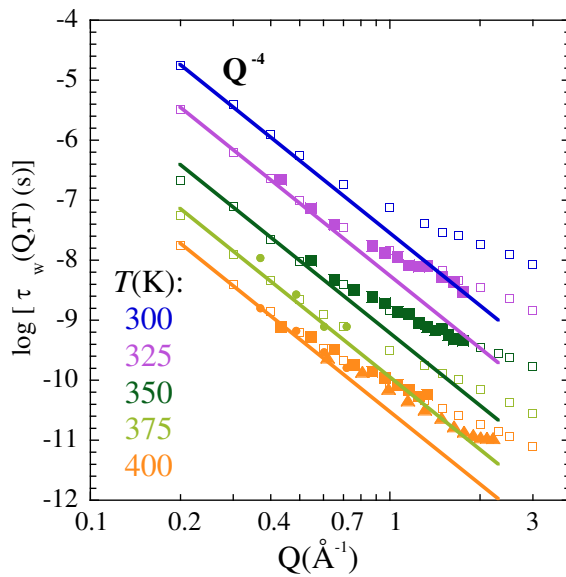
Figure 4.10: *Q*-dependence of the characteristic relaxation times obtained from the KWW analysis at the indicated temperatures. Solid symbols represents experimental data and empty symbols the simulated ones. The solid lines represent a Q^{-4} dependence and the simulated data are shifted by 0.5 decades toward faster times.

polyisoprene [178], poly(methyl methacrylate) [172, 179], poly(vinly acetate) [162], and poly(ethylene propylene) [180] and they are usually required for a perfect matching of MD-simulations and real sample results. Apart from slight differences in the microstructure or in the density, a possible source for this discrepancy could be that the force field used in the simulations was not perfectly calibrated. In any case, it can be stated that, allowing this small shift in timescales, the dynamical features of PVME are captured by the simulated cell in an excellent way.

4.4 Discussion

Once that experimental and simulated data have been compared and it has been checked that the simulated sample is reliable regarding both dynamical and structural properties, it is possible to go further with the

analysis of PVME, studying the physical magnitudes accessible only through fully atomistic molecular dynamics simulation.

4.4.1   Disentangling the contributions to the static structure factor

The partial static structure factors weighted by the atomic form factor, as they have been defined in the expression Eq. (3.9), have been computed to better visualize the contributions to the total static structure factor.
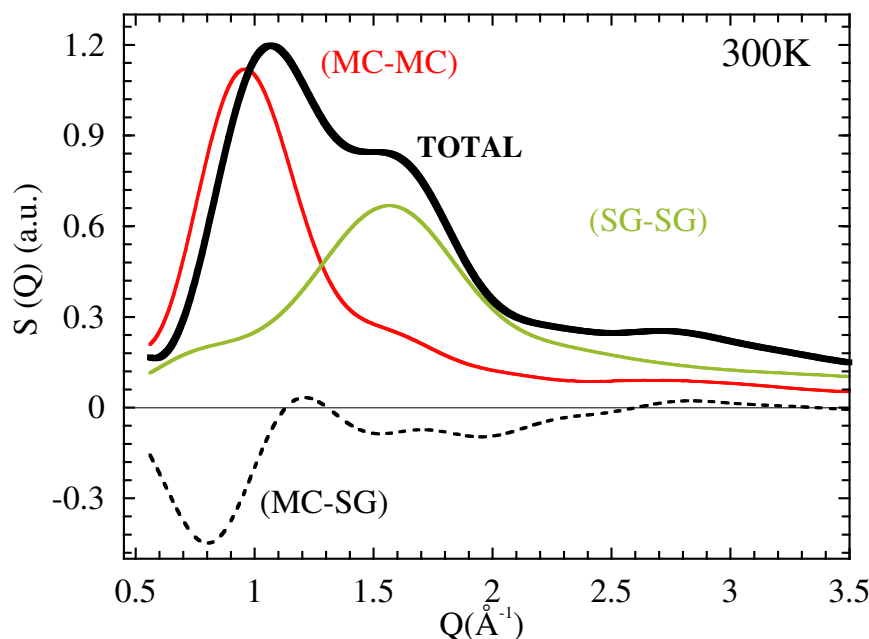

Figure 4.11: Partial static structure factors corresponding to the different atomic correlations within the molecular groups considered at $300\,K$: main chain (MC-MC), side group (SG-SG). The cross correlations (MC-SG) and the total (TOTAL) static structure factor are also represented.

To this end it is useful to group the 10 atoms forming the PVME monomer into 2 functional groups: the main chain group (*MC*), which contains all the hydrogens and the carbons belonging to the main chain, and the side group (*SG*), which is formed by the oxygen and the methyl group atoms. In Figure 4.11 the partial static structure factor of the two different groups is

represented along with the cross term and the total one, all computed at the temperature of $300\,K$.

MC-MC: The *main chain-main chain (MC-MC)* correlation function exhibits a very pronounced peak at $Q \approx 0.95\text{Å}^{-1}$, a very close value to the position of the first peak of the total static structure factor evaluated at this temperature, $Q \approx 1.06\text{Å}^{-1}$. In literature such peak found in polymers is traditionally attributed to intermolecular correlations [181]. So, assuming that it mainly arises from intermolecular correlations, the distance between two chains can be estimated by means of the Bragg approximation and it results $d_{MC-MC} = 2\pi/Q \approx 6.61\text{Å}$. An asymmetric broadening of the first peak is observed in the Q region corresponding to the position of the second peak of the total static structure factor, while in correspondence of its third peak, only a hint of it is present in the MC-MC function.

SG-SG: The *side group-side group (SG-SG)* correlation function is characterized by one broad peak positioned at $Q \approx 1.57\text{Å}^{-1}$, which is very close to the position of the maximum of the second peak of the total static structure factor

MC-SG: Main chain and the side group show an anticorrelation behaviour, revealed by the negative value of the functions at a value of Q close to that of the first peak of the total static structure factor. This kind of behaviour has been reported for other polymers with bulky side group as PMMA [182] or PVAc [162] and hints a tendency of local separation of the side group and the main chain [183, 184]. In those cases this feature is much more pronounced and for PMMA it has been even interpreted as a precursor for the monophase separation observed for poly(*n*-alkyl methacrylates).

Fig. 4.12 shows all the computed static structure factors at the two limit temperatures of 300 and $400\,K$. Concerning the total static structure factor, it is observed that on heating the position of the first peak shifts towards lower Q-values from 1.06Å^{-1} to 1.02Å^{-1}. This behaviour is observed in other polymers and has been attributed to the intermolecular character of
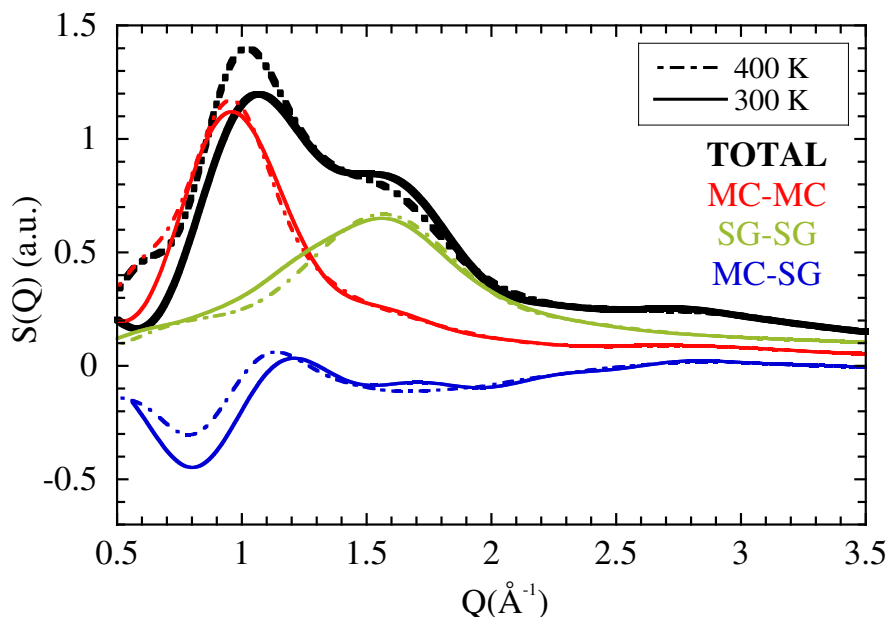
Figure 4.12: Total and partial static structure factors computed at the temperature of 300 (solid line) and $400\,K$ (dashed-dotted line) as indicated in the legend.

the correlations [182, 185]. The intensity of the second peak decreases making it appearing as a shoulder of the first one. On the contrary, its position does not change, pointing to the idea of a predominant intramolecular origin of the correlations contributing to such peak.

As it can be observed, the intensity of the MC-MC main peak placed at $Q \approx 0.95\text{Å}^{-1}$ increases on increasing temperature, while the position remains unchanged. Regarding the SG-partial static structure factor, the intensity of the peak is slightly temperature dependent, while the flank at low Q-values broadens on heating. The main features of the MC-SG correlation are the change in the intensity of the first negative peak placed at $Q \approx 0.8\text{Å}^{-1}$ and the shift of the position of the first positive peak from $Q \approx 1.20$ to $Q \approx 1.11\text{Å}^{-1}$. So, the shift on heating of the first peak of the total static structure factor toward lower Q-values can be ascribed solely to the feature of the MC-SG cross-correlations, which also contribute to the increase of its

intensity.

4.4.2 Dynamics in the α-relaxation: crossover from Gaussian to non-Gaussian behaviour

To better analyze the behaviour of the real and the simulated characteristic relaxation times a mastercurve has been built from the data shown in Fig. 4.10. It is represented in Fig. 4.13 using the same symbols and the same colors.
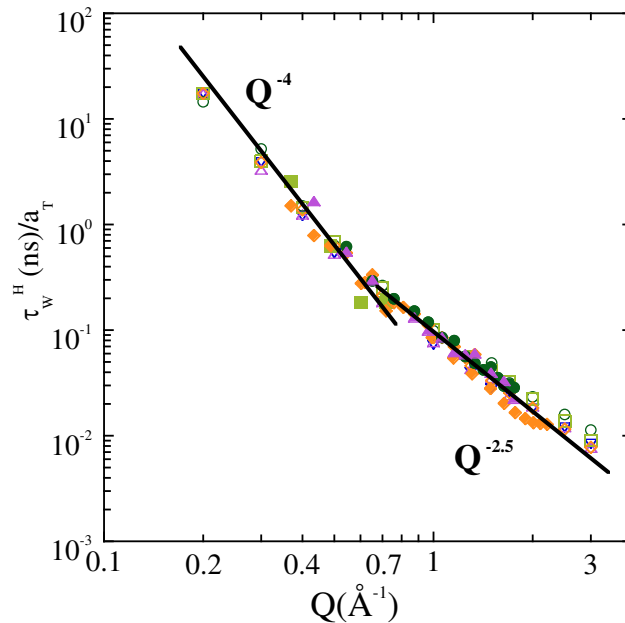

Figure 4.13: Master curve of the simulated and experimental characteristic relaxation times obtained fixing $T_r = 400\,K$ as the temperature reference and shifting the data by a factor a_T. Solid lines show the crossover from the Gaussian law Q^{-4} governing the low Q regime to a non Gaussian dependence Q^{-x}, with $x = 2.5 \pm 0.5$, at high Q-values. Solid symbols represent experimental data and empty symbols the simulated ones.

The mastercurve is constructed by using a shift factor a_T and a reference temperature, in this case $T_r = 400\,K$. In this way, the values τ_w/a_T collapse on the corresponding data to T_r. Within the uncertainties, the agreement between simulated and experimental data is excellent supporting once again

the reliability of the simulated sample. The collapse on a single curve implies that the Q-dependence followed by the relaxation times is independent of temperature [178]. In the Q-range below $\approx 0.7\text{Å}^{-1}$ a Q-dependence of $\tau_w \propto Q^{-4} = Q^{-2/\beta}$ is exhibited. Taking into account that, in the analysis procedure, the value of the shape parameter β was fixed to 0.5, this feature reflects a Gaussian functional form for the intermediate scattering function, as it has been expressed in (3.13)

$$S^H_{inc}(Q,t) = S^{gauss}_s(Q,t) = exp\left[-\frac{< r^2(t) >}{6}Q^2\right] \tag{4.5}$$

and, consequently, so it is the self-part of the van Hove correlation function

$$G^{gauss}_s(r,t) = \left[\frac{\alpha(t)}{\pi}\right]^{3/2} exp[-\alpha(t)r^2] \tag{4.6}$$

in which $< r^2(t) >= 3/[2\alpha(t)]$.

In the higher Q-regime strong deviations from this behaviour are evident and a weaker power law of $\tau_W \approx Q^{-x}$ with $x = 2.5 \pm 0.5$ describes the data. Such crossover from a Gaussian to a non Gaussian behaviour is in agreement with previously PVME literature data [164, 186, 187]. It has been also observed in other polymers in the Q-range of $0.6 - 1\text{Å}^{-1}$ [163, 168, 171, 172, 178, 180, 188, 189]. In the case of $1, 2 - PB$ [171] and $1, 4 - PB$ [190] MD simulations played a fundamental role in claryfing that chemical heterogeneity is one of the origins of the deviations from the Gaussian behaviour.

Therefore, even if it has been shown that the rotation of the methyl group affects only the fast region, to discard effects originated from such additional motion, this study will be focused on the main chain cH hydrogen motion with the aim of revealing the origin of the deviation from the Gaussian behaviour. The self-part of the van Hove correlation function of cH, $G^{cH}_{self}(r,t)$ at the two computed limit temperatures has been represented in Fig. 4.14.
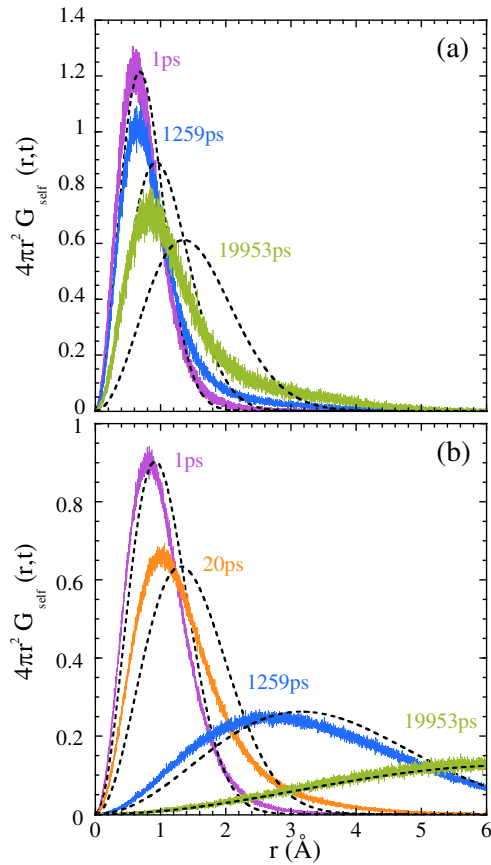
Figure 4.14: cH self van Hove correlation functions evaluated at the different indicated times at the temperatures of (a) $300\,K$ and (b) $400\,K$. Dashed lines are the Gaussian approximation computed using the simulated mean squared displacements at the corresponding time.

At $300\,K$, Fig. 4.14 (a), the hydrogen motion is localized in a region smaller than ≈ 2Å with the $G_{self}^{cH}(r,t)$-peak centered below ≈ 1Å. Close to the limit of the performed simulation $(20\,ns)$ the distribution function shifts its maximum and broadens manifesting the onset of a diffusive-like process. At $400\,K$, Fig. 4.14(b), the distribution starts straight broadening with increasing time. The peak shifts toward larger distances revealing the diffusive feature of the hydrogen motion at higher temperature.

The mean squared displacements $< r_{cH}^2(t) >$, depicted in Fig. 4.15, show
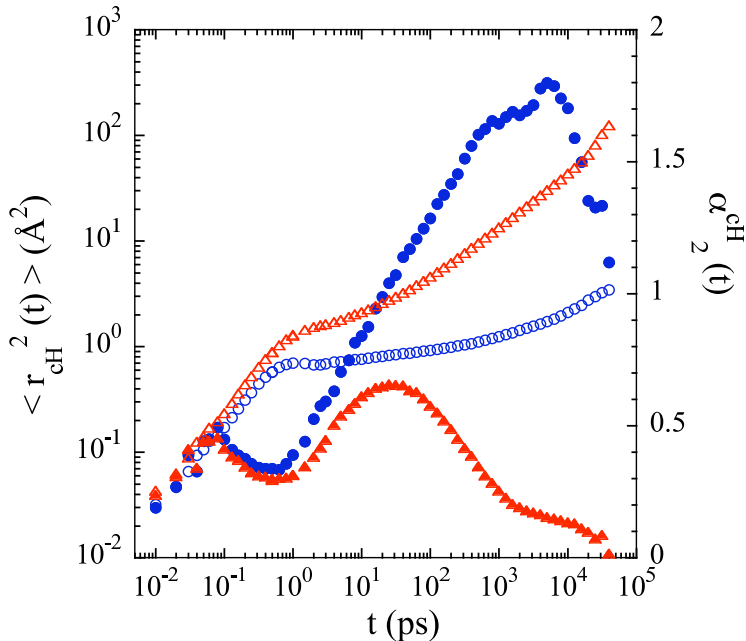
Figure 4.15: Time evolution of the mean squared displacements (empty symbols) and of the non-Gaussian parameter $\alpha_2(t)$ (full symbols) at $300\,K$ (circles) and $400\,K$ (triangles) of the cHs.

a continuos increase starting at $\sim 2\,ps$ confirming this feature.

In the microscopic regime, below $1\,ps$, both temperatures are characterized by a similar rapid increase in $< r^2_{cH}(t) >$. For time longer than $1\,ps$, the cH mean squared displacements at $300\,K$ become almost constant for about three decades until at $\approx 3\,ns$ they start to increase again. In the plateau-region comprised between $\approx 1\,ps$ and $\approx 3\,ns$ the hydrogens are trapped in the cage formed by their neighbours. At $400\,K$ the effect of the cage is only slightly hinted: the mean squared displacements show a sublinear regime $< r^2_{cH}(t) > \propto t^{0.5}$ starting already at $\approx 20\,ps$. Such feature is a characteristic specific of the dynamics of glass-forming polymers indicating the crossing of the segmental dynamics over Rouse motion at longer times and larger length scales [191].

In the Fig. 4.14 the Gaussian approximation of the self-part of the van Hove correlation function is represented through dotted lines to be directly

compared with $G_{self}^{cH}(r,t)$. While at $300\,K$ severe deviations from the Gaussian behaviour start above some picoseconds, at $400\,K$ the deviations appear in the time range comprised between 10 and $100\,ps$, while the agreement at short and very long time is quite good.

It is possible to directly compare in the reciprocal space the simulated intermediate scattering function with that expressed in terms of its Q^2-expansion in Eq. (3.15):

$$S_{inc}^{Gauss}(Q,t) = exp\left[-\frac{<r^2(t)>}{6}Q^2 + \frac{\alpha_2(t)<r^2(t)>^2}{72}Q^4 + ...\right] \quad (4.7)$$

The results for the two limit temperatures and three different Q-values are shown in Fig. 4.16. The Gaussian approximation and the first correction term of the Q^2-expansion of the intermediate scattering function are represented as solid and dashed lines respectively. As it can be observed, the intermediate scattering function can be well described by the Gaussian approximation at $Q = 0.7\text{Å}^{-1}$, noticeable deviations start to appear at $Q = 1\text{Å}^{-1}$ and for high Q values ($\approx 2\text{Å}^{-1}$) an overall disagreement is observed. If the leading correction is comprised, with the $\alpha_2(t)$ parameter evaluated from the moments of $G_{self}^{cH}(r,t)$, the approximation of the intermediate scattering function works quite well up to $Q \approx 1\text{Å}^{-1}$, where the data start to slightly deviate. At higher Q-values, such correction is still insufficient to describe the $S_{inc}^{cH}(Q,t)$ pattern and further terms are needed.

To be worth noting is that the cH incoherent scattering function still exhibits two dynamic regimes even in absence of the methyl group contribution to the motion and in the real space strong evidences of the cage effect are observed. These observations suggest the use of the MCT to analyse the dry PVME dynamics to find a microscopic theoretical framework to explain the deviations from the Gaussian behaviour.
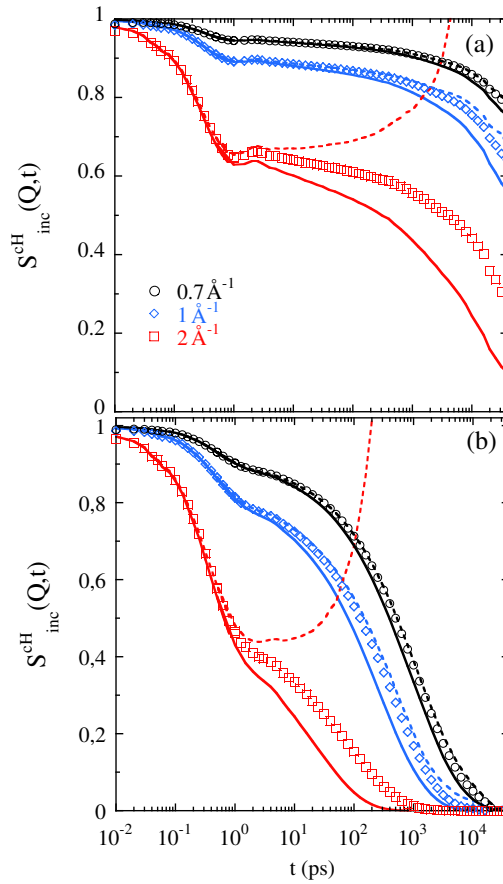
Figure 4.16: cH intermediate scattering function evaluated at (a) $300\,K$ and (b) $400\,K$ at the indicated Q-values. The solid lines represent the Gaussian approximation and the dashed lines include the first correction of the Q^2-expansion of the scattering function.

4.4.3   Analysis in the light of MCT

The MCT and its predictions have been introduced in the paragraph 1.1.4. Here without invoking the knowledge of any exponent parameter, the MCT preditions will be first tested to check if such theory works with the simulated dry PVME sample and then the system will be analyzed. The intermediate scattering functions of the following species of atoms will be considered as correlation functions $\phi_Q(t)$: main chain hydrogens (cH), main-chain carbons (cC) and all the hydrogen (H).
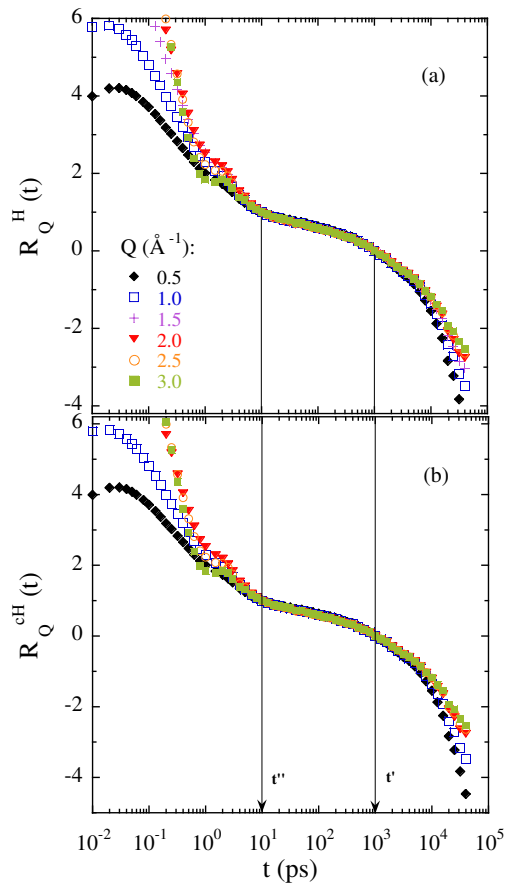
Figure 4.17: Factorization theorem applied to the correlation functions $\phi_Q(t)$ of the (a) Hs and the (b) cHs at $300\,K$ at the indicated Q-values. t' and t'' represent the limits of the β-window.

First the factorization theorem expressed in eq.(1.14) has been checked in the direct and in the reciprocal space. If it holds, in the reciprocal space in the β-regime the ratio

$$R_Q(t) = \frac{\phi_Q(t) - \phi_Q(t')}{\phi_Q(t") - \phi_Q(t')} \tag{4.8}$$

must be Q-independent, with t' and t'' the limits of the β-window.

In Fig. 4.17 $R_Q(t)$ is represented for the H and cH correlation functions at $300\,K$. The superposition in the regime comprised between $5\,ps$ and $3\,ns$

99

is completely fulfilled. The same feature is also found for cC species of atoms.

In the β-regime the factorization $G(r,t) = F(r) + H(r)G(t)$ is expected also in the real space. The ratio

$$R_{self}(r,t) = \frac{G_{self}(r,t) - G_{self}(r,t')}{G_{self}(r',t) - G_{self}(r',t')} = \frac{H(r)}{H(r')} \tag{4.9}$$

with r' constant is thus independent of time and provides information on the length scale involved in the self-atomic motions. As it can be observed in Fig. 4.18, an excellent superposition is reached in the time range of $10\,ps \leq t \leq 400\,ps$, which is almost the same time window found in the reciprocal space and shown in Fig. 4.17. At faster and longer times (about $700\,ps$) failure of such superposition is found. A similar situation was reported for a model polymer melt [192] and the binary Lennard-Jones mixture [55].

Concerning information on the length scales of the process involved, in part (a) of Fig. 4.18 it can be observed that cC motion is limited to displacements smaller than 3Å. The intermolecular distance can be estimated as $d_{chain} \approx 2\,\pi/Q_{1MAX}$. Being $Q_{1MAX} \approx 0.9\,\text{Å}^{-1}$, it results $d_{chain} = 6.98$Å, bigger than the limiting distance of the cC motion at $300\,K$. Moreover $R^{cC}(r,t)$ exhibits at small distances a positive peak vanishing at $r_o = 0.76$Å and a negative peak at longer distances.

The function $H(r)$ provides the rate at which the self van Hove correlation function relaxes [21]:

$$\frac{\partial G_{self}(r,t)}{\partial t} \propto -H(r) \tag{4.10}$$

The negative proportionality implies that the probability of the atomic displacements of dimension r decreases where $H(r)$ is bigger, $r \approx 0.4$Å in this case, and increases where $H(r)$ is smaller, $r \approx 1.1$Å. This last distance is much smaller than d_{chain}, suggesting that attempts to overcome distances of the order of the intermolecular separation are partially reflected back and the atom returns close to its initial position [21, 193].
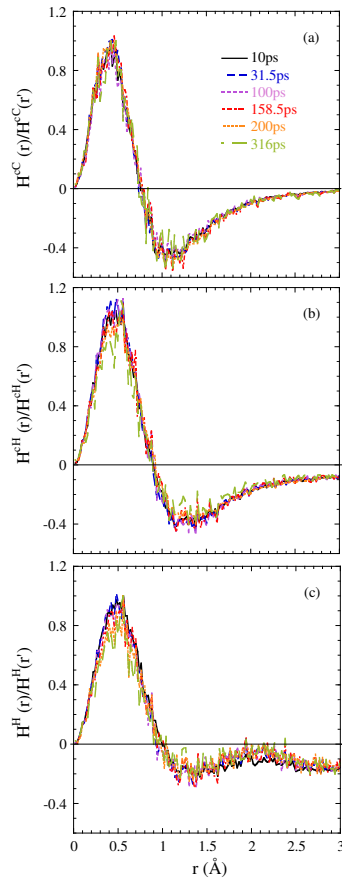
Figure 4.18: Factorization theorem in the real space calculated for (a) cCs, (b) cHs and (c) Hs at the temperature of $300\,K$ at the different indicated times. The values of r' have been chosen to maximize the denominator in eq.(4.9) [$r'(cC) = 0.42$Å, $r'(cH) = 0.52$Å, r'(H)$= 0.56$ Å]

In Fig. 4.18 (b) $R_{cH}(r,t)$ is represented. The pattern is similar to that exhibited by cC atoms, though the delocalization is slightly larger. A striking result is inferred from the comparison between the pattern of $R_{cH}(r,t)$ and $R_H(r,t)$: at large distances $R_H(r,t)$ shows a second negative peak absent in $R_{cH}(r,t)$. Such peak corresponds to the other two equivalent positions occupied by the methyl group hydrogens in the rotational motion in the time range investigated.

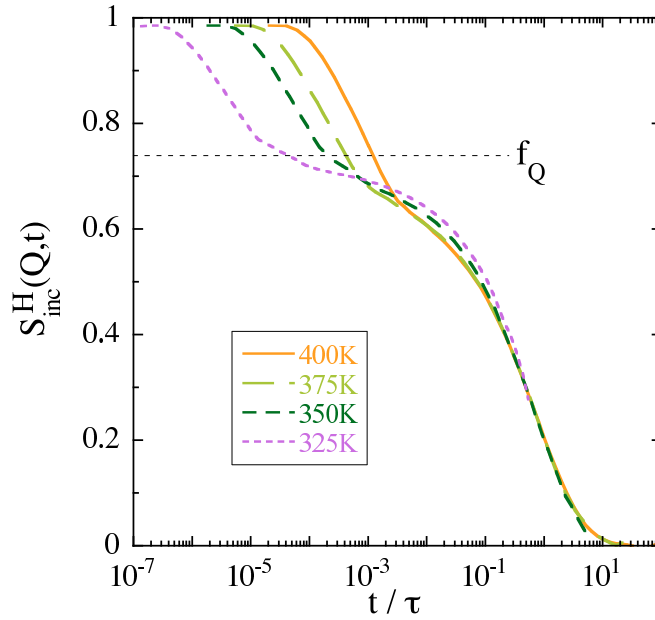The time-temperature superposition principle introduced by the relation

Figure 4.19: Time-temperature superposition principle for $\phi_Q(t)$ evaluated at the first structure factor peak Q-value ($Q_{1MAX} = 1.01\text{Å}^{-1}$) at the indicated temperatures.

(1.19) is another important prediction of the MCT and Fig. 4.19 shows the case of all the hydrogens. The Q-value corresponds to the maximum of the first static structure peak and the timescale chosen to collapse the data is the value at which the different intermediate scattering functions reach 0.2 [194]. The lowest temperature has not been included because the decay of such correlation function only reaches the value of 0.5 in the explored time window. For the considered temperatures a rather good superposition is obtained.

Once that it has been checked that the MCT predictions hold for the dry PVME simulated sample, the exponent parameter can be estimated and the analysis of the data in the light of the MCT can be carried out.
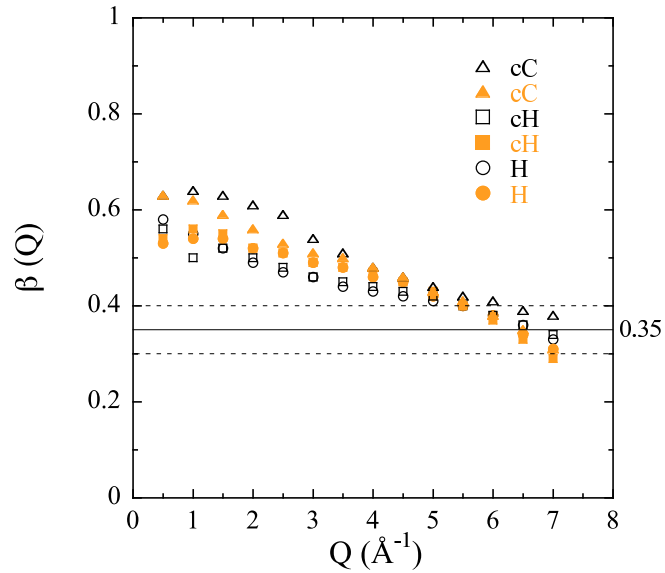
Figure 4.20: High Q-dependence of the shape parameter β evaluated at 325 (emtpy symbols) and $350\,K$ (full symbols) of $\phi_Q(t)$ of the cCs (triangles), cHs (squares) and Hs (circles).

The von Schweidler parameter b, already introduced in eq.(1.20), can be evaluated as the limit for $Q \to \infty$ of the shape parameter β [195]:

$$\lim_{Q \to \infty} \beta(Q) = b \tag{4.11}$$

In Fig. 4.20 are represented the results of such limit for the different species of atoms at the two different temperatures of 325 and $350\,K$. As the value of β at high Q is between 0.3 and 0.4, $b = 0.35$ was chosen.

Subsequently, from the relation (1.17) and (1.18)

$$\lambda = \frac{\Gamma(1-a)^2}{\Gamma(1-2a)} = \frac{\Gamma(1+b)}{\Gamma(1+2b)^2}$$

$$\gamma = \frac{1}{2a} + \frac{1}{2b}$$

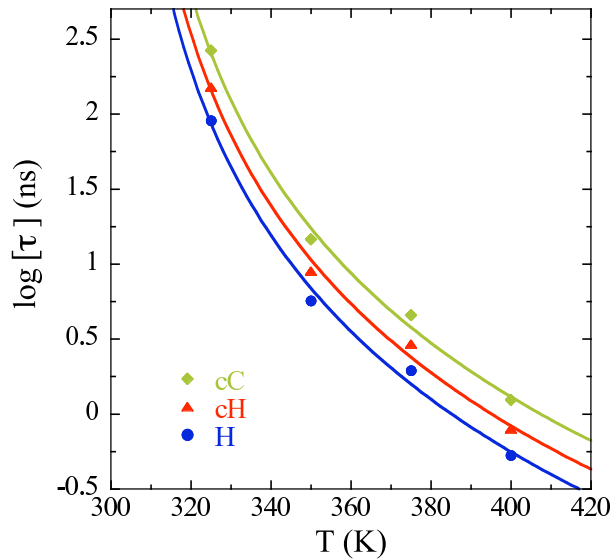$\lambda = 0.87$ and $\gamma = 3.6$ have been obtained.

Figure 4.21: Temperature dependence of the characteristic times at which the correlators $\phi_Q(t)$ corresponding to the different indicated species reach the value of 0.2. Solid lines represent the fits with the expression (4.12).

The γ-parameter determines the way the characteristic relaxation time approaches the critical temperature T_c through the following relation

$$\tau \propto |T - T_c|^{-\gamma} \tag{4.12}$$

It is usually found that $T_c \approx 1.2\,T_g$ [55, 57, 58]. Being the glass transition $T_g = 247\,K$ (see 4.1.1), it should result $T_c \approx 300\,K$. The relation (4.12) was applied to the characteristic times at which the correlation functions take the value of 0.2. As mentioned before, the temperature of $300\,K$ was excluded in the previous analysis because the correlation function do not decay to the chosen value 0.2; moreover, according to the rough estimation of T_c, $300\,K$ should be very close to the value of the MCT-T_c. In Fig. 4.21 the temperature dependence of the characteristic relaxation times is represented. The value of $\gamma = 3.6$ describes very well the data and the fits give back a value of $T_c \approx 300\,K$ in accord to the expected value. From this analysis it follows that PVME results are consistent with the MCT predictions.
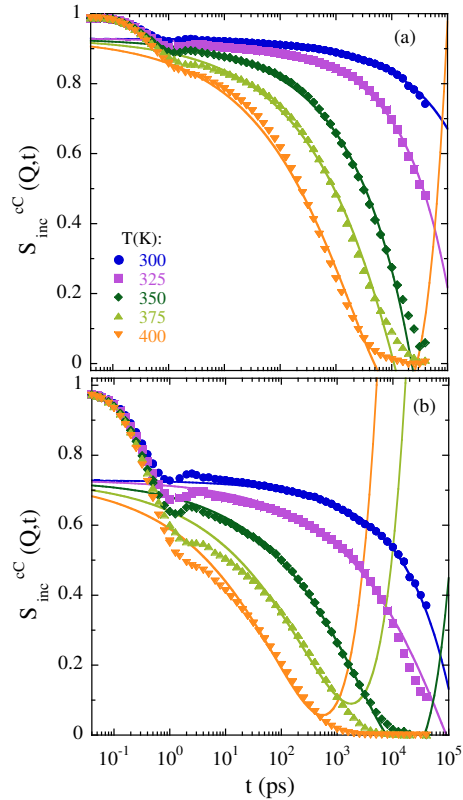
104

Figure 4.22: Fit of the MCT von Schweidler regime of the $S_{inc}^{cC}(Q,t)$ at (a) $Q = 1\text{Å}^{-1}$ and (b) $Q = 2\text{Å}^{-1}$ at the indicated temperatures. All the curves are described using an unique value of the nonergodic parameter f_Q.

In the MCT framework, the correlation functions can be described in terms of the MCT von Schweidler expansion

$$\phi_Q(t) = f_Q - H_{1Q}\, t^b + H_{2Q}\, t^{2b} + \dots \tag{4.13}$$

Figure 4.22 shows such represention calculated for S_{inc}^{cC} for two Q-values at different temperatures. All the curves S_{inc}^{cC} have been described with the same value of f_Q, again in agreement with the MCT predictions, since $f_Q = f_Q^c$ for temperatures above T_c. The values obtained for f_Q are depicted in Fig. 4.23 for all the species of atoms investigated.
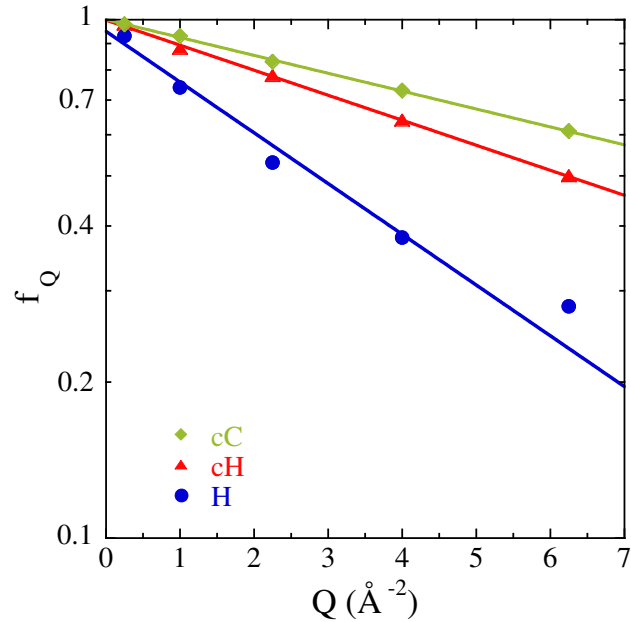
Figure 4.23: Q-dependence of nonergodic parameter f_Q of the indicated species of atoms. Solid lines represent the fit with the Gaussian approximation $f_Q = exp(-Q^2 r_{sc}^2)$.

The nonergodic parameter behaviour is described in terms of a Gaussian function, $f_Q = \exp(-Q^2 r_{sc}^2)$, in which r_{sc} is the localization length and such description is shown through solid lines in Fig. 4.23. It has been estimated that r_{sc} is 0.28Å for the carbons and 0.47Å for the main chain hydrogens. f_Q of all the hydrogens clearly manifest deviations from the Gaussian behavior and it is supposed that such feature stems from the methyl group rotations.

Since the MCT von Schweidler expansion describes very well the decay of the correlation functions at the different temperatures, it can be tested if the parameters H_{1Q} fulfill the following MCT relation:

$$H_{1Q} \propto |T - T_c|^{\gamma b} \tag{4.14}$$

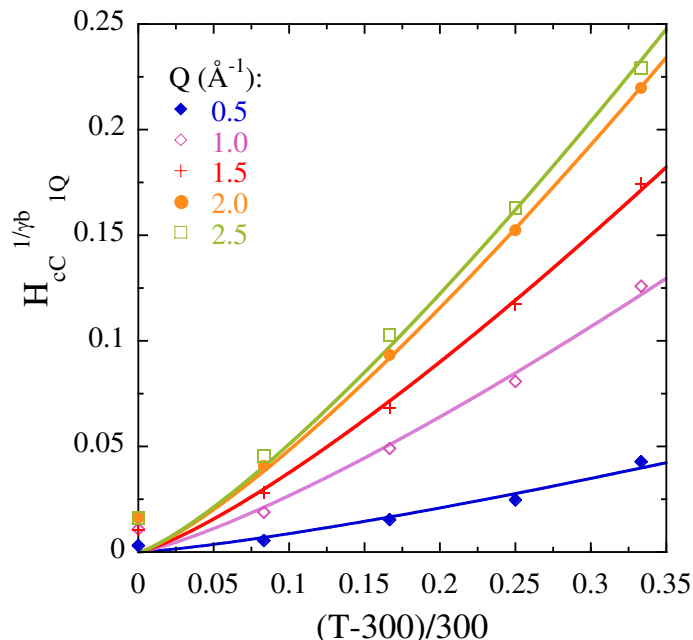In Fig. 4.24 H_{1Q} values and the fits $|T-T_c|^{\gamma b}$ with b, γ and T_c values fixed

Figure 4.24: Temperature dependence of the H_{1Q}-parameter of the MCT von Schweidler expansion of $\phi_Q(t)$ for cCs at the indicated Q-values. Solid lines show the fit with eq.(4.14).

to those previously computed are shown. The agreement among the data and the fits is excellent.

According to the prediction of the MCT (see Eq. (1.20)), in PVME sample it is found that in the high-Q limit $Q^{-1/b} = Q^{-2.86}$, which is compatible with the experimental and simulated feature presented in Fig. 4.13. So, the deviations from Gaussian behaviour found in experimental and simulated data could be understood within the general framework provided by the MCT. Consistent results have been so far obtained with the analysis of PVME data in the light of the MCT. The parameter b, γ and T_c provide a good description of the system. As it can be seen from the table 4.25, the high value of $\lambda = 0.87$ is quite unusual compared to other glass-forming systems [45, 177, 196, 197]. A similar high value $\lambda = 0.93$ has been reported for a fully atomistic $1, 4 - PB$ study and it was attributed to the local conformational

SYSTEM	a	b	γ	λ
hard spheres	0.31	0.58	2.5	0.74
o-terphenyl	0.30	0.54	2.6	0.76
polyethylene (UA)	0.27	0.46	2.9	0.81
poly(vinyl methyl ether) (FA)	0.23	0.35	3.6	0.87
1,4-polybutadiene (UA)	0.21	0.30	4.1	0.90
1,4-polybutadiene (FA)	0.18	0.24	4.9	0.93

Figure 4.25: MCT exponents for different glass formers [198]. UA and FA denote, respectively, coarse-grained united atom and fully atomistic models. PVME sample studied in this PhD thesis is in red.

changes controlled by rotational barriers, which affect the dynamics of the polymer segments within the cage [52]. In a recent work on MD-simulations of a simple model for polymer melts with intramolecular barriers, it has been found that there is a clear correlation between the exponent parameter and chain stiffness [198]. The competition between packing effects and intramolecular barriers is suggested to be the mechanism responsible for the increase of λ from 0.76, for fully flexible chains (like the bead-spring models referred to in [21], which do not include rotational barriers), to $\lambda \approx 0.90$, for very stiff chains. Chemically realistic polymer models seem to exhibit λ-values approaching the limit $\lambda = 1$: a united atom model of polyethylene reveals $\lambda = 0.81$ [199], of $1,4-PB$ $\lambda = 0.90$ [53] and a fully atomistic model of $1,4-PB$ gives $\lambda = 0.93$ [52].

The results so-obtained on PVME sample thus supports the scenario proposed by Bernabei *et al.* [198] in which real polymers should be classified in the family of complex systems as short-ranged attractive colloids [200–202] or binary mixtures with strong dynamic asymmetry [203–206]. The unusual large λ-values exhibited by them could reveal an underlying high-order MCT transition.

Moreover, the deviations from the Gaussian behaviour shown by the char-

acteristic timescales of several polymers at high-Q values could be described by asymptotic power-laws Q^{-x} with $x \approx 2\dots2.5$. Since the intermediate scattering functions are usually described with β-values close to 0.5, assuming that the b-parameter is not very different from β, the behaviour at high Q-regime would be compatible with the $Q^{-1/b}$-dependence predicted by MCT in other polymer systems.

4.4.4 The anomalous jump diffusion model

In the following the simulated data will be analyzed in the light of a simple model which implicitly contains the concept of the cage. The *anomalous jump diffusion model* is a generalization of the jump diffusion model, which is based on the idea of the existence of a distribution of a discrete jumps underlying the atomic motion in the α process [178]. In this scenario, an atom remains in a given site for a time τ_0, vibrating around a center of equilibrium [207–209]. After τ_0, it moves rapidly to a new position separated from the original one by a vector $\vec{l}$. The self intermediate scattering function assumes the following form

$$S_{self}^{JD}(Q,t) = exp\left[-\frac{<u^2>}{3}Q^2 - b(Q)\left(\frac{t}{\tau_0}\right)\right] \qquad (4.15)$$

in which $b(Q)$ depends on the particular geometry of the jump involved. Assuming randomly oriented jump directions with an exponential distribution of jump lengths

$$f_0(l) = \frac{l}{l_0^2}exp\left(-\frac{l}{l_0}\right) \qquad (4.16)$$

in which l_0 is the preferred jump distance, it results

$$b(Q) = Q^2 l_0^2 \frac{1}{1 + Q^2 l_0^2} \qquad (4.17)$$

In the limit of $Q\,l_0 \to 0$, $b(Q) \to Q^2\,l_0^2$ and $S_{self}^{JD}(Q,t)$ has a Gaussian form.

Glass-forming systems exhibit a KWW form for the intermediate scattering function. In order to describe such systems by means of this model it is necessary to introduce the stretching parameter β in the time-dependent part of Eq. (4.15). The following expression for the self intermediate scattering function which is analogous to the Eq. (4.15) is so obtained:

$$S_{self}^{JD}(Q,t) = exp\left[-\frac{<u^2>}{3}Q^2 - b(Q)\left(\frac{t}{\tau_0'}\right)^\beta\right] \tag{4.18}$$

In this way, as in the simple jump diffusion model, in the limit of $Ql_0 \to 0$ the Gaussian approximation is found.

Within this approach τ_w, $\alpha_2(t)$ and $<r^2(t)>$ may be directly calculated and their expressions are:

$$\tau_w = \tau_0'\left[1 + \frac{1}{Q^2\,l_0^2}\right]^{1/\beta} \tag{4.19}$$

$$<r^2(t)> = 2<u^2> + 6l_0^2\left(\frac{t}{\tau_0'}\right)^\beta \tag{4.20}$$

$$\alpha_2(t) = \frac{72l_0^4\left(\frac{t}{\tau_0'}\right)^\beta}{[\,2<u^2> + 6\,l_0^2\left(\frac{t}{\tau_0'}\right)^\beta]^2} \tag{4.21}$$

As it has been previously done, to rule out the heterogeneous behaviuor of the different PVME protons as the origin of the observed deviations from Gaussianity, in the following the study will focus on the dynamics of the main chain hydrogens, cH.

Figure 4.26 shows the simulated characteristic relaxation times of the cH hydrogens, $\tau_w(Q)^{cH}$, at $400\,K$. As it can be observed in the mastercurve evaluated for all the hydrogens of the sample, at $Q \approx 0.7\text{Å}^{-1}$ the behaviour of the $\tau_w(Q)^{cH}$ starts to deviate from the Gaussian one, described by a power law of $\tau \propto Q^{-4}$. The origin of the crossover from Gaussian to non-Gaussian behaviour cannot stem solely from the heterogeneous dynamics exhibited by different species of atoms. The result of the fit of the characteristic relaxation

times (Eq.(4.19)) is displayed in Fig. 4.26 as solid line. It gives $\ell_0 = 0.45$Å as the value of the characteristic jump distance of the main chain hydrogen.
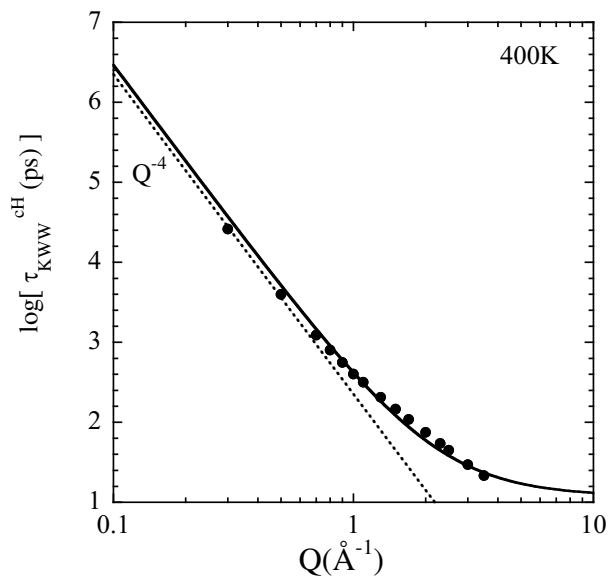

Figure 4.26: Q dependence of the simulated characteristic time of the main chain PVME protons at $400K$. The dotted line represents the Gaussian dependence of τ_{KWW}^{cH} and the solid line the fit with the anomalous jump diffusion model.

The good agreement between the data and the fit suggests that the anomalous jump diffusion model captures in a semiquantitative way the PVME dynamics in the temperatures and time window considered and it may be used to effectively describe the crossover from Gaussian to non-Gaussian behaviour. The model involves a heterogeneous picture for the self-atomic motions at the origin of the α relaxation regime which manifests at short length scales. There, each atom can jump over different distances at each moment; at large Q values, short length scales, the system looks heterogeneous and non-Gaussianity is evident, while for small Q values, large length scales, the scattering process is sensitive to the motion over many diffusive elemental steps and the result does not depend on the nature of a single step. Then, the sublinear diffusion is reached and the system becomes Gaussian.
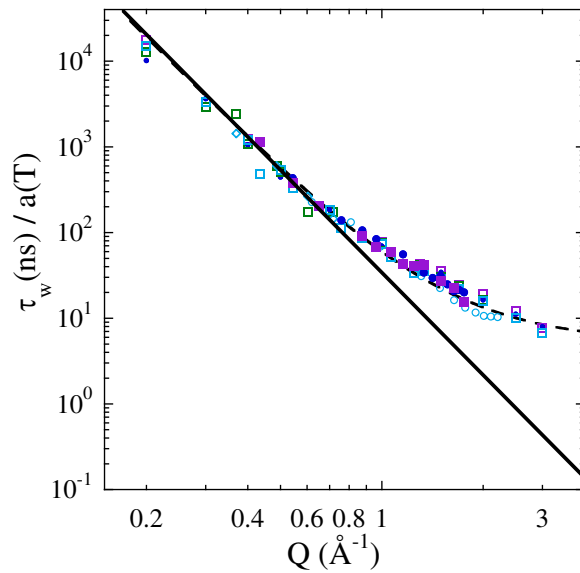
Figure 4.27: Q-dependence of the characteristic relaxation times of all the hydrogen of dry PVME. Data are the same of Fig. 4.13. The solid line represents the Gaussian dependence of τ_{KWW} and the solid line the fit with the anomalous jump diffusion model. It results $\ell_0^{dryPVME} = 0.65\text{Å}$

Since the experimental results of dry PVME will be used as reference for the study of the PVME water solution in the next chapter, the anomalous jump diffusion model has been applied also to parametrize the Q-dependence of the intermediate scattering function of all the hydrogen atoms in dry PVME. It is represented in Fig. 4.27 and the value of the characteristic jump distance results to be $\ell_0^{dryPVME} = 0.65\text{Å}$.

CHAPTER 5

WATER PVME CONCENTRATED SOLUTION

5.1 Experimental details

5.1.1 Sample and experimental conditions

The PVME sample was purchased from Sigma-Aldrich with water content of $c_w = 50wt\%$ in weight. It was dried out and hydrated again with the desired amount of water. To take advantage of the selective labelling in the NS experiments, two solutions were prepared: $PVME/H_2O$ with water content of $c_w = 30wt\%$ in weight and $PVME/D_2O$ with water content of $c_{D_2O} = 32wt\%$ in weight. With these hydration levels, the number of water molecules is equal to ≈ 1.4 in both the solutions. For all the NS experiments flat aluminum holders were used and the sample thicknesses were chosen to provide a transmission of about 90%, thus allowing multiple scattering effects to be neglected. Following the same protocol described above, a solution with water content of $c_w = 45wt\%$ was also prepared and it was solely studied by WAXS.

A differential scanning calorimeter (DSC) TA Instrument Q2000 was used in standard mode to monitor the crystallization of the samples and to estimate their glass transition temperatures. The measurements were carried out

using hermetic Aluminium pans. A cooling-heating cycle between $T_g - 100$ K and $T_g + 30\,K$, at a rate of 10 K/min, was performed using Helium as transfer gas with a flow rate of 25 ml/min. The annealing time between cooling and heating runs was 2 min. No crystallization on cooling was observed and the glass transition temperatures were finally estimated from the heat flow curves as the onset point. The results are $T_g^{PVME/H_2O} = 208\,K$ and $T_g^{PVME/D_2O} = 211\,K$.

The **FOCUS Time-of-Flight** and the **IN16 backscattering spectrometers** were used to study the dynamics of the solutions. The measurements on $PVME/H_2O$ and $PVME/D_2O$ were carried out during the same experiments of the dry PVME sample. Therefore, the set up of the instruments used is that already described in detail in section 4.1. The analysis of the FOCUS data has been centered on the $PVME/D_2O$ solution to study how does water affect the microscopic dynamics of glassy PVME at $100\,K$. The $IN16$ measurements performed on $PVME/H_2O$ and $PVME/D_2O$ were carried out at the temperatures of 200, 225, 250, 270, 285 and $298\,K$.

The same experimental protocol used to measure the dry one and described in section 4.1 was followed in the **dielectric spectroscopy** and the **X-ray** experiments on the wet sample. The X-ray measurements were performed at the Material Physics Center (CFM) at room temperature ($\approx 300\,K$).

5.2 Experimental results and data analysis

Structure

WAXS spectra of dry PVME and PVME at the two different levels of hydration investigated at $300\,K$ are represented in Fig. 5.1. All the samples exhibit two peaks below $Q = 2\,\text{Å}^{-1}$, the first placed at $Q \approx 0.9\text{Å}^{-1}$ and the second at $Q \approx 1.5\,\text{Å}^{-1}$. A third peak is placed at $Q \approx 2.7\,\text{Å}^{-1}$. Increasing the hydration, the relative intensities of the first two peaks change, being

enhanced the second, while the broad third peak becomes more pronounced.
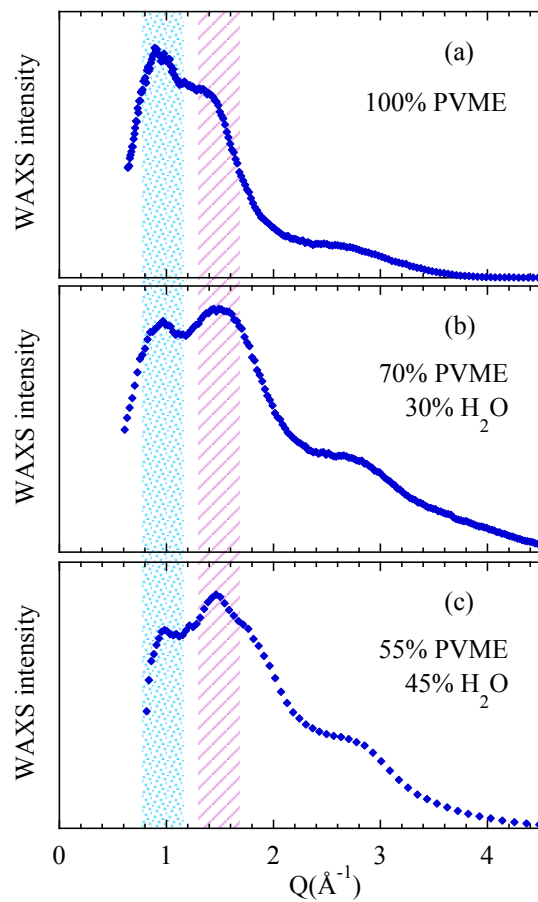

Figure 5.1: WAXS diffraction patterns of dry PVME (a) and PVME water solution with water content of $c_w = 30wt\%$ (b) and $c_w = 45wt\%$ (c) measured at room temperature. The shadowed regions correspond to the first, to the second and to the third peak.

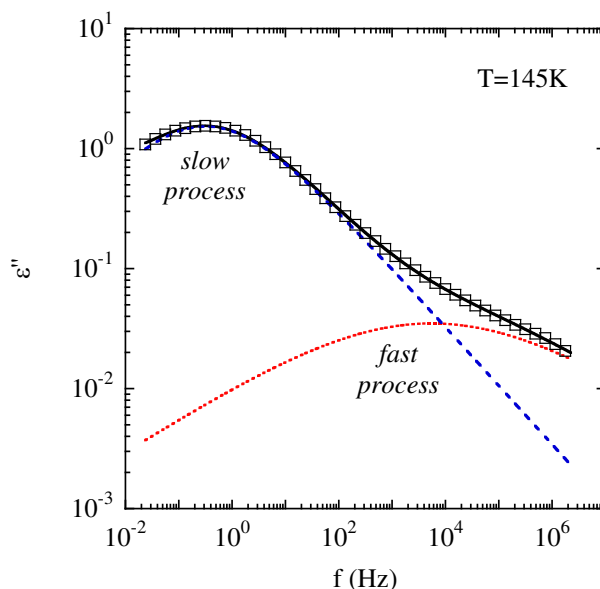**Calorimetry and Dielectric Spectroscopy measurements**

Figure 5.2: Dielectric loss spectrum of $PVME/H_2O$ solution at $T = 145\,K$. The fast (dotted line) and the slow (dashed line) process are drawn along with the total fit (solid line).

Dielectric spectroscopy measurements were performed on $PVME/H_2O$ in a range of temperature comprised between 115 and $255\,K$. In Fig 5.2 a low temperature spectrum $(T = 145\,K)$ is represented and two dynamic processes can be distinguished. The process which takes place at low frequency is called in this thesis the *slow process*, while the other one, called *fast process*, is active at higher frequency. In a previous work conducted by S. Cerveny and co-workers [114] the dielectric response of PVME aqueous solution was studied in the low frequency range of $10^{-2} - 10^6\,Hz$. By performing experiments on $PVME/H_2O$ and $PVME/D_2O$ samples, they found that the dielectric relaxation spectra of $PVME/H_2O$ reflects the water mobility. Based on such work, it is so assumed that both processes showed in Fig. 5.2 reveal the dynamics of water molecules. It is worthy of noting that in the work of Cerveny *et al.* [114] no high frequency or fast process was discussed.
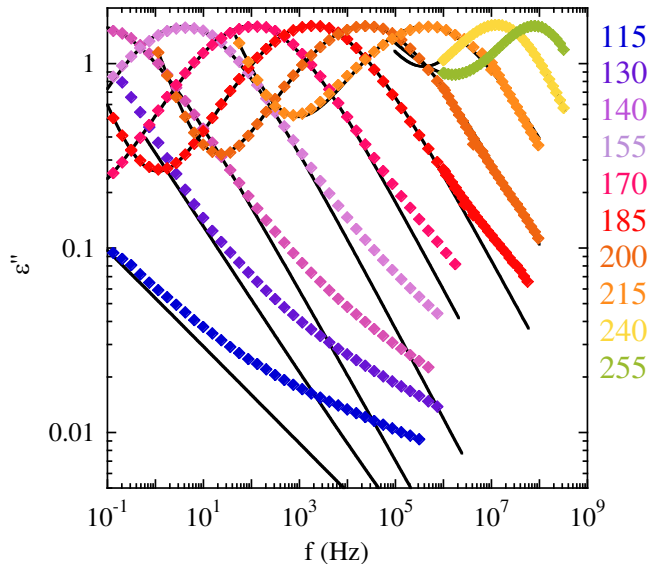
Figure 5.3: $PVME/H_2O$ dielectric loss spectra at the indicated temperature. The solid lines represent the fit of the slow process. The fast process cannot be resolved for $T > 155\,K$ because it is outside of the frequency window.

To fit the complex part of the spectra the following expression with two Cole-Cole (CC) functions [139] and a conductivity term was used:

$$\epsilon^*(\omega) = \epsilon'(\omega) - i\epsilon''(\omega) = -i\frac{\sigma_0}{\epsilon_0\omega} + \sum_{n=1}^{2}\frac{\Delta\epsilon_n}{[1 + (i\omega\tau_n)^{\alpha_n}]} \tag{5.1}$$

σ_0 is the dc conductivity, ϵ_0 the vacuum permittivity, $\Delta\epsilon_n$ is the dielectric strength, τ_n is the characteristic relaxation time and α_n is the symmetric broadening of the processes $n = 1, 2$. From the data analysis shown in Fig. 5.3 it can be deduced that at high temperatures it is not possible to resolve the high frequency process. In Fig. 5.4(b) the characteristic relaxation times of both processes are displayed (the ($\square$) symbols represent the characteristic relaxation times of the slow process, while ($\boxplus$) symbols those of the fast one). In Fig. 5.4(a) the derivative of the specific heat measured by calorimetry is shown.
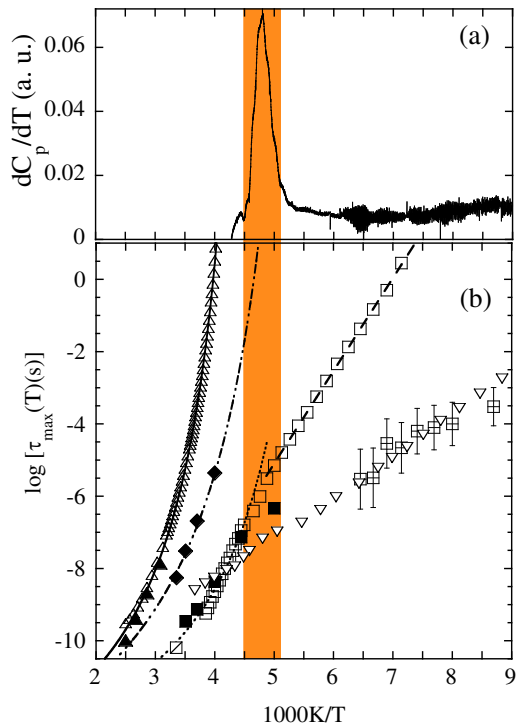
Figure 5.4: (a): Derivative of the specific heat as function of the inverse of the temperature. (b): Relaxation map of the PVME aqueous solution. The square symbols represent water dynamics, while the diamond symbols the wet PVME dynamics. Full symbols correspond to NS data at $Q = 1\text{Å}^{-1}$: the PVME ($\blacklozenge$) and the water ($\blacksquare$) component of the solution. Empty symbols correspond to DS measurements. The empty squares represent water characteristic relaxation times of the slow ($\square$) and fast ($\boxplus$) process. The dry PVME results are also displayed: NS characteristic relaxation times at $Q = 1\ \text{Å}^{-1}$ are represented as full triangles ($\blacktriangle$) [210], while empty triangles represent DS data: the α- ($\triangle$) and the β-process ($\triangledown$) are represented. Solid, dashed-dotted and dotted lines are the VF description of the dry, the wet PVME and the water. A dashed line shows the Arrhenius fit of the water slow process. The shadowed area indicates the region of the calorimetric glass transition of the solution.

Below the calorimetric glass transition of the sample, evidenced in Fig. 5.4 through a shaded area, the temperature dependence of the water dielectric relaxation times can be described by an Arrhenius equation $\tau(T) = \tau_0 exp(E/kT)$. The resulting values of the activation energy of the slow and the fast process are $E_0 = 0.51\,eV$ and $E_0 = 0.20\,eV$, with $log(\tau_0) = -17.8$ and $log(\tau_0) = -12.00$ respectively. As it can be seen from Fig. 5.4(b), the

temperature dependence of the relaxation times of the slow process crosses over from a non-Arrhenius behaviour above T_g to an Arrhenius one below T_g and the characteristic times of the fast process of water coincide within the uncertainties with those of the β-relaxation of the dry PVME sample.
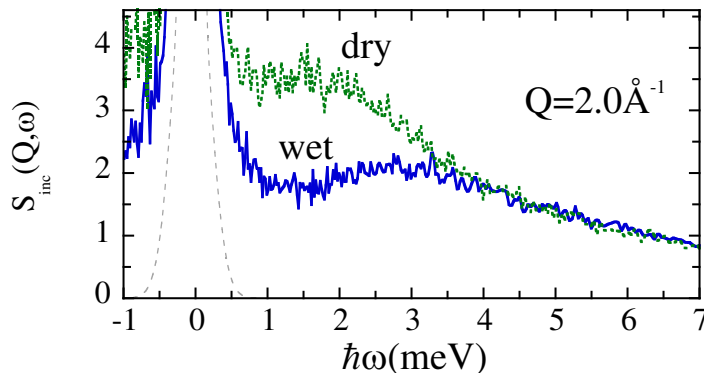
Time-of-Flight experiments

Figure 5.5: FOCUS spectra obtained at $100\,K$ at $Q = 2\text{Å}^{-1}$ for dry (green dotted line) and wet PVME (blue solid line). The resolution is represented as a dashed line.

Time-of-Flight experiments were used to study the behaviour of the PVME in presence of water well below the glass transition temperature. In Fig.5.5 FOCUS spectrum of $PVME/D_2O$ measured at $100\,K$ at the Q-value of 2Å^{-1} is represented along with the dry PVME spectrum. Both sets of data exhibit a clear Boson peak in the low frequency range, while for $\hbar\omega \gtrsim 4\,meV$ they closely match. In the low frequency range water significantly affects the microscopic dynamics of glassy PVME. Increasing the water content the intensity of the Boson peak decreases and its position shifts toward higher frequency, from $\approx 1.5\,meV$, the position of the maximum in dry PVME, to $\approx 3\,meV$, the position in wet PVME.
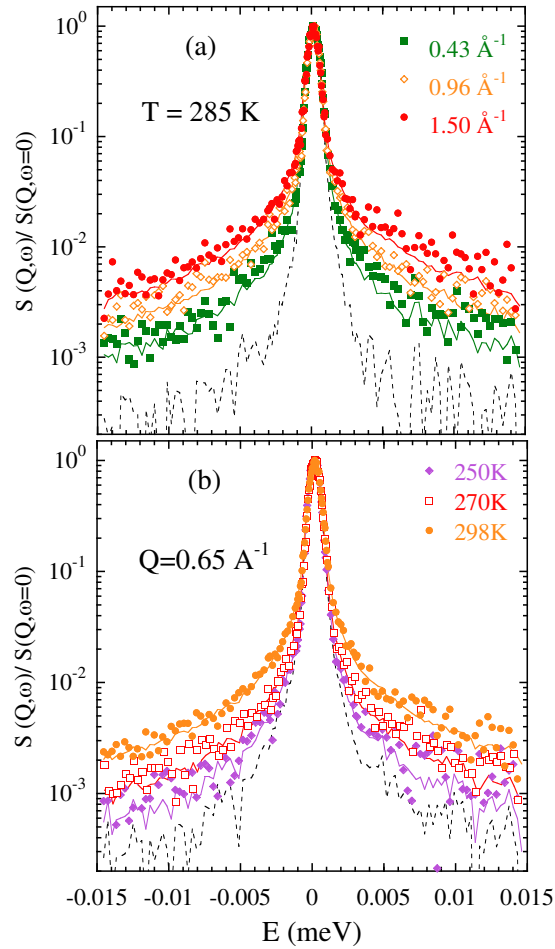
Backscattering experiments

Figure 5.6: $IN16$ spectra of $PVME/D_2O$ solution at (a) $T = 285\,K$ varying Q and (b) at fixed $Q = 0.65\text{Å}^{-1}$ varying T. The solid lines represent the KWW fitting curves ($\beta^{wetPVME} = 0.3$) and the instrumental resolution is depicted as dashed line.

$PVME/D_2O$ and $PVME/H_2O$ experiments on $IN16$ were performed in parallel and the same temperatures were investigated. The results on the deuterated solution were analyzed first, with the aim of complementing the data provided by FOCUS and understanding how does water af-

fect the polymer dynamics. Thereafter, these results have been used to extract information on the water dynamics in the $PVME/H_2O$ sample. In Figure 5.6 $PVME/D_2O$ spectra at different temperatures and Q-values are displayed. Since deuterated water was used, the spectra mainly show the PVME hydrogen dynamics. The general features are qualitatively similar to those shown by dry PVME at higher temperatures (Fig. 4.4 and Ref. [210]). They manifest as a quasielastic signal which broadens with increasing the Q-value and the temperature, suggesting diffusive-like dynamics of the PVME hydrogens in the solution. At $225\,K$ the spectra are elastic for the $IN16$ resolution. As it has been done for the dry sample, the data were analyzed in the frequency domain using Fourier tranform (FT) of the KWW functions, constructed by a superposition of Lorentzian functions (FT of single exponential decays) weighted by suitable distributions of characteristic times. The decay of the intermediate scattering functions was so fitted by means of the following KWW function

$$S_{inc}^{wetPVME}(Q,t) = A^{wetPVME}(Q,T)\,exp\Big[-\Big(\frac{t}{\tau_w^{wetPVME}(Q,T)}\Big)^{\beta^{wetPVME}}\Big]$$
$$(5.2)$$

In a preliminary data analysis $\beta^{wetPVME}$ was considered a free parameter and values between 0.4 and 0.2 were obtained. Fixing $\beta^{wetPVME} = 0.3$ a very good description of the data was achieved as it can be observed in Fig. 5.6. So $\beta^{wetPVME} = 0.3$ was fixed and the characteristic relaxation times $\tau_w^{wetPVME}(Q,T)$ were estimated. They are displayed in Fig. 5.7.
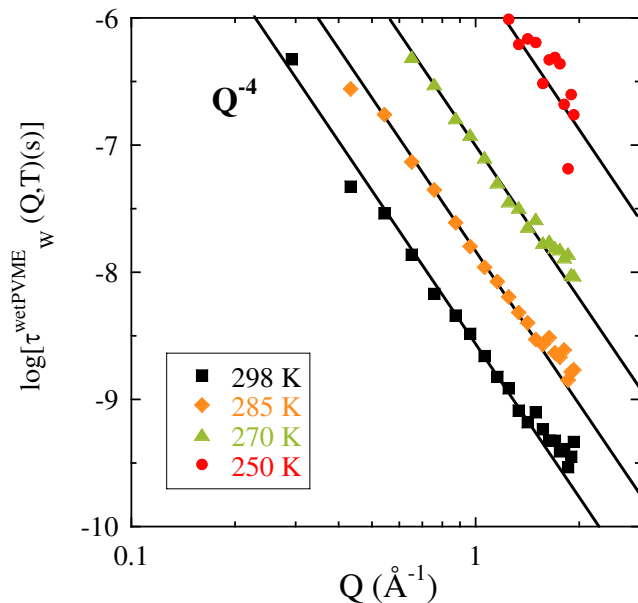
Figure 5.7: Characteristic relaxation times of PVME in $PVME/D_2O$ as estimated by BS experiments by means of KWW analysis with $\beta^{wetPVME} = 0.3$. The temperatures investigated are indicated in the legend and solid lines show the Q^{-4}-dependence.

In Figure 5.8 some representative $PVME/H_2O$ spectra are shown. They are broader than those of the $PVME/D_2O$ considered at the same Q- and T-values. Since water protons represent the unique additional component to the whole dynamics detected by neutrons in $PVME/H_2O$ with respect to $PVME/D_2O$, water hydrogen motion is faster than PVME hydrogen motion.
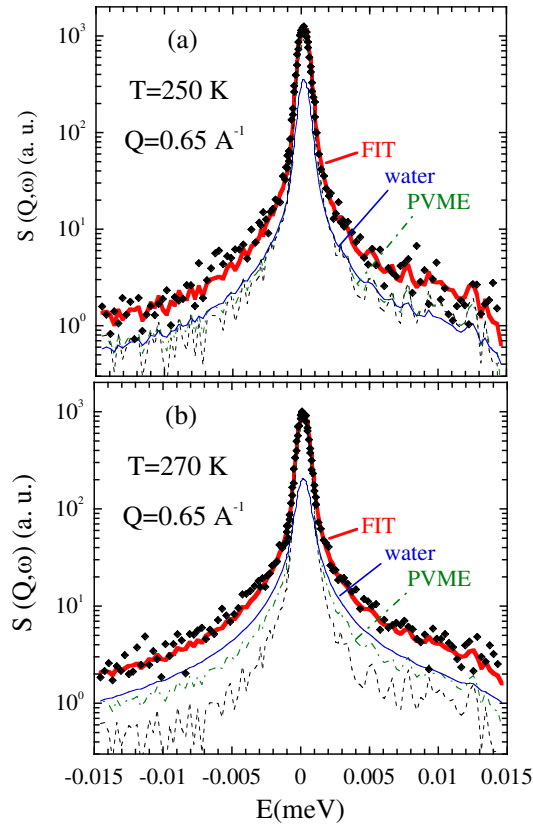
Figure 5.8: $IN16$ spectra of $PVME/H_2O$ solution at the Q-value of $Q = 0.65\text{Å}^{-1}$ and at (a) $T = 250\,K$ and (b) $T = 270\,K$. The thick solid lines represent the KWW fitting curves of total scattering function, the water component is represent as a thin blue solid line and the PVME component as green dashed-dotted line. The instrumental resolution is shown as a dashed line.

The measured intensity of $PVME/H_2O$ spectra can be considered as due to the contribution of water and PVME proton motions each weighted by the relative amount of the component in the solution. Therefore, the total intermediate scattering function can be expressed as

$$S_{inc}^{PVME/H_2O}(Q,t) = f_{H_2O}S_{inc}^{H_2O}(Q,t) + f_{PVME}S_{inc}^{wetPVME}(Q,t) \qquad (5.3)$$

in which the weights f_{H_2O} and f_{PVME} are determined by the relative cross-sections of the corresponding components:

$$f_{H_2O} = \frac{\sigma_{inc}^{H_2O}}{\sigma_{inc}^{PVME/H_2O}} = 0.31 \qquad (5.4)$$

$$f_{PVME} = \frac{\sigma_{inc}^{PVME}}{\sigma_{inc}^{PVME/H_2O}} = 0.69 \qquad (5.5)$$

Taking into account the procedure followed to analyse confined water in other systems [101, 113], KWW functions have been used to describe the incoherent scattering function of water protons. With the aim of reducing the number of free parameters, it has been assumed that the amplitudes parametrizing the fast dynamics of PVME and H_2O hydrogens were the same, so $A(Q,T)^{H_2O} = A(Q,T)^{wetPVME} = A(Q,T)$. Moreover, the values of $\beta^{wetPVME}$ and $\tau_w^{wetPVME}(Q,T)$ obtained from the analysis of $PVME/D_2O$ spectra were introduced as input data. The shape parameter β^{H_2O} was analyzed first. It did not show any clear and sistematic behaviour with temperature, so it was fixed at the temperature average value calculated for each Q. The characteristic relaxation times $\tau_w^{wetPVME}(Q,T)$ of water protons were subsequently obtained. They are displayed in Fig. 5.9(b) as a function of Q along with the values of $\beta^{H_2O}(Q)$, represented in Fig. 5.9(a).

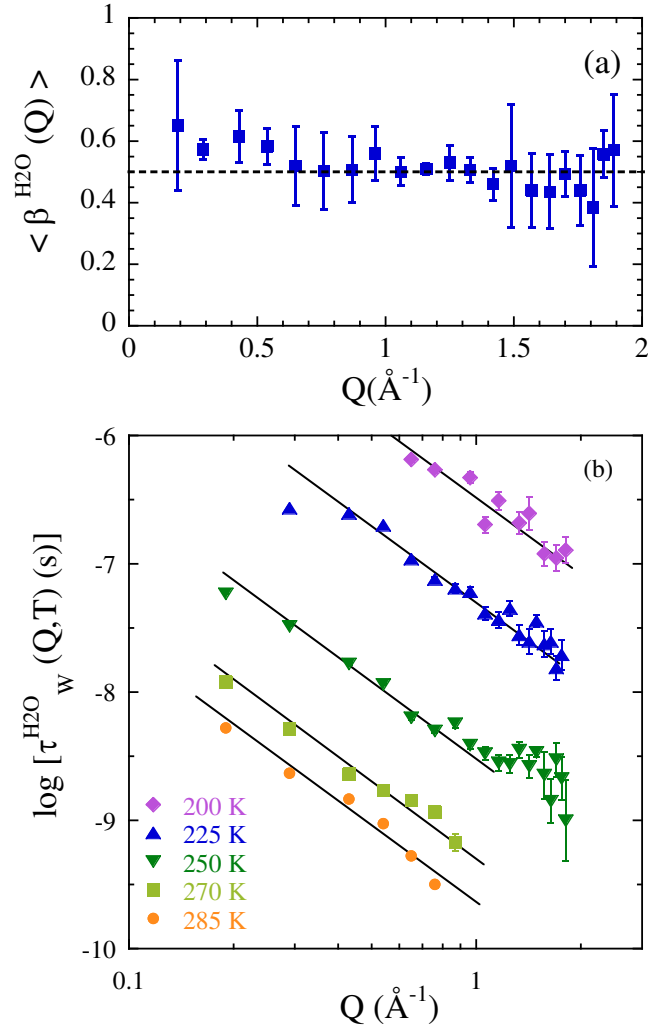Figure 5.9: Momentum transfer dependence of (a) the T-averaged shape parameter β^{H_2O} and of (b) the water characteristic relaxation times. Solid lines in (b) show the Q^{-2}-dependence.

5.3 Discussion

5.3.1 Structure of the sample at different hydration levels

The WAXS patterns of the samples at different level of hydration, shown in Fig. 5.1, exhibit a rise of the intensity of the second peak with increasing

the water content. According with the literature [169] and with the analysis of the simulated static structure factor carried out in section 4.4.1, in dry PVME the first peak placed at $\approx 0.9 \text{Å}^{-1}$ is mainly due to the correlations among main chain atoms, while the second peak, located at $\approx 1.5 \text{Å}^{-1}$, is related to those among side group atoms. Since water molecules can form hydrogen bonds with the oxygen atoms belonging to the side groups, it could be expected that they would be preferentially located close to these groups. Such hypothesis would be supported by the observed enhancement of the second peak. It seems that the presence of water does not appreciably affect the short-range order of PVME, since the correlations involving water atoms are characterized by the same associated lenghts of the side groups in dry PVME.

In addition to the hydrophilic oxygen atom, the side groups contain a hydrophobic methyl group. Increasing the water content some structural self-organization on the molecular scale can be expected and water could be located in hydrophilic or hydrophobic regions or in nano-sized bulk-like "pockets". In a MD simulation study performed by Tamai *et al.* [211] on hydrogels, it has been shown that in a PVME water sample with water content of $c_w = 50\%$ the 19% of the water molecules are found in hydrophilic regions, the 58% in hydrophobic regions and the 23% in bulk regions. Though low hydrated PVME was not studied by these authors, for the other hydrogels investigated with $c_w = 25\%$ the results point to very small amount of bulk-like water. Such scenario would be consistent with the data obtained by WAXS measurements represented in Fig. 5.1 and bulk-like water could be present in the sample with the highest water composition.

5.3.2 wet PVME dynamics in the glassy state

In the deep glassy state the Boson peak is exhibited in both dry and wet PVME as Fig. 5.5 shows. In the high frequency range the samples show almost identical spectra, while in the low frequency range the hydrated sample

exhibits, with respect to the dry one, a less pronounced Boson peak shifted from $1.5\,meV$ to $\approx 3\,meV$. Water thus mainly affects the low frequency vibrational modes of PVME. A similar hydration-induced shift of the Boson peak has already been observed in proteins through neutron scattering experiments and molecular dynamics simulation studies [212–216]. Nakagawa *et al.* suggested that the presence of water makes the protein energy landscape more rugged. At low temperature the protein motion is thus found to be trapped in a local minima causing the characteristic Boson peak frequency to shift to higher values [217]. On the other hand, Yamamuro *et al.* performed an inelastic NS study on different hydrogen-bonded molecular glasses, focusing the study on the effects of the hydrogen bonds on the Boson peak intensity and energy [218]. The authors found a general relation between the hydrogen bonds, the Boson peak energy and the Boson peak intensity: increasing the number of hydrogen bonds, the peak intensity decreases and its energy increases. In such context the shift of the Boson peak in the PVME/D_2O sample with respect to the dry one could be ascribed to the effect of the hydrogen bonds formed in presence of water. At low temperature the hydrogen bonds formed by water could deform the harmonic potential trapping the PVME motions in a local minima inducing the shift of the Boson peak to higher frequency with a decrease of its intensity.

This interpretation is supported by the estimation of the PVME mean square displacements. The FOCUS elastic signal can be described using the following expression

$$\frac{S_{elastic}(Q,T)}{S_{elastic}(Q,T \to 0)} = \exp\left(-\frac{\langle u^2 \rangle}{3}Q^2\right) \qquad (5.6)$$

The mean squared displacements at $100\,K$ can be so evaluated and they result to be $\langle u^2 \rangle^{dryPVME} = 0.066\text{Å}^2$ and $\langle u^2 \rangle^{wetPVME} = 0.043\text{Å}^2$. The amplitude of the vibrations in the glassy state is slightly reduced in presence of water. The results on the structural data suggested that water molecules are bonded to the side group oxygen and these bondings would induce a

decrease of the vibrational amplitudes of the PVME hydrogens by limiting the vibrational dynamics.

5.3.3 Water dynamics as revealed by NS

In Fig. 5.9(a) the values of β^{H_2O} used to analyse the QENS data of the $PVME/H_2O$ sample by means of KWW functions are displayed. It can be seen that in the Q-range investigated β^{H_2O} values are close to 0.5, always lower than 1, which is the expected value for homogeneous diffusion. The characteristic relaxation times shown in Fig. 5.9(b) follow the Q-dependence $\tau_w^{H_2O} \propto Q^{-2}$, which is the typical power law expected for simple diffusion. Since the shape of the spectra is not exponential, the displacements of water hydrogens are not distributed according to a Gaussian distribution.

The observed stretching of the water signal could be attributed to a distribution of mobilities. The KWW function can be expressed as a superposition of single exponential functions (see Eq. (1.5))

$$\varphi(t) = \exp\left[-\left(\frac{t}{\tau_w}\right)^\beta\right] = \int_{-\infty}^{+\infty} g(\log\tau)\exp\left(-\frac{t}{\tau}\right)d(\log\tau) \qquad (5.7)$$

in which the characteristic relaxation times τ are distributed according to given distribution functions $g(log\tau)$. In this context, Rajagopal *et al.* [219, 220] have proposed a distribution function giving rise to a KWW function characterized by a value of the shape parameter equal to 0.5. Such distribution function is defined as

$$g\left[\log\left(\frac{\tau}{\tau_w}\right)\right] = ln(10)\left(\frac{\tau}{4\pi\tau_w}\right)^{\frac{1}{2}}\exp\left(-\frac{\tau}{4\tau_w}\right) \qquad (5.8)$$
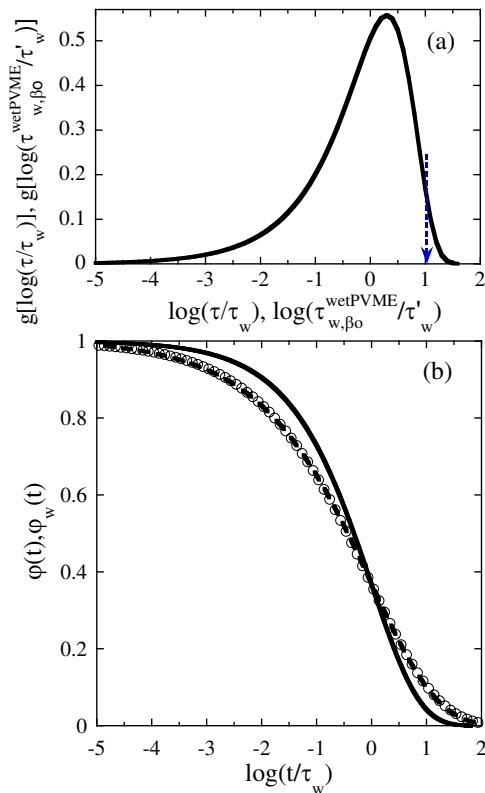
and it is shown in Fig 5.10(a).

Figure 5.10: (a) Distribution of characteristic times for single exponentials (Eq. (5.8)) and assumed to be extensible to stretched exponentials for the case of the PVME component (Eq. (5.13)). The superposition of single exponentials (Eq. (5.7)) gives rise to the KWW function with $\beta = 0.5$ shown as solid line in (b). The result of superimposing KWW functions with $\beta = 0.5$ according to Eq. 5.12 and characteristic times as in (a), Eq. (5.13), leads to the empty circles in (b) that can be described by a KWW function with $\beta = 0.36$ (dashed line). The relation between its characteristic time τ_w and the reference value of the distribution τ'_w is $\tau_w = 0.8\tau'_w$. The vertical arrow in (a) marks the corresponding value of $\tau_w^{dryPVME}$ at $298\,K$.

Since in a simple diffusion process the characteristic relaxation time can be related to the diffusion coefficient through the expression $\tau = D^{-1}Q^{-2}$, a distribution of mobilities $g(\log\tau)$ can be due to a distribution of diffusion coefficients $g(\log D^{-1})$. The KWW function given by the superposition of such distribution of diffusion coefficients $g(\log D^{-1})$ would be described using the stretched variable $X = Q^2 t$ which represents the conjugate variable (showing the same dimension) of the distributed magnitude D^{-1}. It results

$$\varphi(t) = \exp\left[-\left(\frac{t}{\tau_w}\right)^{\beta}\right] = \int_{-\infty}^{+\infty} g(\log D^{-1}) \exp\left(-\frac{Q^2 t}{D^{-1}}\right) d(\log D^{-1}) \quad (5.9)$$

In this case the resulting scattering function will thus read as $\exp[-(Q^2 t/D_w^{-1})^{\beta}]$ with the characteristic time defined as $\tau_w = D_w^{-1} Q^{-2}$, following the power law Q^{-2} expected for simple diffusion processes.

Hence, the Q-dependence of the characteristic relaxation times and of the shape parameter exhibited by the water molecules in the solution can be explained assuming a distribution of mobilities or of diffusion coefficients associated with slightly different local environments.

5.3.4 wet PVME dynamics in the α-relaxation regime as revealed by NS

In order to answer the question how does water affect the segmental dynamics of PVME in the solution, it is useful to summarize the results obtained on dry PVME studied well above T_g illustrated in the previous chapter.

NS data were analysed by means of KWW functions with $\beta^{dryPVME} = 0.5$ and the characteristic relaxation times were estimated. The results obtained by means of MD simulations were in an excellent agreement with those of NS. The characteristic relaxation times evaluated by means of both techniques exhibit a crossover from a Gaussian to a non-Gaussian behaviour at $Q^{\star}_{dryPVME} \approx 0.7 \text{Å}^{-1}$ as the master curve shows in Fig. 4.13. The excellent superposition evidenced by this curve can be factorized as follows

$$\tau_w = D_{eff}^{-1}(T) f(Q) \qquad (5.10)$$

For $Q \lesssim Q^{\star}_{dryPVME}$, $f(Q) \sim Q^{-x}$ with $x = 4 = 2/\beta^{dryPVME}$, which implies that $S_{inc}(Q,t)$ is a Gaussian function. In the higher Q-region deviations from such behaviour are found. They have been interpreted as due to

the non-Gaussian events taking place within the cage imposed by the neighboring atoms, which finally lead to the decaging involved in the structural relaxation. Dry PVME data are consistent with the Mode Coupling Theory (MCT) phenomenological predictions [210] and can be also well described in the framework of the anomalous jump diffusion model [178]. In the context of this model, the preferred jump distance ℓ_o is found to be 0.65Å.

The values obtained for the characteristic relaxation times of dry PVME by means of NS at $Q = 1\text{Å}^{-1}$ are represented in Fig. 5.4(b) as full triangles. They perfectly match those evaluated through DS experiments. This empirical overlap usually holds in glass-forming polymers [221, 222]. Both sets of data can be described by a Vogel-Fulcher (VF) expression

$$\tau = \tau_\infty \exp \frac{B}{T - T_o} \tag{5.11}$$

with $\tau_\infty^{dryPVME} = 1.16e^{-13}s$, $B^{dryPVME} = 1481.5\,K$ and $T_o^{dryPVME} = 202\,K$.

Concerning the $PVME/D_2O$ solution, the relaxation times of the PVME component evaluated from the NS experiments at $Q = 1\text{Å}^{-1}$ are represented in Fig. 5.4(b) as full diamonds. The dynamics of wet PVME is evidently faster than that of the dry sample. Since the resolution of the NS instrument impedes the study of the dynamics of the PVME aqueous solution at temperatures close to T_g and the DS measurements reveal only the dynamics of the water component, consideration of DSC results on the solution can be of utmost interest in this study. Being the polymer the majority component of the system, it can be assumed that the glass transition temperature, measured through DSC and represented in Fig. 5.4(a), reflects the freezing of PVME motions in the solution. The detected glass transition would so represent the *effective* glass transition of the PVME in the solution. It means that water leads to a shift of $36\,K$ in the value of the PVME glass transition temperature. This phenomenon is usually called *plasticization effect*.

Assuming that the same shift $(\Delta T_{shift} = 36\,K)$ is also induced in the Vogel temperature $T_o^{wetPVME}$

$$T_o^{wetPVME} = T_o^{dryPVME} - \Delta T_{shift} = 166\,K$$

while the other VF parameters remain unchanged, $\tau_o^{wetPVME} = \tau_o^{dryPVME}$ and $B^{wetPVME} = B^{dryPVME}$, the corresponding VF analysis can be performed and it gives a perfect description of the NS results of $PVME/D_2O$ at $Q = 1\,\mathring{A}^{-1}$ (see dashed-dotted curve in Fig. 5.4(b)). So, the effect of water on PVME dynamics can be described by a shift of the value of the glass transition temperature of the dry sample. An anologous effect is found in polymer blends, in which the vicinity of segments of chains of other kind, which display different intrinsic mobilities, induces a change in the glass-transition temperature of each component of the mixture [223, 224].

Besides the plasticization effect, the presence of water has two consequences on the dynamics of bulk PVME. (i) It causes a clear additional stretching of the spectral shape. The β parameter of PVME in the solution is found to be $\beta^{wetPVME} = 0.3$, while in the dry sample $\beta^{dryPVME} = 0.5$. (ii) Strong deviations from Gaussian behavior in the whole Q-range investigated are found. In wet PVME in fact a non-Gaussian behaviour is observed in the whole $IN16$ window, being $\beta^{wetPVME} = 0.3$ and the Q-dependence of the characteristic relaxation times $\tau_w^{wetPVME} \propto Q^{-4}$.

The stretching and the deviations from the Gaussian behaviour exhibited by water have been rationalized as due to the superposition of simple diffusive processes originated by the existence of heterogeneous environments in the solution. Fig. 5.10(a) shows the distribution function compatible to the water results. It can be assumed that such heterogeneous environments affect the dynamics of PVME in the solution yielding a distribution of mobilities also in the PVME component. It can be considered that the functional form of the PVME response in solution is a KWW function with a stretching parameter β_o, and the characteristic time $\tau_{w,\beta_o}^{wetPVME}$ varies from one region to the other in the sample according to the function $g(\log \tau_{w,\beta_o}^{wetPVME})$. This function would

132

have the same functional form as that observed for the characteristic time of the water component, already expressed in Eq.(5.8) and shown in Fig. 5.10(a):

$$g\left[\log\left(\frac{\tau_{w,\beta_o}^{wetPVME}}{\tau_w'}\right)\right] = ln(10)\left(\frac{\tau_{w,\beta_o}^{wetPVME}}{4\pi\tau_w'}\right)^{\frac{1}{2}}\exp\left(-\frac{\tau_{w,\beta_o}^{wetPVME}}{4\tau_w'}\right) \quad (5.12)$$

with τ_w' a reference timescale. The resulting response of PVME in the solution would then be given by:

$$\varphi_{w,\beta_o}^{wetPVME}(t) = \int_{-\infty}^{+\infty} g(\log\tau_{w,\beta_o}^{wetPVME})\exp\left[-\left(\frac{t}{\tau_{w,\beta_o}^{wetPVME}}\right)^{\beta_o}\right]d(\log\tau_{w,\beta_o}^{wetPVME})$$

$$(5.13)$$

In analogy with the case of water, in which it has been assumed "bulk"-like (simple diffusion) behaviour for the distributed functions, it is assumed the value of $\beta_o = 0.5$, which is equal to that of the dry PVME. The result of such superposition is shown in Fig. 5.10(b) as open circles and it is well described by a KWW function (dashed line) with a characteristic time $\tau_w = 0.8\tau_w'$ and a value of 0.36 for the stretching parameter. Such value is very close to that used for the parametrization of the wet PVME scattering function ($\beta^{wetPVME} = 0.3$). Therefore, a common heterogeneous environment can be considered as a possible origin of the stretching of both components of the solution. Such scenario is in fact consistent with a single funtional form of the distribution function and with the same underlying distribution of mobilities.

At this point it is interesting to compare the characteristic times of dry and wet PVME. To this end the corresponding master curves constructed with the same reference temperature of $298\,K$ have been calculated and they are represented in Fig. 5.11.
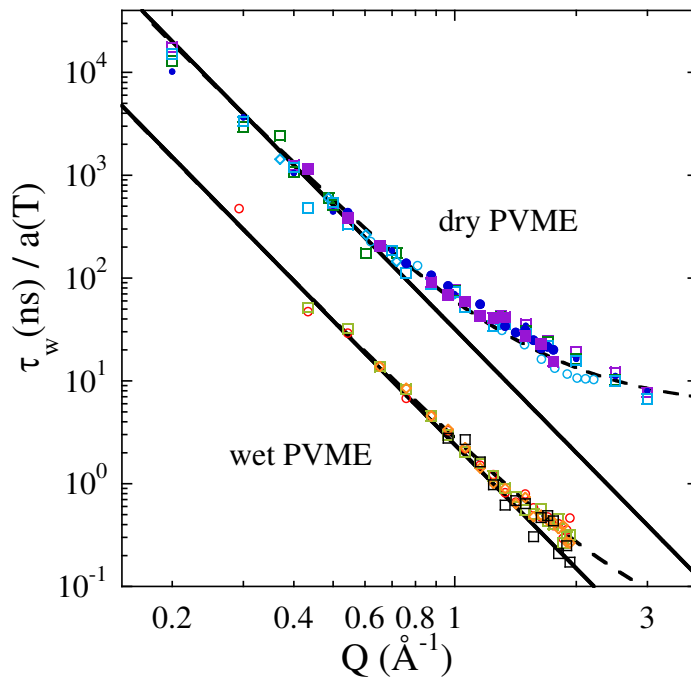
Figure 5.11: Mastercurves of dry [210] and wet PVME characteristic relaxation times obtained collapsing both sets of data to the reference temperature of $298\,K$. Different symbols correspond to different measurements and temperatures. Solid lines show the Q^{-4} dependence. $Q^{\star}_{dryPVME} = 0.7\text{Å}^{-1}$ and $Q^{\star}_{wetPVME} = 1.5\text{Å}^{-1}$.

In the range of Q below $Q^{\star}_{dryPVME} = 0.7\text{Å}^{-1}$ the master curves follow the same Q-power law of Q^{-4}. So $\tau_w^{wetPVME} = \alpha\tau_w^{dryPVME}$, with α given by the ratio between the VF equations describing wet and dry PVME results. At the reference temperature of $298\,K$ α takes the value of 0.075. In Fig. 5.10(a) the vertical arrow shows the corresponding position of the value of $\tau_w^{dryPVME}$ at this temperature: $\tau_w^{dryPVME}$ is about the longest time that can be found in the solution. It means that most of PVME hydrogens would move about 5 times faster in the solution than in bulk.

In this Q-regime, the phenomenology observed for wet PVME could be described assuming the scenario previously explained with the reference times of the distributions $\tau'_w = D'^{-1}_{eff}(T)f(Q)/0.8$, in which $D'_{eff} = D^{dryPVME}_{eff}/\alpha$ and $f(Q)$ is the same of the dry sample. The resulting $\tau_w^{wetPVME}$ would then

display the same dependence as $\tau_w^{dryPVME}$, that is proportional to Q^{-4}, which is in accordance to the experimental findings (Figs. 5.7 and 5.11).

In the Q range above $Q_{dryPVME}^{\star} = 0.7 \mathring{A}^{-1}$ the master curves do not follow the same Q-power law. The relaxation times of the wet PVME $\tau_w^{wetPVME}$ can be still factorized according to Eq. (5.10). If it is assumed the validity of the scenario of superposition of KWW functions, then a different Q-dependence of $f(Q)$ of the characteristic times of wet and dry PVME dynamics has to be considered. To explain this feature it can be invoked the description of both sets of data given by means of the anomalous jump diffusion model and represented in Fig. 5.11 as dashed lines. The characteristic jump distance of PVME in the solution results $\ell_o^{wetPVME} = 0.3\mathring{A}$, shorter than that found in the bulk polymer. The shortening of such distance due to the presence of water could rationalize the results obtained in the region above $Q_{dryPVME}^{\star}$. A more continuous-like diffusion of PVME atoms in the solution is deduced. Moreover, the decaging process would take place rather soon in the hydrated polymer. In fact, in the wet PVME it results that $\tau_w^{wetPVME}(Q_{wetPVME}^{\star}) \ll \tau_w^{dryPVME}(Q_{dryPVME}^{\star})$ with $Q_{wetPVME}^{\star} \approx 1.5\mathring{A}^{-1}$. The ratio $\tau_w^{dryPVME}(Q_{dryPVME}^{\star})/\tau_w^{wetPVME}(Q_{wetPVME}^{\star})$ is about 3 order of magnitude larger than that calculated in the Gaussian regime of dry PVME, $\tau_w^{dryPVME}(Q < Q_{dryPVME}^{\star})/\tau_w^{wetPVME}(Q < Q_{dryPVME}^{\star})$.

5.3.5   Fast process observed by dielectric spectroscopy (DS)

The characteristic times of the slow and the fast process of the water component as measured by dielectric spectroscopy are drawn in Fig. 5.4(b). The results corresponding to the water fast process, within the uncertainties, coincide with those of the β-relaxation of dry PVME, suggesting that the origin of the fast process of water molecules could be the motions involved in the secondary relaxation occuring in dry PVME. From the concentration dependence of the amplitude of the fast process it is deduced that water

molecules also participate in this relaxation. Therefore, the water fast process could be seen as due to the polymer localized motion involved in the β-relaxation of pure PVME and to some water dynamics directly induced by the polymer motions [225]. In a study performed by Urakawa *et al.* the molecular motion related to the β-relaxation of dry PVME has been assigned to the free rotational motions of the methyl groups around the O-C bond [225]. In accordance with those results, the scenario of water molecules reflecting the rotational motions of the dry PVME side groups supports the hypothesis that water is mainly placed near the PVME side groups, as already suggested by the diffraction data presented in this Ph. D. thesis and found in the simulations of Ref. [211].

5.3.6 Global discussion on the relaxation map of PVME water solution

In this section a global discussion on the results corresponding to both components of the solution and obtained by means of NS and DS techniques is given.

The characteristic relaxation times obtained through NS experiments at $Q = 1.0\,\text{Å}^{-1}$ for both components of the solution are shown in the Fig. 5.4(b). Water component, depicted as solid squares, exhibits faster dynamics than the PVME one, depicted as solid diamonds. Decreasing the temperature, the difference between these relaxation times increases, implying an enhancement of the dynamic asymmetry of the system on cooling. In the temperature range of $T \lesssim 225\,K$, the PVME component is expected to be frozen with respect to the water component.

In the temperature range of $T \geq 225\,K$ the NS characteristic relaxation times of water at $Q = 1.0\,\text{Å}^{-1}$ match the dielectric spectroscopy results, supporting the interpretation that DS experiments performed on $PVME/H_2O$ solution reveal water motions [114]. In this high temperature range the joint set of data of NS, DS and Microwaves of water in the solution can

be described by a VF function with $\tau_\infty^{H_2O} = 1.5e^{-13}\,s$, $B^{H_2O} = 897\,K$ and $T_o^{H_2O} = 158\,K$. This description, depicted in Fig. 5.4(b) with a dotted line, suggests a cooperative-like motions of water molecules.

In the temperature range of $T < 225\,K$, NS and DS water relaxation times begin to follow a weaker temperature dependence. In particular, NS results exhibit the characteristic deviation attributed in other NS studies performed on confined water to the strong-fragile transition, a phenomenon discussed in section 1.2.3. Such deviation has also been explained as a general feature of dynamically asymmetric systems studied in a range of temperatures close to the glass transition of the majority component [115]. By analogy with polymer blends, the origin of the crossover found at $\approx 225\,K$ in PVME aqueous can be interpreted as the onset of confinement of water by the freezing of the polymer matrix [223, 224, 226]. In these systems a strong dynamic asymmetry is developed at low temperature and the glass transition temperature is mainly due to the effective glass transition of the majority component.

In addition, the water characteristic relaxation time evaluated by means of NS at $200\,K$ (full square symbols) is faster than that obtained by DS measurements (empty square symbols) and it seems to approach the fast process, which cannot be resolved above $145\,K$ (see Fig. 5.2). Since the water fast process characteristic times at high temperature coincide with the β-process of dry PVME, it can be assumed that in the low temperature regime these data can describe those of the fast process of water. It results that at $200\,K$ the NS water relaxation time is slower than that of the dry PVME β-process. It can be thus concluded that at $200\,K$ NS reveals a water motion which, though it could be attributed to a combination of the slow and the fast DS processes, would be apparently dominated by the fast one. In this context, the deviations from the VF description of water dynamics could be interpreted as the strong coupling of water motions with the PVME processes involved in the β-relaxation.

It is worthy of remarking that some features reported for miscible poly-

mer blends, as the broadening of the responses with respect to those of the homopolymers and the dynamic heterogeneity of the different components, are also displayed in the PVME aqueous solution. In polymer blends the additional stretching is attributed to concentration fluctuations [227, 228]. In the particular case of PVME/polystyrene blend studied by Cendoya *et al.* the authors explained the dynamic heterogeneities by assuming that the PVME segmental dynamics contributes to the response of the blend through a superposition of different processes [228]. These processes were described by KWW functions with the same spectral shape as those of bulk PVME, but different characteristic relaxation times distributed due to the concentration fluctuations. This scenario is analogous to that of PVME aqueous solution here presented. Moreover, results on strong dynamically asymmetric systems report confinement effects for the fast component which resemble those observed for water in PVME water solution, as Arrhenius-like temperature dependence of the characteristic times in the low-T region, where the slow component is frozen [226].

Finally, the shift in the T_o value of the wet sample with respect to the dry one implies a change in the polymer fragility defined as

$$ m = \frac{d(log_{10}\tau)}{d\left(T_g/T\right)} \tag{5.14} $$

Since the value of the fragility decreases from $m^{dryPVME} = 85$ to $m^{wetPVME} = 72$, according to the Angell's classification the polymer becomes stronger in the solution. Such observation is consistent with a significant amount of hydrogen-bonds in the solution.

CHAPTER 6

CONCLUSIONS

This Ph. D. thesis has been focused on the structure and the dynamics of dry PVME and its concentrated aqueous solution. The joint use of NS, X-ray experiements and fully atomistic molecular dynamics simulation has represented a powerful tool to unveil the characteristics of the samples. DS and calorimetry supports have also been useful for a consistent interpretation of the results. First the dry polymer and thereafter the PVME aqueous solution with water content of $c_w = 30\%$ have been deeply investigated.

dry PVME

X-ray and NS experiments were performed on fully protonated samples. From the former measurements the structure of the sample was studied, while through the latter the single-particle motion of PVME hydrogens was investigated. In parallel fully atomistic molecular dynamics simulations were carried out. Once they have been validated by contrasting simulated results against the experimental ones, the simulations have been exploited. The analysis of the experimental and the simulated data have led to the following results:

- The structure of the PVME was unveiled. The total static structure

139

factor measured at room temperature exhibits three peaks placed at $Q \approx 0.9\mathring{A}^{-1}$, $Q \approx 1.5\mathring{A}^{-1}$ and $Q \approx 2.7\mathring{A}^{-1}$ respectively. Through the analysis of the simulated partial static structure factors it has been shown that the main peak is mainly due to the correlations among the main chains, while the second peak to the correlations among the side groups. The third peak is temperature independent and is due to both types of correlations. In addition an anticorrelation, interpreted as the tendency of local separation of the side group and the main chains, has been observed in correspondence of the first peak. Interestingly, the T-dependence of the first peak is dictated by that of the cross-correlations.

- Through the study of the single particle motion of fully protonated PVME anomalous diffusive motion has been identified in the α-relaxation regime. A crossover from a Gaussian to a non-Gaussian behaviour in the Q-dependence of the α-relaxation times has been observed. It takes place at the value of $Q = 0.7\mathring{A}^{-1}$. It has been interpreted that one possible origin for such deviation is related to the chemical heterogeneity of the sample. The methyl group hydrogens indeed participate simultaneously in the methyl group rotation and in the whole chain motion affecting the total scattering function. Such fast rotational motion is a source of deviations from the Gaussian behaviour. Moreover, from the analysis of the main chain hydrogen motion, evidences of the cage effects have been observed and they have been interpreted as another inherent source for the deviation from the Gaussian behaviour.

- The deviations from the Gaussian behaviour were studied in the reciprocal space by analyzing the intermediate scattering function of the main chain hydrogens. Through the direct comparison between the simulated function and the Q^2-expansion of the scattering function,

it is shown that at high Q-values the correction including the non-Gaussian parameter $\alpha_2(t)$ is insufficient to describe the pattern of the simulated intermediate scattering function.

- The self-correlation functions of the PVME atoms were analyzed within the framework of the MCT and consistent results were obtained. The high value of the γ and λ parameters are close to those found for other real polymers. Such result has been interpreted as a consequence of the competition between two distinct mechanisms for dynamics arrest constituted by the packing effects of intermolecular character and by the barriers for conformational changes of intramolecular character specific of polymer systems.

- The crossover from Gaussian to non-Gaussian behaviour in the Q-dependence of the α-relaxation times has been also analyzed by means of the anomalous jump diffusion model. A value $\ell_0^{cH} = 0.45\text{Å}$ is found for the most probable jump distances for the main chain hydrogens, while a larger value ($\ell_0^{dryPVME} = 0.65\text{Å}$) is found if all the hydrogens are considered.

aqueous PVME solution

The structure of PVME aqueous solution at two different levels of hydration was investigated by means of X-ray experiments. Concerning the dynamics, NS measurements have provided information on the single particle motion of the hydrogens of both components of the solution. In order to do this it has been made use of the isotopic labelling technique (H/D). Dielectric spectroscopy and DSC experiments have provided further insight to get a fully picture of the dynamics in the components. The following conclusions have been yielded:

- The correlations involving water molecules are characterized by the same associated lengths of the side groups of dry PVME, suggesting

141

that the short-range order of the polymer is not affected by the presence of water. In particular, the position of the first structure factor peak is not appreciably affected by the presence of water. It seems to be probable the existence of bulk-like water correlations, implying the existence of aggregates of water molecules.

- For both components of the solution, water and PVME, NS results evidence a stretching of the scattering functions ($\beta^{H_2O} \approx 0.5$ and $\beta^{wetPVME} = 0.3$) and a non-Gaussian behaviour of the characteristic relaxation times in the whole Q-range investigated. These results have been interpreted with a distribution of mobilities due to structural heterogeneities of the sample like water clusters or aggregates.

- Strong dynamic asymmetry which increases on cooling has been observed in all the Q-range investigated by means of NS experiments.

- In the temperature range $T > 225\,K$, the water characteristic relaxation times obtained by means of NS at $Q = 1\text{Å}^{-1}$ very much coincide with those evaluated by means of DS, supporting that DS detects water dynamics in the solution. Both NS and DS data can be described by a VF function with $\tau_\infty^{H_2O} = 1.5e^{-13}\,s$, $B^{H_2O} = 897\,K$ and $T_o^{H_2O} = 158\,K$ implying cooperative-like motions of water molecules.

- At the temperature of $T \approx 225\,K$ water characteristic relaxation times evaluated by means of DS and NS exhibit a crossover toward a weaker T-dependence. The fragile-to-strong transition of water in confined systems has been considered as the origin of this kind of deviation by some authors [101], though it has been critized by others [98, 105–107]. From DS studies, such crossover has been alternativelly interpreted as a general feature of dynamically asymmetric systems studied in the temperature range close to the glass transition of the majority component [115]. In this Ph. D. thesis it is suggested that such crossover in

the aqueous PVME solution can be due to the onset of the confined dynamics of water by the freezing of the polymer matrix.

- In the low temperature range two processes are detected by dielectric spectroscopy measurements: the *slow* one takes place at low frequency, while the *fast* one at higher frequency. The water relaxation times corresponding to the fast process coincide within the uncertainties with those of the β-process of dry PVME. In literature the PVME secondary process has been ascribed to the rotation motions of the methyl group atoms around the O-C bonds [225]. According to literature and to WAXS results, which hint that water molecules are placed close to the PVME side groups atoms, it has been so suggested that the water fast process is due to the polymer motion involved in the β-process of pure PVME and to some water dynamics induced by such motions.

- With the aid of dielectric spectroscopy results the motion of water detected by NS at the lowest temperature of $200\,K$ is suggested to be due to the combination of the fast and the slow processes occurring in water and revealed by DS. The deviation exhibited at low temperature of the characteristic relaxation times from the high temperature behaviour could be so considered as the participation of the water molecules in the fast motions coupled with PVME secondary relaxation.

- Concerning the effect of water on the microscopic dynamics of glassy PVME, it has been observed that the Boson peak, detected through NS experiments performed on $PVME/D_2O$ at $100\,K$, is less intense with respect to that of the dry sample and the position is shifted toward higher frequency. In this temperature range, it is expected that the hydrogen bonds would limit the dynamics of the wet polymer provoking the shift of the Boson peak frequency and a decrease of the vibrational amplitude of the PVME hydrogen motion. This hypothesis is confirmed by the values found for the mean squared displacements of the different

samples.

- In the high temperature range a plasticization effect is observed in the polymer dynamics due to the presence of water. The value of the PVME glass transition is shifted of $36\,K$ and, according to the Angell's classification, the polymer becomes stronger in the solution.

- The overall phenomenology found in PVME water solution strongly resembles that observed for polymer blends with different glass-transition temperature for the two homopolymers. This similarity supports the interpretation of some results in this solution as consequence of the dynamic asymmetry in the system.

BIBLIOGRAPHY

[1] L. H. Sperling, *Introduction to physical polymer science*, 2nd ed., John Wiley & Sons, Inc.,, 1992.

[2] G. Strobl, *The Physics of Polymer: Concepts for Understanding their Structures and Behavior*, 2nd ed., Springer-Verlag, Berlin Heidelberg New York, 1997.

[3] D. I. Bower, *Introduction to Polymer Physics*, Cambridge University Press, Cambridge, 2002.

[4] C. A. Angell, Science **267**, 1924 (1995).

[5] P. G. Debenedetti and F. H. Stilliger, Nature **410**, 259 (2001).

[6] M. Doi and S. F. Edwards, *The theory of polymer dynamics*, Oxford University Press, England, 1986.

[7] P. G. D. Gennes, *Scaling concepts in polymer physics*, Cornell University Press, New York, 1979.

[8] D. Richter, M. Monkenbusch, A. Arbe, and J. Colmenero, *Neutron Spin Echo in Polymer Systems*, Advances in Polymer Science, Vol. 174. Springer Verlag, 2005.

[9] J. Colmenero, A. J. Moreno, and A. Alegría, Prog. Polym. Sci. **30**, 1147 (2005).

[10] H. Vogel, Phys. Z **22**, 645 (1921).

[11] G. S. Fulcher, J. Am. Chem. Soc. **8**, 339; 789 (1925).

[12] P. E. Rouse, J. Chem. Phys. **21**, 1272 (1953).

[13] P. G. D. Gennes, J. Phys. **42**, 735 (1981).

[14] P. W. Anderson, Science **267**, 1615 (1995).

[15] J. C. Dyre, Rev. Mod. Phys. **78**, 953 (2006).

[16] C. A. Angell, J. Non-Cryst. Solids **102**, 205 (1988).

[17] M. D. Ediger, C. A. Angell, and S. R. Nagel, J. Phys. Chem. **100**, 13200 (1996).

[18] F. Kohlrausch, Pogg. Ann. Phys. **119**, 352 (1863).

[19] G. Williams and D. C. Watts, Trans. Faraday Soc. **66**, 80 (1970).

[20] A. Arbe, J. Colmenero, M. Monkenbusch, and D. Richter, Phys. Rev. Lett. **81**, 590 (1988).

[21] J. Baschnagel and F. Varnik, J. Phys.: Condensed Matter **17**, R851 (2005).

[22] A. Heuer and K. Okun, J. Chem. Phys. **106**, 6176 (1997).

[23] R. Schilling *Condensed Matter,* arXiv:cond-mat/0305565v1.

[24] P. G. Debenedetti, *Metastable Liquids. Concepts and Principles*, Princeton University Press, Princeton, 1996.

[25] E. Donth, *The Glass Transition. Relaxation Dynamics in Liquids and Disordered Materials*, Springer-Verlag, Berlin Heidelberg New York, 2001.

[26] J. Jäckle, Rep. Prog. Phys. **49**, 171 (1986).

[27] U. Bengtzelius, W. Götze, and A. Sjölander, J. Phys. C: Solid State Phys. **17**, 5915 (1984).

[28] K. Kawasaki, Phys. Rev. **150**, 291 (1966).

[29] W. Kob, *Condensed Matter,* arXiv:cond-mat/0212344v1.

[30] W. Götze, *Liquids, Freezing and Glass Transition*, edited by J. P. Hansen, D. Levesque and J. Zinn-Justin, Amsterdam, 1991.

[31] W. Götze and L. Sjögren, Rep. Prog. Phys. **55**, 241 (1992).

[32] W. Götze, J. Phys.: Condens. Matter **11**, A1 (1999).

[33] W. Götze, *Complex Dynamics of Glass-Forming Liquids. A mode Coupling Theory*, Oxford University, New York, 2009.

[34] P. S. Das, Rev. Mod. Phys. **76**, 785 (2004).

[35] D. R. Reichman and P. Charbonneau, J. Stat. Mech. **5**, P05013 (2005).

[36] J.-P. Hansen and I. R. McDonald, *Theory of Simple Liquids*, Academic Press, London, 2006.

[37] M. Bernabei, A. Moreno, and J. Colmenero, J. Chem. Phys. **131**, 204502 (2009).

[38] U. Balucani and M. Zoppi, *Dynamics of the Liquid State*, University Press, Oxford, 1994.

[39] F. Sciortino and W. Kob, Phys. Rev. Lett. **86**, 648 (2001).

[40] M. Fuchs, W. Götze, and M. R. Mayr, Phys. Rev. E **58**, 3384 (1998).

[41] W. Götze and L. Sjögren, Phys. Rev. A **43**, 5442 (1991).

[42] G. Foffi, W. Götze, F. Sciortino, P. Tartaglia, and T. Voigtmann, Phys. Rev. E **69**, 011505 (2004).

[43] J.-L. Barrat and A. Latz, J. Phys.: Condens. Matter **2**, 4289 (1990).

[44] M. Nauroth and W. Kob, Phys. Rev. E **55**, 657 (1997).

[45] T. Franosch, M. Fuchs, W. Götze, M. R. Mayr, and A. P. Singh, Phys. Rev. E **55**, 7153 (1997).

[46] S. H. Chong, W. Götze, and A. P. Singh, Phys. Rev. E **63**, 011206 (2001).

[47] R. Schilling and T. Scheidsteger, Phys. Rev. E **56**, 2932 (1997).

[48] L. Fabbian et al., Phys. Rev. E **62**, 2388 (2000).

[49] A. Tölle, H. Schober, J. Wuttke, and F. Fujara, Phys. Rev. E **56**, 809 (1997).

[50] D. Richter, B. Frick, and B. Farago, Phys. Rev. Lett. **61**, 2465 (1988).

[51] A. V. Zon and S. W. D. Leeuw, Phys. Rev. E **60**, 6942 (1999).

[52] J. Colmenero, A. Narros, F. Alvarez, A. Arbe, and A. J. Moreno, J. Phys.: Condens. Matter **19**, 205127 (2007).

[53] W. Paul, D. Bedrov, and G. D. Smith, Phys. Rev. E **74**, 021501 (2006).

[54] W. Götze, Z. Phys. B **60**, 195 (1985).

[55] W. Kob and H. C. Andersen, Phys. Rev. E **51**, 4426 (1995).

[56] R. Schmitz, J. W. Dufty, and P. De, Phys. Rev. Lett. **71**, 2066 (1993).

[57] W. Kob and H. C. Andersen, Phys. Rev. E **52**, 4134 (1995).

[58] J. Horbach and W. Kob, Phys. Rev. B **60**, 3168 (1999).

[59] F. Franks, *Water: a matrix of life.*, Cambridge: The Royal Society of Chemistry, 2nd edn, 2000.

[60] D. Eisenberg and W. Kauzmann, *The Structure and Properties of Water*, 1st edn 1969, Oxford University Press: Clarendon, 2006.

[61] F. H. Stillinger, Science **209**, 451 (1980).

[62] C. Lobban, J. L. Finney, and W. F. Kuhs, Nature **391**, 268 (1998).

[63] C. Huang et al., Proc. Nat. Acad. Sci. **106**, 15214 (2009).

[64] C. A. Angell, Nature **331**, 206 (1988).

[65] C. A. Angell, Ann. Rev. Phys. Chem. **34**, 593 (1983).

[66] C. A. Angell, *Water, a comprehensive treatise*, vol 7, Felix Franks, New York, 1982.

[67] P. G. Debenedetti, J. Phys.: Condens. Matter **15**, R1669 (2003).

[68] P. Kumar, G. Franzese, and H. E. Stanley, J. Phys.: Condens. Matter **20**, 244144 (2008).

[69] O. Mishima and H. E. Stanley, Nature **396**, 329 (1998).

[70] R. J. Speedy and C. A. Angell, J. Chem. Phys. **65**, 851 (1976).

[71] P. G. Debenedetti, *Metastable Liquids. Concepts and Principles*, Princeton University Press, 1996.

[72] G. P. Johari, A. Hallbrucker, and E. Mayer, Nature **330**, 552 (1987).

[73] V. Velikov, S. Borick, and C. A. Angell, Science **294**, 2335 (2001).

[74] C. A. Angell, Chem. Rev. **102**, 2627 (2002).

[75] Y. Yue and C. A. Angell, Nature **427**, 716 (2004).

[76] N. Giovambattista, C. A. Angell, F. Sciortino, and H. E. Stanley, Phys. Rev. Lett. **93**, 047801 (2004).

[77] G. P. Johari, Journal of Chemical Physics **116**, 8067 (2002).

[78] S. Sastry, Nature **398**, 469 (1999).

[79] S.-H. Chen, J. Teixeira, and R. Nicklow, Phys. Rev. A **26**, 3477 (1982).

[80] J. Teixeira, M.-C. Bellissent-Funel, S.-H. Chen, and A. J. Dianoux, Phys. Rev. A **31**, 1913 (1985).

[81] A. Rahman and F. H. Stillinger, Phys. Rev. A **10**, 368 (1974).

[82] J. Teixeira, M. C. Bellissent-Funel, S.-H. Chen, and B. Dorner, Phys. Rev. Lett. **54**, 2681 (1985).

[83] G. Ruocco and F. Sette, J. Phys.: Condens. Matter **11**, R259 (1999).

[84] P. Jenniskens and D. F. Blake, Science **265**, 753 (1994).

[85] P. Jenniskens, S. F. Banham, D. F. Blake, and M. R. S. McCoustra, J. Chem. Phys. **107**, 1232 (1997).

[86] E. F. Burton and W. F. Oliver, Proc. R. Soc. A **153**, 166 (1935).

[87] G. P. Johari, A. Hallbrucker, and E. Mayer, Science **273**, 90 (1996).

[88] O. Mishima, L. D. Calvert, and E. Whalley, Nature **310**, 393 (1984).

[89] O. Mishima, L. D. Calvert, and E. Whalley, Nature **314**, 76 (1985).

[90] T. Loerting, C. Salzmann, I. Kohl, E. Mayer, and A. Hallbrucker, Phy. Chem. Chem. Phys. **3**, 5355 (2001).

[91] C. A. Angell, Science **319**, 582 (2008).

[92] P. H. Poole, F. Sciortino, U. Essman, and H. E. Stanley, Nature **360**, 324 (1992).

[93] S. Sastry, P. G. Debenedetti, F. Sciortino, and H. E. Stanley, Phys. Rev. E **53**, 6144 (1996).

[94] F. Mallamace et al., J. Chem. Phys. **124**, 161102 (2006).

[95] R. Bergman and J. Swenson, Nature **403**, 283 (2000).

[96] S. Cerveny, G. Schwartz, R. Bergman, and J. Swenson, Phys. Rev. Lett. **93**, 245702 (2004).

[97] S.-H. Chen et al., Procl. Natl. Acad. Sci. **103**, 9012 (2006).

[98] M. Vogel, Phys. Rev. Lett. **101**, 225701 (2008).

[99] H. D. Middendorf, Physica B **226**, 113 (1996).

[100] K. Ito, C. T. moynihan, and C. A. Angell, Nature **398**, 492 (1999).

[101] S. H. Chen et al., J. Chem. Phys. **125**, 171103 (2006).

[102] L. Xu et al., Procl. Natl. Acad. Sci. **102**, 16558 (2005).

[103] P. Kumar et al., Phys. Rev. Lett. **97**, 177802 (2006).

[104] S. H. Chen et al., Proc. Nat. Acad. Sci. **103**, 12974 (2006).

[105] J. Swenson, H. Jansson, and R. Bergman, Phys. Rev. Lett. **96**, 247802 (2006).

[106] S. Pawlus, S. Khodadadi, and A. P. Sokolov, Phys. Rev. Lett. **100**, 108103 (2008).

[107] W. Doster et al., Phys. Rev. Lett. **104**, 098101 (2010).

[108] J. Swenson, H. Jansson, J. Hedström, and R. Bergman, J. Phys.:Condens. Matter **19**, 205109 (2007).

[109] N. Nandi, K. Bhattacharyya, and B. Bagchi, Chem. Rev. **100**, 2013 (2000).

[110] S. K. Pal and A. H. Zweil, Chem. Rev. **104**, 2099 (2004).

[111] G. A. Jeffrey and W. Saenger, *Hydrogen bonding in biological systems*, Springer-Verlag:Berlin, 1991.

[112] R. G. Bryant, Ann. Rev. Biophys. Biomol. Struct. **25**, 29 (1996).

[113] J. Swenson, H. Jansson, W. S. Howells, and S. Longeville, J. Chem. Phys. **122**, 084505 (2005).

[114] S. Cerveny, J. Colmenero, and A. Alegría, Macromolecules **38**, 7056 (2005).

[115] S. Cerveny, A. Alegría, and J. Colmenero, Phys. Rev. E **77**, 031803 (2008).

[116] D. L. Price and K. Sköld, *Methods of Experimental Physics: Neutron Scattering*, Academic Press, Orlando, 1986.

[117] S. W. Lovesey, *Theory of Neutron Scattering from Condensed Matter. International series of monographs on physics*, Clarendon Press, Oxford, 1984.

[118] J. S. Higgins and H. C. Benoît, *Polymers and Neutron Scattering*, Clarendon Press, Oxford, 1994.

[119] J. L. Squires, *Introduction to the Theory of Thermal Neutron Scattering*, Dover Publications Inc., New York, 1996.

[120] M. Bée, *Quasielastic Neutron Scattering*, Adam Hilger, Bristol and Philadelphia, 1988.

[121] A. Dianoux and G. Lander, *Neutron data booklet*, Institute Laue-Langevin, 2002.

[122] W. Wagner, J. Mesot, P. Allenspach, G. Kuehne, and H. M. Rønnow, Physica B **385**, 968 (2006).

[123] G. S. Bauer, Y. Dai, and W. Wagner, J. Phys. IV France **12**, Pr8 (2002).

[124] Paul Scherrer Institut - PSI. http://asq.web.psi.ch/facility/accelator.html.

[125] various authors, *Neutrons, X-rays and Light: Scattering method applied to soft matter*, North-Holland Delta Series, 2002.

[126] J. Mesot, S. Janssen, L. Holitzner, and R. Hempelmann, J. Neutron Research **3**, 293 (1996).

[127] S. Janßen, J. Mesot, L. Holitzner, A. Furrur, and R. Hempelmann, Physica B **234**, 1174 (1997).

[128] V. García Sakai and A. Arbe, Current Opinion in Colloid & Interface Science **14**, 381 (2009).

[129] *The IRIS User guide - ISIS* - Science & Technology Facilities Council. http://www.isis.stfc.ac.uk/instruments/iris/.

[130] B. Frick and M. Gonzalez, Physica B **201**, 8 (2001).

[131] B. Alefeld, M. Birr, and A. Heidemann, Naturwissenschaften **56**, 410 (1969).

[132] F. Mezei, *Neutron Spin Echo*, Lecture Notes in Physics Vol.28, Springer-Verlag, Heidelberg, 1980.

[133] B. Farago, Physica B **113**, 241 (1997).

[134] various authors, *Neutron Spin Echo Spectroscopy. Basics, Trends and Applications*, Springer, Berlin, 2003.

[135] L. A. Feigin and D. I. Svergun, *Structure Analysis by small-angle X-ray and neutron scattering*, Plenum Press, New York, 1987.

[136] E. N. Maslen, A. G. Fox, and M. A. O'Keefe, *International Tables of Crystallography, vol C*, A. J. C. Wilson, p 476, 1992.

[137] P. A. Doyle and P. S. Turner, Acta Cryst. **A24**, 390 (1967).

[138] F. Kremer and A. Schönals, *broadband dielectric spectroscopy*, springer-verlag berlin, 2003.

[139] R. H. Cole and K. S. Cole, J. Chem. Phys. **10**, 48 (1942).

[140] D. W. Davidson and R. H. Cole, J. Chem. Phys. **18**, 1417 (1950).

[141] D. W. Davidson and R. H. Cole, J. Chem. Phys. **19**, 1484 (1951).

[142] S. Havriliak and S. Negami, J. Polym. Sci. C **14**, 99 (1966).

[143] S. Havriliak and S. Negami, Polymer **8**, 161 (1967).

[144] C. P. Lindsey and G. D. Patterson, J. Chem. Phys. **73**, 3348 (1980).

[145] F. Alvarez, A. Alegría, and J. Colmenero, Phys. Rev. B **44**, 7306 (1991).

[146] M. P. Allen and D. J. Tildesley, *Computer Simulations of Liquids*, Clarendon Press, Oxford, 1987.

[147] J. M. Haile, *Molecular Dynamics Simulation. Elementary methods*, Wiley-Interscience Publication, 1992.

[148] D. Frenkel and B. Smit, *Understanding Molecular Simulation: From Algorithms to Applications*, Accademic Press, San Diego, 1996.

[149] Accelrys. Materials science modeling and simulations. http://www.accelrys.com.

[150] *Accelrys Inc., Cerius²4.8 Forcefield-Based Simulations, Release 4.8,* San Diego: Accelrys Inc. (2003).

[151] Computational Center, Donostia International Physics Center - DIPC. http://dipc.ehu.es/cc/hardware.htm.

[152] *MSI Forcefield Engines,* San Diego: Molecular Simulations Inc. (1997).

[153] D. N. Theodorou and U. W. Suter, Macromolecules **18**, 1467 (1985).

[154] H. Sun, J. Phys. Chem. B **102**, 7338 (1998).

[155] S. W. Bunte and H. Sun, J. Phys. Chem. B **104**, 2477 (2000).

[156] J. Yang, Y. Ren, A. Tian, and H. Sun, J. Phys. Chem. B **104**, 4951 (2000).

[157] H. Sun and D. Rigby, Spectrochimica Acta Part A **53**, 1301 (1997).

[158] W. C. Swope, H. C. Andersen, P. H. Berens, and K. R. Wilson, J. Chem. Phys. **76**, 637 (1982).

[159] L. Verlet, Phys. Rev. **159**, 98 (1967).

[160] A.-C. Genix et al., Macromolecules **39**, 3947 (2006).

[161] A.-C. Genix et al., Macromolecules **39**, 6260 (2006).

[162] M. Tyagi, A. Arbe, F. Alvarez, J. Colmenero, and M. A. González, J. Chem. Phys. **129**, 224903 (2008).

[163] A. Arbe et al., Phys. Rev. Lett. **89**, 245701 (2002).

[164] J. Colmenero, A. Alegria, A. Arbe, and B. Frick, Phys. Rev. Lett. **69**, 478 (1992).

[165] R. Zorn, Phys. Rev. B **55**, 6249 (1997).

[166] R. Casalini and C. M. Roland, J. Chem. Phys. **119**, 4052 (2003).

[167] *Physical Properties of Polymers Handbook,* edited by J. E. Mark, Springer, New York, 1996.

[168] J. Colmenero, F. Alvarez, and A. Arbe, Phys. Rev. E **65**, 041804 (2002).

[169] C. Saelee, T. M. Nicholson, and G. R. Davies, Macromolecules **33**, 2258 (2000).

[170] R. Zorn et al., Phys. Rev. E **52**, 781 (1995).

[171] A. Narros et al., J. Chem. Phys. **121**, 3283 (2004).

[172] A.-C. Genix et al., Macromolecules **39**, 6260 (2006).

[173] A. Chahid, A. Alegria, and J. Colmenero, Macromolecules **27**, 3282 (1994).

[174] F. Alvarez, A. Arbe, and J. Colmenero, Chem. Phys. **261**, 47 (2000).

[175] J. Colmenero, R. Mukhopadhyay, A. Alegria, and B. Frick, Phys. Rev. Lett. **80**, 2350 (1998).

[176] J. Colmenero, A. Moreno, and A. Alegria, Prog. Polym. Sci. **30**, 1147 (2005).

[177] S. Mossa, R. D. Leonardo, G. Ruocco, and M. Sampoli, Phys. Rev. E **62**, 612 (2000).

[178] A. Arbe et al., Phys. Rev. E **67**, 051802 (2003).

[179] A. Soldera and Y. Grohens, Polymer **45**, 1307 (2004).

[180] R. Pérez-Aparicio, A. Arbe, F. Alvarez, J. Colmenero, and L. Willner, Macromolecules **42**, 8271 (2009).

[181] B. Frick, D. Richter, and C. Ritter, Europhys. Lett. **9**, 557 (1989).

[182] A.-C. Genix et al., Macromolecules **39**, 3947 (2006).

[183] M. Beiner, K. Schröter, E. Hempel, S. Reissig, and E. Donth, Macromolecules **32**, 6278 (1999).

[184] M. Wind, R. Graf, S. Renker, H. W. Spiess, and W. J. Steffen, J. Chem. Phys. **122**, 014906 (2005).

[185] A. Narros et al., Macromolecules **38**, 9847 (2005).

[186] J. Colmenero, A. Alegria, J. M. Alberdi, F. Alvarez, and B. Frick, Phys. Rev. B **44**, 7321 (1991).

[187] J. Colmenero, A. Arbe, A. Alegría, and K. L. Ngai, J. Non-Cryst. Solids **229**, 172 (1994).

[188] B. Farago et al., Phys. Rev. E **65**, 051803 (2002).

[189] M. Tyagi, A. Arbe, A. Alegría, J. Colmenero, and B. Frick, Macromolecules **40**, 4568 (2007).

[190] A. Narros, A. Arbe, F. Alvarez, J. Colmenero, and D. Richter, J. Chem. Phys. **128**, 224905 (2008).

[191] D. Richter et al., Europhys. Lett. **66**, 239 (2004).

[192] M. Aichele and J. Baschnagel, Eur. Phys. J. E **5**, 229 (2001).

[193] B. Doliwa and A. Heuer, Phys. Rev. Lett. **80**, 4915 (1998).

[194] *The α-scaling has to be checked by choosing a value for the decay of the correlation function small enogh to assure that the relevant process*

driving the dynamics there is the α-relaxation. The resulting quality of the scaling representation does not change if we choose any value below 0.3.

[195] M. Fuchs, J. Non-Cryst. Solids **172**, 241 (1994).

[196] J. Horbach and W. Kob, Phys. Rev. E **64**, 041503 (2001).

[197] F. Sciortino, L. Fabbian, S.-H. Chen, and P. Tartaglia, Phys. Rev. E **56**, 5397 (1997).

[198] M. Bernabei, A. J. Moreno, and J. Colmenero, Phys. Rev. Lett. **101**, 255701 (2008).

[199] A. van Zon and S. W. de Leeuw, Phys. Rev. E **60**, 6942 (1999).

[200] M. Sperl, Phys. Rev. E **68**, 031405 (2003).

[201] E. Zaccarelli et al., Phys. Rev. E **66**, 041402 (2002).

[202] F. Sciortino, P. Tartaglia, and E. Zaccarelli, Phys. Rev. Lett. **91**, 268301 (2003).

[203] A. J. Moreno and J. Colmenero, J. Chem. Phys. **124**, 184906 (2006).

[204] A. J. Moreno and J. Colmenero, J. Chem. Phys. **125**, 164507 (2006).

[205] A. J. Moreno and J. Colmenero, Phys. Rev. E **74**, 021409 (2006).

[206] V. Krakoviack, Phys. Rev. Lett. **94**, 065703 (2005).

[207] T. Springer, *Quasielastic neutron scattering for the investigation of diffusive motions in solids and liquids*, Springer Tracts in Modern Physics, 64, Springer-Verlag, Berlin, 1972.

[208] K. S. Singwi and A. Sjölander, Phys. Rev. **120**, 1093 (1960).

[209] P. A. Egelstaff, *An Introduction to the liquid state*, Oxford University Press, 1992.

[210] S. Capponi et al., J. Chem. Phys. **131**, 204901 (2009).

[211] Y. Tamai, H. Tanaka, and K. Nakanishi, Macromolecules **29**, 6750 (1996).

[212] M. Diehl, W. Doster, W. Petry, and H. Schober, Biophys. J. **73**, 2726 (1997).

[213] P. J. Steinbach, R. J. Loncharich, and B. Brooks, Chem. Phys. **158**, 383 (1991).

[214] J. Fitter, Biophys. J. **76**, 1034 (1999).

[215] G. Caliskan, A. Kisliuk, A. M. Tsai, C. L. Soles, and A. P. Sokolov, J. Chem. Phys. **118**, 4230 (2003).

[216] A. Paciaroni et al., Chem. Phys. **292**, 397 (2003).

[217] H. Nakagawa, Y. Joti, A. Kitao, and M. Kataoka, Biophys. J. **95**, 2916 (2008).

[218] O. Yamamuro, K. Takeda, I. Tsukushi, and T. Matsuo, Physica B **311**, 84 (2002).

[219] A. K. Rajagopal and K. L. Ngai, *Relaxation in complex systems*, G. B. Wright, North-Holland, Amsterdam, 1991.

[220] D. Goméz and A. Alegría, J. Non-Cryst. Solids **287**, 246 (2001).

[221] J. Colmenero, A. Arbe, and A. Alegría, J. Non-Cryst. Solids **126**, 172 (1994).

[222] D. Richter et al., Macromolecules **31**, 1133 (1998).

[223] T. P. Lodge and T. C. B. McLeish, Macromolecules **33**, 5278 (2000).

[224] J. Colmenero and A. Arbe, Soft Matter **3**, 1474 (2007).

[225] O. Urakawa, Y. Fuse, H. Hori, Q. Tran-Cong, and O. Yano, Polymer **42**, 765 (2001).

[226] C. Lorthioir, A. Alegría, and J. Colmenero, Phys. Rev. E **68**, 031805 (2003).

[227] C. M. Roland and K. L. Ngai, Macromolecules **24**, 2261 (1991).

[228] I. Cendoya et al., Macromolecules **32**, 4065 (1999).

PUBLICATIONS

- *Dynamics of hydration water in a polymer system.*

  R. Busselez, S. Cerveny, S. Capponi, A. Arbe, J. Colmenero, B. Frick and J. M. Zanotti, in preparation.

- *Quasielastic neutron scattering study of hydrogen motions in an aqueous poly(vinyl methyl ether) solution.*

  S. Capponi, A. Arbe, S. Cerveny, R. Busselez, B. Frick, J. P. Embs and J. Colmenero, submitted to J. Chem. Phys. (February 2011).

- *The free volume of poly(vinyl methyl ether) as computed in a wide temperature range and at length scales up to nanoregion.*

  D. Račko, S. Capponi, F. Alvarez and J. Colmenero, J. Chem. Phys. **134**, 044512 (2011).

- *Atomistic motions in poly(vinyl methyl ether): a combined study by quasielastic neutron scattering and molecular dynamics simulations in the light of the mode coupling theory.*

  S. Capponi, A. Arbe, F. Alvarez, J. Colmenero, B. Frick and J. P. Embs, J. Chem. Phys. **131**, 204901 (2009).

161

- *The free-volume structure of a polymer melt, poly(vinyl methyl ether) from molecular dynamics simulations and cavuty analysis.*

  D. Račko, S. Capponi, F. Alvarez, J. Colmenero and J. Bartoš, J. Chem. Phys. **131**, 064903 (2009).

- *Thermal fluctuations of DNA enclosed by glycerol-water glassy matrices: an elastic neutron scattering investigation.*

  E. Cornicchi, S. Capponi, M. Marconi, G. Onori and A. Paciaroni, Eur. Biophys. J. **37**, 583 (2008).

- *Temperature dependence of fast fluctuations in single- and double-stranded DNA molecules: a neutron scattering investigation.*

  E. Cornicchi, S. Capponi, M. Marconi, G. Onori and A. Paciaroni, Phil. Mag. **87**, 509 (2007).

ACKNOWLEDGEMENTS

Quisiera dar mi más profundo agradecimiento a los directores de mi tesis: el Director del CFM Prof. Juan Colmenero y la Prof. Arantxa Arbe. Durante estos años me han supervisado y constantemente apoyado en mi trabajo, han confiado en mi y sobre todo me han dado la oportunidad de formarme científicamente. Gracias a ellos el doctorado se ha vuelto una etapa fundamental, no sólo desde el punto de vista científico.

Quisiera también agradecer a todas las personas del grupo de Polymers and Soft Matter. En particular al Director del Departamento de Física de Materiales Prof. Ángel Alegría por su apoyo en llevar a cabo el Ph. D. en un país extranjero, al Dr. Fernando Alvarez por haberme introducido en el tema de las simulaciones, al Dr. Angel Moreno per avermi aiutato nella prima parte del dottorato, a la Dr. Silvina Cerveny por haber contribuido a encontrar un tema de investigación tan interesante cuanto difícil como el agua, a Luis y a Silvia por su sincera amistad. I would like to thank Dr. Bernhard Frick for his help in the experiments at ILL and for his suggestions. Un ringraziamento sincero va al mio ex-boss Dr. Alessandro Paciaroni per il suo costante appoggio anche a distanza. Quisiera agradecer a mis compañeros de despacho Yasmin y Siddharth por aguantar mis cambios de humor, a

calor a mi euskalvida: os adoro! Un gracias especial a Merethe y Lu, la otra perseguida como yo.

Mila esker Gorka, por tu ciberamistad y por haber librado mi alma romana escondida por el xirimiri.

Eskerrik asko Nere, una de las super cocodrilos como yo, por tu verdadera amistad y todos los momentos que hemos pasado juntas, Iñaki por tener ese trabajo tan raro y animarme a quedar a las 8 de la mañana: sin ti nunca hubiera podido encontrar otra vez la felicidad de madrugar para hacer algo que me guste. Iñigo, por enseñarme todo los trucos basicos del txurf y por animarme a comprar mi primera tabla. Nacho, Alberto, Ainhoa, Monika, Regina, Noa y el resto de la gente de los cursillos. Irantzu por tu sonrisa. Y si estoy pillando estas izquierdas y derechas de pm (por mi, por supuesto) es también por Mikel, Josetxo, Dani, Rodrigo y Iker, por haberme trasmitido lo que es el txurf: mila esker lagunak!

Danke Biondo por estos meses pasados juntos en el agua y en los bares de Donosti.

Finalmente quiero de verdad agradecer a todos los que no están incluidos en este capítulo y que aun sólo por un momento me han realegrado esta temporada: su apoyo ha sido fundamental!!